ANALYSIS OF THE GÁLVEZ-DAVISON INDEX FOR CONVECTIVE FORECASTS OVER AFRICA USING THE GALWEM

THESIS

William A. Hanson, 1Lt, USAF

AFIT-ENP-MS-19-M-81

DEPARTMENT OF THE AIR FORCE
AIR UNIVERSITY

AIR FORCE INSTITUTE OF TECHNOLOGY

Wright-Patterson Air Force Base, Ohio

ANALYSIS OF THE GÁLVEZ-DAVISON INDEX FOR CONVECTIVE FORECASTS
OVER AFRICA USING THE GALWEM

THESIS

Presented to the Faculty

Department of Engineering and Physics

Graduate School of Engineering and Management

Air Force Institute of Technology

Air University

Air Education and Training Command

In Partial Fulfillment of the Requirements for the

Degree of Master of Science in Atmospheric Science

William A. Hanson, BS

1 LT, USAF

March 2019

AFIT-ENP-MS-19-M-81

ANALYSIS OF THE GÁLVEZ-DAVISON INDEX FOR CONVECTIVE FORECASTS
OVER AFRICA USING THE GALWEM

William A. Hanson, BS

1 LT, USAF

Committee Membership:

Maj. H.R. Tseng, PhD
Chair

Maj. Omar Nava, PhD
Member

Capt. Gabriel Donndelinger
Member

AFIT-ENP-MS-19-M-81

ABSTRACT

Thunderstorm forecasting over Africa has presented significant difficulty. The Gálvez-Davison Index (GDI) was developed for the Americas and provides a more accurate convective forecasting index than the conventional indices for thunderstorm forecasting.. Previous research using the GDI via the Global Forecasting System (GFS) model data over Africa showed promising results for areal coverage (Donndelinger 2018), especially during the spring through fall months. This study will look to test the GDI via the Global Air Land Weather Exploitation Model (GALWEM) to determine if the GALWEM GDI forecast is able to more accurately forecast the location and areal coverage, as well as resolve airmass thunderstorms, when compared to the GALWEM K Index (KI) and GFS GDI forecast.

Results from this study show the GDI and KI have similar location error at the 95% confidence level across the monthly, Zulu time, convective regime, and regional studies. GDI consistently outperforms the KI in terms of areal convection coverage in every study analyzed at the 95% confidence level. The GDI proves to perform best when convection is primarily airmass-based, while the KI performs best when convection is primarily from Mesoscale Convective Systems (MCSs). Furthermore, Kelvin waves and outgoing longwave radiation (OLR) show promise as additional convective forecast tools for Africa. This study contains important information for furthering meteorological understanding of convection and precipitation over the African continent.

v

Acknowledgments

Major Rose Tseng for taking me on as her thesis student and pushing me in her own way to produce a more thorough and significant product than I thought possible.

Captain Gabriel Donndelinger for allowing me to continue his research on the GDI and KI over Africa and providing the framework of the code for plotting and analyzing the GDI.

Major Omar Nava for his help with some coding issues and talks on clustering analysis.

Dr. Jose Gálvez and Mr. Michel Davison for allowing me to use their index and for setting time aside to meet with me regarding this specific research.

14th Weather Squadron for providing the lightning data used in this project for multiple different regions in a timely manner.

16th Weather Squadron for tirelessly providing GALWEM data each week.

Naval Research Laboratory (NRL) and *Weather.us* for providing satellite imagery.

University Corporation for Atmospheric Research (UCAR) Research Data Archive (RDA) for their GFS analysis data.

My classmates for all of your help and keeping me grounded. You're awesome!

My amazing wife for her constant support and encouragement through the entire process. I cannot thank her enough. Thank you to my friends and siblings for pushing me to better myself and escape at times! Thank you to my parents for instilling in me a good work ethic and extreme stubbornness.

Lastly, this thesis is dedicated to my grandfather who passed away this fall; you set the example of humility and hard work for me to follow.

Table of Contents

List of Figures

List of Tables

A NEW ANALYSIS OF THE GALWEM GÁLVEZ-DAVISON INDEX FOR CONVECTIVE FORECASTS IN NORTHERN AFRICA

1. Introduction

General Issue

Forecasting convective activity in Africa is a daunting task due to several limiting factors. The continent of Africa has a lack of quality data coverage and the increased focus and activity in the region creates significant challenges for weather forecasting and planning. The research here focuses on convective forecasting over the African continent. Thunderstorm location forecasting is of particular importance, as lightning strikes present significant aviation and operational risk management concerns. Location accuracy of convective indices is one of the main focal points of this study.

Convective indices are one important tool used to aid thunderstorm forecasting globally. These indices assess parameters from real-time or atmospheric soundings of the vertical atmosphere to provide meteorologists an idea of the probability for convective storms. Parameters include moisture, temperature and dewpoint temperature to determine instability in a certain region. Some of these convective indices include: Lifted Index (LI), Showalter Stability Index (SSI), and the Total Totals Index. The K Index (KI), in particular, has been regarded as a quality index for the tropical regions (Gálvez and Davison 2016). In North America, the LI, SSI and TTI are generally accepted as the standard for convective forecasting, but no one index has been accepted as a standout for Africa. However, positive results have been achieved when the GDI is recreated and analyzed over Africa (Donndelinger 2018). The findings of Donndelinger (2018) will be discussed more in Chapter IV.
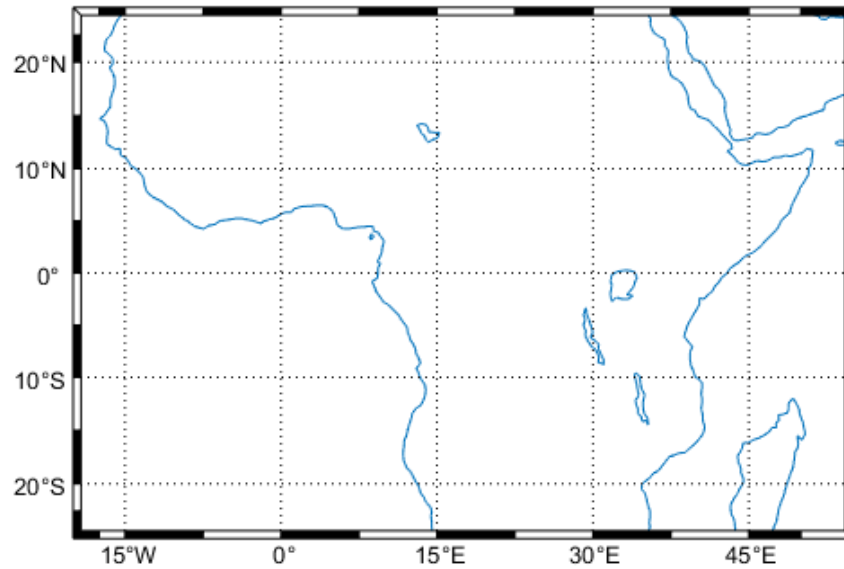
Figure 1.1. The region of interest: The African continent bounded by 25°S-25°N and 20°W-55°E.

The area of interest for this research is the majority of the continent of Africa, specifically from 25°S-25°N and 20°W-55°E (Figure 1.1). This area is chosen because the GDI is designed for the tropics.

NOAA researchers, Jose Gálvez and Michel Davison, developed a new convective index tailored for the Caribbean and Central America (Gálvez and Davison 2016). Validation studies have been conducted and variations have been made to tailor the Gálvez and Davison Index (GDI) for Costa Rica, South America, and in climatologically different areas such as South Korea (Omar Nava, written communication, July 13, 2017). The purpose of this research is to expand upon previous studies by Gálvez and Davison (2016) and Donndelinger (2018) in order to analyze and compare the forecasting skill of the GDI and KI over Africa using the Global Air Land Weather Exploitation Model (GALWEM).

Problem Statement

Forecasting techniques for convective activity in Africa are currently based on indices created with meteorological understanding and weather data from other parts of the world. While Donndelinger (2018) showed promising results analyzing the GDI via GFS 1° horizontal resolution reanalysis data, the horizontal resolution of this GFS data is fairly coarse and this presents an issue for airmass thunderstorms. The Air Force's GALWEM has yet to be tested using the GDI over Africa, making it the next step for this research study as it is the Air Force's forecasting model of choice.

Hypothesis

The GALWEM GDI will more accurately predict convective storms over Africa than the KI. The GALWEM has a horizontal resolution of 17 km, whereas the GFS reanalysis data used in the previous study has a horizontal resolution of 1° longitude by 1° latitude, or approximately 111 km by 111 km. The much higher resolution of the GALWEM data should help resolve airmass thunderstorms and more accurately identify areas of likely convection. Any adjustments to the index should consider differences between the models, as well as climate differences between Central America, the Caribbean, and different regions in Africa.

Research Objectives, Focus Questions

The research objectives are as follows:

1. Replicate both the GDI and KI algorithms in Matlab using the GALWEM data, and plot the index over the African region of interest, providing a similar display to the NOAA website (https://www.wpc.ncep.noaa.gov/international/gdi/)

2. Plot each base parameter used to calculate the GDI with GALWEM data against GFS analysis data counterpart in order to see if there are any significant model biases present

3. Ensure lightning data and strike placement is realistic and lines up with cold cloud top coverage via satellite imagery

4. Assess the skill of both indices by comparing forecasts with lightning data and satellite imagery, statistically analyzing its skill in predicting convection over Africa

5. Test GDI-Africa (GDI-As) developed by Donndelinger (2018) and modify the GDI to further develop or create new GDI-As, considering differences between the target regions: the Caribbean and Africa; adjust the parameters within GDI and/or add new terms to modify and tailor the new GDI-A

6. Assess the skill of the GDI-As for Africa by comparing forecasts with lightning data and satellite imagery, statistically analyzing its skill in predicting convection over Northern Africa

7. Split the GDI and GDI-As into West and East and statistically analyze the forecasting accuracy of these two regions when compared to lightning data and satellite imagery, in order to determine if there is a regional correlation to GDI forecast accuracy

Research questions for investigation:

1. How well does the GALWEM GDI predict convection over Africa for both spatial coverage and location of storms?

2. Does the GALWEM data, and subsequently GDI, help resolve airmass thunderstorms? (This was a weakness of the GFS 1° longitude by 1° latitude reanalysis data)

3. Does the GALWEM GDI need improvement for forecasting over Africa, and if so, how? Do the GDI-As developed by Donndelinger (2018) improve forecast accuracy for Africa when used with the GALWEM? What additional parameters, if any, need to be considered for the GDI-As?

4. Is there a particular region where the GDI does not perform well? For example, because GDI was developed for the tropics, does the index lack accuracy in one part of the continent over another? Furthermore, does it perform poorly in dry regions such as the Sahara/Sahel and Saudi Arabia?

5. How well does the new GDI-A work over Africa, spatially and intensity wise? Why does it work better than GDI in this region?

6. Does the new GDI-A improve confidence when forecasting convection over Africa?

Assumptions/Limitations

In this study, two sets of model data are used: the GFS analysis data and the GALWEM zero hour (00 HR) forecast data. While the GFS analysis model data is not perfectly representative of the true atmospheric conditions, it is some of the best data available and is accepted as close to observed. Increased emphasis is placed on the low-levels with several more

5

layers represented in the upper levels. The horizontal resolution of the GFS data is 1° latitude by 1° longitude, where 1° is approximately 111 km or 69 miles (UCAR 2017). Convection processes occur at smaller scales than the vertical and horizontal resolutions of the GFS model data, as further explained in Chapter II. Vertically, GFS model data points are set at the surface, 1000 millibars (mb), 975 mb, 950 mb, 925 mb, and 900 mb, and then every 50 mb above that until 100 mb (UCAR 2017).

In Donndelinger (2018), the GFS model data is mapped onto a 1° by 1° grid, with each point assessed to see if the forecast correctly identified the probability for lightning to occur. As discussed by Donndelinger (2018), this is an issue for two reasons: lightning rarely strikes at whole degree latitude and longitude degree values, and interpretation of GFS GDI forecast index values for various levels of convective potential is subjective. Based on these two issues, the selected method of statistical analysis is clustering, rather than point-by-point analysis. Furthermore, although the GALWEM data (17 km) has a much higher resolution than the GFS analysis data (~111 km), it is still not high enough of a resolution to consider point-by-point analysis. For this reason, and in order to keep methods consistent and allow objective comparisons between the results of this study and Donndelinger (2018), clustering will also be used for the statistical analysis here. Lastly, it should be noted that the GALWEM has an effective horizontal resolution of 17 km. The reference latitude for the model is 48.186°N/S with increasing effective horizontal resolution toward the north of this reference latitude and decreasing effective horizontal resolution to its south (GALWEM 2016). For example, the effective 17 km GALWEM horizontal resolution at 15°N (well within the study region) is ~24.6km, which has implications for the phenomena the model can resolve. For the sake of this document, the GALWEM resolution will be referred to as 17 km for the all successive mentions.

Implications

 While the previous study showed some positive results, there is still work to be done in terms of improving forecast location of convective activity in Africa. Increase in forecast confidence over the region with the use of the higher-resolution GALWEM model could aid forecasting ability in terms of predicting the extent, timing and intensity of convection. Increased environmental situational awareness could contribute to a better understanding of weather patterns and storm formation in Africa and ultimately help further knowledge of the role in the Earth's climate system, as well as other human-based systems including transportation, irrigation and agriculture.

Preview

 This thesis is organized in the following fashion: Chapter II discusses sources of formation and types of African thunderstorms along with an overview of past research conducted in tropical convection, Chapter III details the background on data and methodology used in this research, Chapter IV lays out analysis and results, and Chapter V discusses the research results, the impacts and usefulness of the GDI and GDI-A for convective forecasting over Africa, as well as a conclusion of the research with recommendations for future work in this specific topic.

II. Background and Literature Review

Chapter Overview

The purpose of this chapter is to describe the basis of current research and background of convection patterns over Africa. An understanding of this information is crucial to the full understanding of research findings and conclusions at the end of this document.

African Thunderstorms

The majority of literature on convective activity has focused on mid-latitude storms. This is primarily based on the higher population density and subsequent resource allocation. In order to bolster knowledge of global weather patterns and climatology, as well as ease growing transportation, agriculture, and economic stresses, it is vital to gain a better understanding of tropical convection.

Tropical convection and mid-latitude convection vary in many ways. In the tropics, latent heat release initiates and sustains convection, whereas in the mid-latitudes, available potential energy from strong temperature gradients drives convective activity (Holton and Hakim 2013). In the tropics, most latent heat release is tied to convective systems. Therefore, storm activity upstream is an indicator of increased convective potential in these regions (Gálvez and Davison 2016). Mid-latitude convection is primarily caused by fronts, boundaries between airmasses, resulting from strong temperature gradients, while large-scale circulations and latent heat release produce convection in the tropics. Large-scale patterns that drive tropical circulation include the Hadley cell and the Walker Circulation (North Carolina Climate Office 2019).

Differential heating of Earth's surface causes the large-scale circulations observed in our atmosphere. The dominant circulation in the tropics is the Hadley cell; a region where the easterly trade winds in both hemispheres converge near the equator, causing rising air motion (Holton and Hakim 2013). The Hadley cell is responsible for the majority of heat transfer from the equator poleward. As air converges and is pushed vertically above the surface into the atmosphere, pseudoadiabatic ascent and formation of cumulus and cumulonimbus clouds provides heat transport from the surface to aloft (Holton and Hakim 2013). These clouds form a band of discontinuous, deep convection along the meteorological equator circling the globe called the Intertropical Convergence Zone or ITCZ (Galvin 2016). The exact location of the ITCZ moves north and south depending upon the most direct solar radiation on Earth's surface. The trade wind flow aids moisture advection, providing latent heat, and energizing this large-scale, sustained convection in the ITCZ (Holton and Hakim 2013).

The movement of tropical waves is another prominent feature that is associated with convection in the tropics. Within the ITCZ, weak disturbances form and propagate westward, often propelled by the latent heat release from convective precipitation (Holton and Hakim 2013). Within large, convective clouds, upper-level divergence occurs and by mass continuity, low-level convergence also occurs. When this occurs, tropical waves are formed. While it is not easy to detect tropical waves, they can be identified by perturbations in the easterly trade winds, via satellite, or by the changes in 24-hour surface pressure (Kirshnamurti et al. 2013).

Convection in Africa is exhibited in three main ways including: African easterly waves (AEWs), airmass thunderstorms, and Mesoscale Convective Systems (MCSs). Across the African continent, unique processes result in a specific type of waves called African wave disturbances or African easterly waves (AEWs). An apparent feature of the Northern

Hemisphere summer is the strong positive temperature gradient induced between the equator and 25°N due to intense surface heating in the Sahara Desert (Holton and Hakim 2013). This strong temperature gradient causes a low level easterly jet to form around 13-16°N with a jet core at about 650 mb, known as the African Easterly Jet (AEJ) (Holton and Hakim 2013). Monsoonal flow and the lower Walker circulation induce westerly flow at about 10°N with a core around 950 mb. These features combine to create a cyclonic shear zone that promotes initiation and propagation of synoptic-scale tropical waves (Holton and Hakim 2013). These AEWs are more dependent on the barotropic and baroclinic energy conversion from the AEJ as opposed to latent heat release, making them a special category of tropical waves (Holton and Hakim 2013). At 650 mb, stronger winds are observed aloft, indicating the location of the AEJ (Figure 2.1).
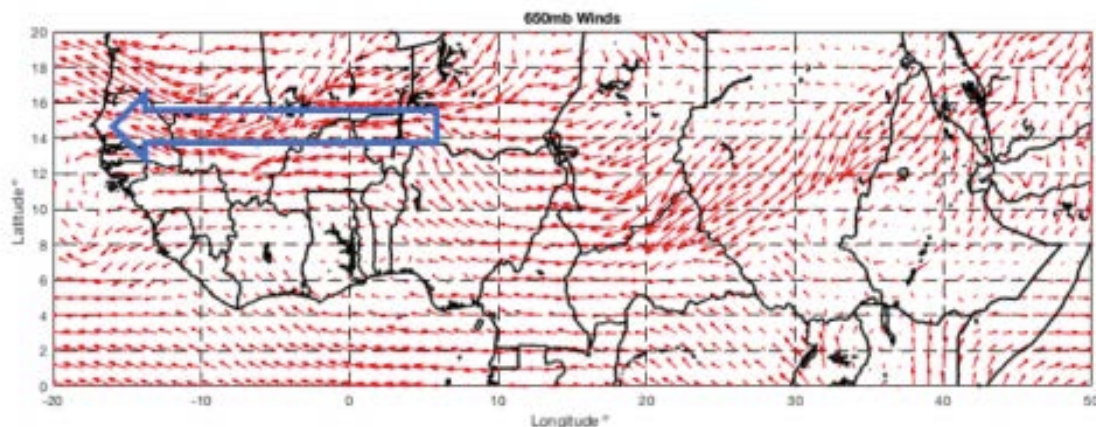
Figure 2.1: The high winds at 650 mb in the AEJ are highlighted by the blue arrow (Donndelinger 2018).

AEWs have some distinct characteristics. These waves can range from 1500-4500 km, averaging 2500 km in length from north to south (Kirshnamurti et al. 2013). With a time scale on the order of 3-5 days, these waves travel at around 8 meters per second or approximately 5-7° longitude per day. AEWs originate somewhere between 15-30°E and reach a maximum amplitude somewhere between 10°E and -20°W over West Africa or the coast. Ahead of the waves are northeasterly winds, low-level convergence, and rising air. As this region is an

easterly shear environment, convection associated with AEWs is found on the west side of the wave axis. AEWs can generate convection, but the aforementioned process is the least prominent manner in which convection is produced.

Convection is often in the form of airmass thunderstorms, which are observed in the tropics and mid-latitudes alike. Airmass thunderstorms are caused from uneven heating of the Earth's surface. If the convective temperature is reached or surpassed, air rises and forms columns of air that do not need any mechanical forcing to create rising motion (Donndelinger 2018). Small, localized thunderstorms can result if enough instability is present. These storms range in size from about 24 km to about 1° of latitude in diameter, or about 111 km, near the equator. Most of these observed systems are smaller than 1° by 1°, which is why the higher-resolution, 17 km GALWEM data was selected (Figure 2.2).
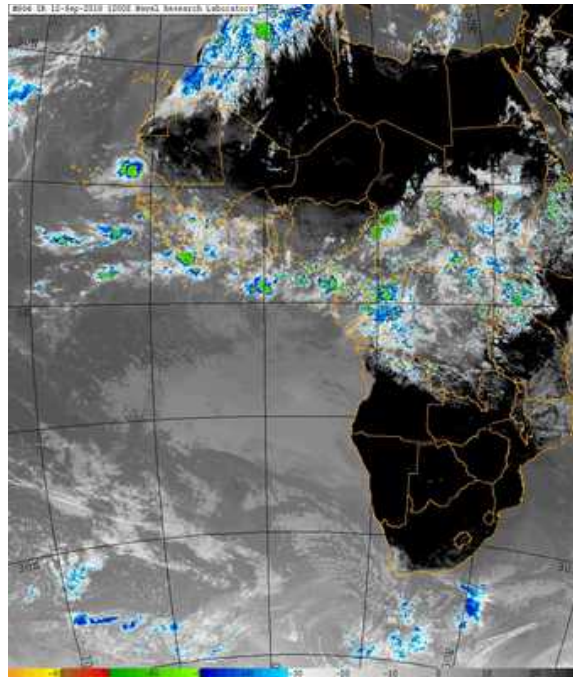
Figure 2.2: Airmass thunderstorms across Africa shown on IR satellite imagery from 12 Sep 2018 at 12Z (NexSat 2011).
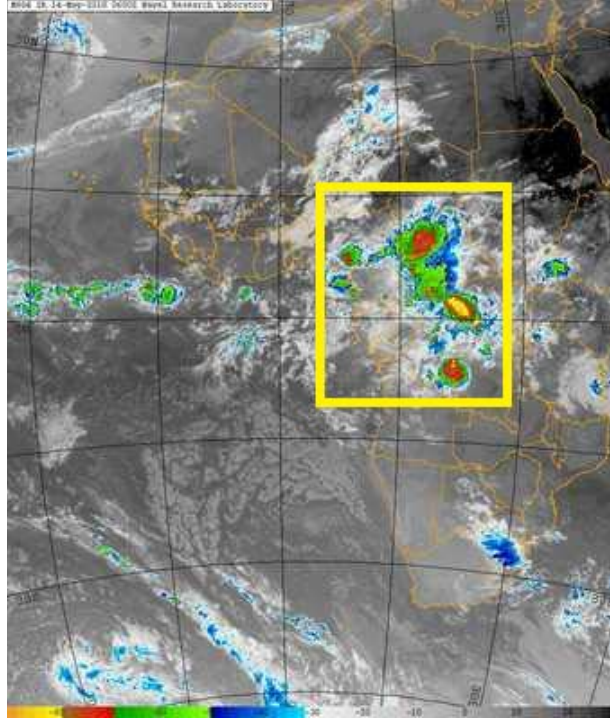
Figure 2.3: MCSs are highlighted inside the large yellow rectangle on IR satellite imagery from 14 May 2018 at 06Z.

Mesoscale Convective Systems (MCSs) are another source of convective activity over Africa. MCSs are large, usually circular, convective storms that encompass much broader areas than independent thunderstorms. These storm systems are defined by cloud-top temperatures of -52°C or colder that cover a minimum area of 30,000 km^2 (Jirak et al. 2003). MCSs have strong vertical velocities, high amounts of precipitation, and broad areas of cold cloud tops (Figure 2.3) (Kirshnamurti et al. 2013). Prime MCS initiation conditions exist over northern Africa with the tropical easterly jet (TEJ) at around 7°N and 175 mb, and the AEJ at around 13-16°N and 650 mb (Figure 2.4). The anticyclonic shear side (northern most portion) of the TEJ in the upper levels overlays the cyclonic shear side of the AEJ in the mid-levels (southern-most portion), inducing convergence in the low levels and divergence aloft. This environmental setup is conducive for the development and maintenance of convection.

12
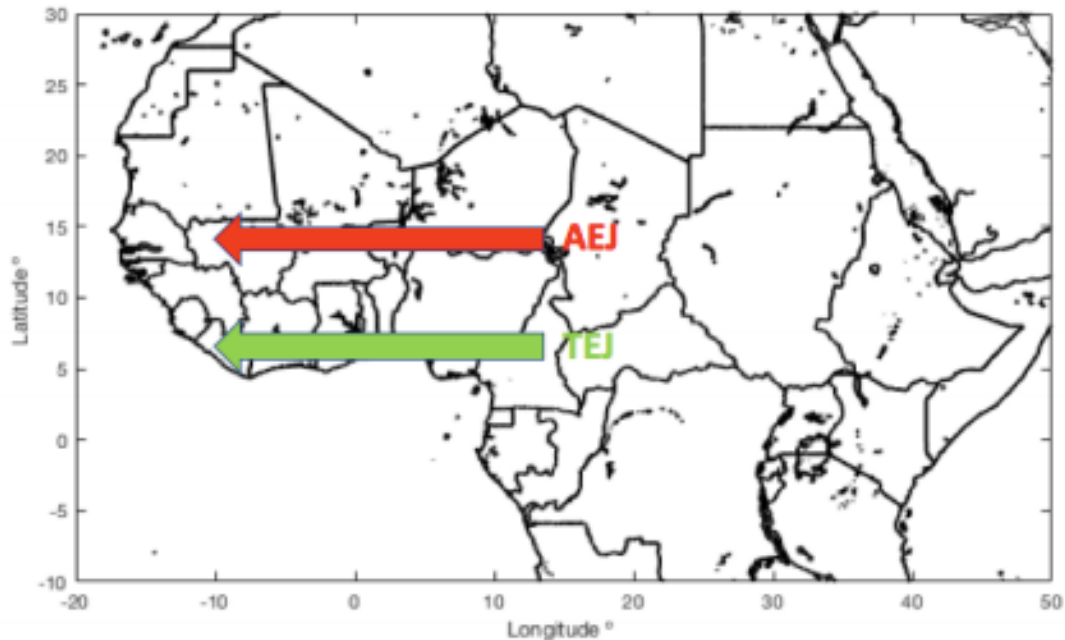
Figure 2.4: The locations of the prominent wind features, the African Easterly Jet (AEJ) at approximately 650 mb, and the tropical easterly jet (TEJ) at approximately 175 mb (Donndelinger 2018).

Almost all squall line systems in West Africa have been observed in this ideal convective-formation environment between the TEJ and AEJ.

Another contributing factor to thunderstorm formation in Africa is the southwesterly monsoonal flow, which pushes onshore over northwestern Africa. This warm, moist air is capped off by the dry, easterly mid-level flow, providing a shearing environment and ideal conditions for storm formation (Kirshnamurti et al. 2013). Typically, small-scale convective systems will dissipate once excess surface heating is no longer present. However, MCSs can form and enhance during the night due to cooling cloud tops that promote vertical development in the atmosphere (Donndelinger 2018).

Another phenomena that modulates convection over the Africa continent is that of Kelvin waves. There are two types of Kelvin waves: coastal and equatorial. Coastal Kelvin waves propagate with the shoreline on the right in the Northern Hemisphere and on the left in the

13

Southern Hemisphere (Krauss 2019). These waves balance the Coriolis force against a topographic boundary. When the wave moves poleward along the coast, the Coriolis force pushes it to the right (left) in the Northern (Southern) Hemisphere and this causes water to pile up along the coast. Excess water on the coast creates a pressure gradient directed offshore and a geostrophic current direct northward. Equatorial Kelvin waves are a special type of Kelvin wave that balances the Northern Hemisphere Coriolis force against the Southern Hemisphere Coriolis force (Krauss 2019). These waves propagate eastward and only along the equator. Studies have shown that Kelvin waves are able to regulate precipitation and convective activity over Africa, primarily near the equator and in conjunction with the West African Monsoon (Krauss 2019; Mekonne et al. 2008; Mounier et al. 2006). This information will be discussed further in Chapter IV via the regional and Kelvin wave studies.

Relevant Research

The K Index (KI)

The KI is often regarded as a quality convective index for forecasting in the tropics because it was developed to pinpoint airmass thunderstorms rather than convection resulting from frontal systems or orographic lift (George 1960). This index was created to forecast thunderstorms over the North Central plains and validated over North America. One major difference between the KI and other common indices is the consideration of the 700 mb moisture within KI. Computation of the KI is carried out via Equation 2.1 below.

$$KI = (850\ mb\ T - 500\ mb\ T) + (850\ mb\ T_d) - (700\ mb\ T - 700\ mb\ T_d) \qquad (2.1)$$

In Equation 2.1, T is the air temperature and T_d is the dewpoint temperature. K is unique in its inclusion of the 700 mb dewpoint depression, which is closely linked to buoyancy and dry air

14

entrainment in the tropical mid-troposphere (Gálvez and Davison 2016). The values of the KI are then categorized by frequency estimates shown in Table 2.1. Since KI is strictly used to forecast airmass thunderstorms, any low-level (below 700 mb) convergence or divergence will affect the frequency of thunderstorms (George 1960). While convergence and divergence are not included in KI calculation, these processes must be considered by the forecaster (George 1960).

Table 2.1: K values and their respective thunderstorm frequency estimates (George 1960).

K Value	Frequency Category
1. Less than 20	None
2. Above 20 but less than 25	Isolated thunderstorms
3. Above 25 but less than 30	Widely scattered thunderstorms
4. Above 30 but less than 35	Scattered thunderstorms
5. Above 35	Numerous thunderstorms

Although it has its strengths for forecasting airmass thunderstorms, the KI includes some weaknesses in regards to tropical environments such as low variability in shallow convective regions, as well as a disregard of thermodynamic properties below 850 mb (Gálvez and Davison 2016). K does not take into account stability contributions below 850 mb, which are key for tropical convection. The GDI has focused on these weaknesses in the KI because it was developed for tropical convection, specifically over Central America and the Caribbean, where low-level processes are the primary contributors of convective development. Some other common convective indices and their corresponding characteristics are included in Table 2.2 for reference. Each index considers multiple parameters at various levels in the atmosphere as a quick look at convective potential.

Table 2.2: Gálvez and Davison's assessment of common convective indices (Gálvez and Davison 2016).

Index	Reference	Summary
Showalter	Showalter (1947)	Estimates convective instability by comparing the difference between the 500 hPa ambient temperature and that of a parcel rising from 850 hPa following the dry adiabat until saturated, and then the moist adiabat.
K	George (1960)	The K was developed to forecast air mass thunderstorms. It considers an 850-500hPa lapse rate term and an 850-700 hPa moisture term. The consideration of 700 hPa moisture adds skill in tropical environments. Limitations are performance over elevated terrain and spatial homogeneity in the deep tropics.
Lifted	Galway (1966)	Similar to the Showalter index, but the parcel is lifted from the boundary-layer top instead of 850 hPa. Although methods for the determination of this level vary, it is often determined using the warmest diurnal temperature and the mean mixing ratio at 2m, predicted if necessary. This height often falls within the lowest 900m of the profile. Lifted index values tend to be lower than Showalter index values.
Total Totals	Miller (1967)	It is based upon an 850-500hPa lapse rate term and upon a cross moisture-temperature term. The latter is largely sensitive to 850 hPa moisture. It was designed for applications in the United States (Peppler and Lamb, 1989).

The Gálvez-Davison Index (GDI)

The Gálvez-Davison Index (GDI) is a new index developed for tropical convection that works to fill the gaps of knowledge left by common convective indices lack of skill and accuracy in the tropics (Gálvez and Davison 2016). The GDI is comprised of four main sub-indices: equivalent potential proxies core index (ECI), mid-level warming index (MWI), inversion index (II), and surface pressure correction for elevation (Co). The GDI considers additions from three separate atmospheric layers when calculating these sub-indices (Figure 2.5).
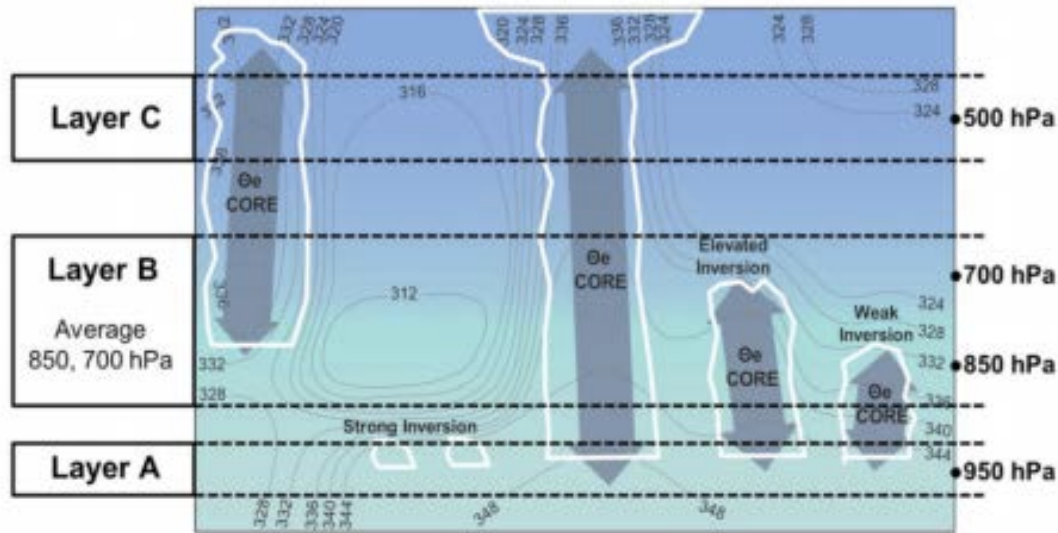
Figure 2.5: Model depiction of the layers used in the GDI algorithm to forecast convective potential (Gálvez and Davison 2016).

Equivalent Potential Temperature Proxies Core Index (ECI)

Equivalent potential temperature (EPT) is a meteorological quantity that accounts for both temperature and moisture in the atmosphere (Gálvez and Davison 2016). EPT can indicate the column moisture and potential release of latent heat. As mentioned previously, release of latent heat is the main cause of convection in the tropics. Higher EPT values are favorable for convection, and slow decrease with height is favorable for deep convection. The 950 mb height is chosen to be the center of layer A in order to capture the characteristics of the boundary layer; 925 mb proved to be too high at times. Technically, the air temperature at the lifted condensation level (LCL) should be used to calculate the EPT but to simplify the calculations of EPT, air temperatures at 850 mb were chosen instead of LCL temperature. Only minor differences in GDI values were noted when using this substitution.

Two important factors to consider when forecasting tropical convection are moisture and trade wind inversions (TWI). In the tropics, moisture is mainly a product of foregoing convection (Gálvez and Davison 2016). A feedback mechanism of moisture and convection indicates that

17

foregoing convection in upstream locations could be used as a predictor for tropical convection. TWI is another important meteorological factor to consider when forecasting convection in the tropics. This feature is identified by a minor decrease in lapse rate or, sometimes, a small increase in temperature with height. The cause of the TWI is descending air in the Hadley cell. The development of convection depends on the strength and height of these inversions. With a stronger and lower inversion, vertical development is inhibited, while some growth can occur with weaker and higher inversions. Regions with both ample moisture and limited inhibiting inversion are ideal for convective development. Calculating the EPTs within the GDI formula incorporates the warm, moist column as well as the TWI signatures.

In order to calculate the equivalent potential temperature proxy (EPTP) term for the GDI, the EPTPs from all three layers, A, B, and C are incorporated.

$$\theta_A = \theta_{950} = T_{950}\left(\frac{1000}{950}\right)^{2/7} \tag{2.2}$$

$$\theta_B = 0.5(\theta_{850} + \theta_{700}) = 0.5[T_{850}\left(\frac{1000}{850}\right)^{\frac{2}{7}} + T_{700}\left(\frac{1000}{700}\right)^{\frac{2}{7}}] \tag{2.3}$$

$$\theta_C = \theta_{500} = T_{500}\left(\frac{1000}{500}\right)^{2/7} \tag{2.4}$$

Final EPTP values are calculated using the EPTPs above in the following manner:

$$EPTP_A = \theta_A\, e^{\left(\frac{L_0\, r_{950}}{c_{pd} T_{850}}\right)} \tag{2.5}$$

$$EPTP_B = \theta_B\, e^{\left(\frac{L_0\, (0.5(r_{850} + r_{700}))}{c_{pd} T_{850}}\right)} + \propto \tag{2.6}$$

$$EPTP_C = \theta_C\, e^{\left(\frac{L_0\, r_{500}}{c_{pd} T_{850}}\right)} + \propto \tag{2.7}$$

In the equations above, the 'r' represents the mixing ratio at the specified levels, the empirical

adjustment constant $\propto = -10[K]$, the latent heat constant $L_o = 2.69E6\frac{J}{kg}$, and the specific heat

of dry air at constant pressure $c_{pd} = 1005.7\frac{J}{kg\ K}$.

Finally, the ECI is calculated using mid-level EPTP (ME) and low-level EPTP (LE)

factors.

$$ME = EPTP_C - \beta \tag{2.8}$$

$$LE = EPTP_A - \beta \tag{2.9}$$

In the equations above, $\beta = 303[K]$ and it is an empirical constant. The final ECI is calculated

using Equation 2.10 below.

$$ECI = \begin{cases} \gamma * (EPTP_A - \beta) * (EPTP_C - \beta), LE > 0 \\ 0, LE \leq 0 \end{cases} \tag{2.10}$$

In equation 2.10, $\gamma = 6.5 * 10^{-2}[K^{-1}]$ and is an empirical scaling constant. Equation 2.10 shows

that the convective potential increases based on the EPTP$_A$ and EPTP$_C$ difference from the β

empirical constant. The GDI determines the amount of moisture and heat in the low-levels and

aloft. If both levels have significant amounts of both moisture and heat, the column will be

primed for convective activity.

Mid-Level Warming Index (MWI)

The MWI sub index quantifies stability changes in the mid-levels based on temperatures

at 500 mb. The MWI stability is related to warm ridges (stable) and cool troughs (unstable) in the

mid-levels. This index is an inhibition factor, meaning it only produces negative values or is set

to zero. The MWI relies on the 500 mb air temperature departure from $\tau = 263.15[K] (\sim -$

10°C). If the 500 mb temperature is warmer than τ, the MWI has a negative value and this

reduces the magnitude of the GDI. If the 500 mb temperature is cooler than τ, the MWI is set to zero and does not affect the GDI (Equation 2.11).

$$MWI = \begin{cases} \mu * (T_{500} - \tau), T_{500} - \tau > 0 \\ 0, T_{500} - \tau \leq 0 \end{cases} \tag{2.11}$$

In equation 2.11 above, $\mu = -7[K^{-1}]$ is an empirical constant established that sets MWI to a negative value and controls the relative weight of the MWI on the GDI formula. Warmer 500 mb temperatures will lower the GDI values, decreasing convective potential.

Inversion Index (II)

The inversion index is another inhibiting sub index of the GDI. The II considers stability across the inversion and dry air entrainment once convective cells penetrate the inversion. Both of these processes inhibit trade wind convection. The II is made up of two dimensionless factors, a stability factor S and a drying factor D, where S and D are as follows:

$$S = \sigma * (T_{950} - T_{700}) \tag{2.12}$$

$$D = \sigma * (EPTP_B - EPTP_A) \tag{2.13}$$

In equations 2.12 and 2.13 above, $\sigma = 1.5[K^{-1}]$ is an empirical scaling constant determined ad hoc in order to control the weight of TWI effects on the GDI. The stability factor shows that the smaller the difference, the stronger the stability of the layer due to an increase in negative buoyancy. A large difference indicates an unstable 950-700 mb layer. The more negative D becomes, the more dry air entrainment is occurring, and therefore inhibition of the convective development. Below, positive values of II are set to zero, to ensure II is an inhibiting factor:

$$II = \begin{cases} 0, S + D > 0 \\ \sigma * (S + D), S + D \leq 0 \end{cases} \tag{2.14}$$

Correction for Elevation (Co)

The GDI was developed for use in regions with a surface pressure located below 950 mb. However, in high elevation areas, 950 mb is actually below the surface. For this reason, a terrain correction factor is needed to adjust for unrealistically high GDI values over high terrain into more realistic numbers. The CO is calculated as follows:

$$Co = 18 - \frac{9000}{P_{SFC} - 500},$$ (2.15)

In Equation 2.15, $18, 9000, and\ 500$ are all empirical constants in hectopascals (hPa). Gálvez and Davison (2016) found that this correction factor was necessary over the Mexican highlands.

In order to calculate the GDI, the sub-indices are added together to indicate various convective potential, where higher numbers indicate greater potential (Figure 2.6).

$$GDI = ECI + MWI + II + Co$$ (2.16)

GDI> 45	High potential for scattered to widespread thunderstorms
+35 to +45	Potential for scattered thunderstorms and/or widespread shallow convection
+25 to +35	Potential for scattered shallow convection and isolated to scattered thunderstorms
+15 to +25	Potential for isolated to scattered shallow convection and a few isolated thunderstorms
+5 to +15	Potential for isolated to scattered shallow convection. Any T-storm brief and isolated
-20 to +5	Isolated to scattered shallow convection. Strong subsidence inversion likely.
GDI<-20	Fair conditions. Any convection should be shallow, isolated and produce very light rain.

Figure 2.6: GDI values and their corresponding convective potential (Gálvez and Davison 2016).

Gálvez and Davison (2016) concluded that the GDI outperformed the TTI, LI, KI, and the Convective Available Potential Energy (CAPE) for the study region of Central America and

the Caribbean. Their study analyzed GDI values compared to brightness temperatures shown in the GOESIR4 satellite imagery. They used a determination coefficient of r^2 to assess performance of GDI relative to LI, TTI, KI, and CAPE via GFS data. Data were compared at two different horizontal resolutions: 1° and 2°. Their results indicate that GDI outperforms most stability indices in its depiction of convection in the tropics. GDI performed best in the 15°N - 25°N belt of the study region, with high correlation of brightness temperatures noted in the Gulf of Honduras/Yucatan Peninsula and in central Mexico (Gálvez and Davison 2016). Results are encouraging in Mexico, where much of the terrain lies above 950 mb and a large urban population is present in Mexico City and the surrounding region.

Donndelinger (2018) also showed positive results for use of the GDI over Africa. In the previous study, Donndelinger (2018) recreated the GDI algorithm and compared its accuracy against the National Oceanic and Atmospheric Association (NOAA) GDI forecasts using GFS model reanalysis data at a resolution of 1° by 1°. Then, the KI is recreated and both the GDI and KI are compared to satellite data to ensure a reasonable depiction of these indices is being plotted. Donndelinger (2018) used K means clustering to group detected lightning strikes archived by the 14th Weather Squadron. The lightning clusters were examined and GDI, along with KI, values greater than 35 and 30 respectively were selected to indicate high potential for convective activity. The same number of clusters is chosen for GDI and KI as the clusters indicated by the k-means plot for lightning in order to keep consistency. Lightning and GDI/KI clusters were compared visually and paired by geographic proximity to one another. Then, average areal coverage and location values were calculated. Location error is determined by taking the difference between the observed (lightning cluster) and forecasted (GDI/KI cluster) centroids for the lightning. Average area error is determined by calculating the average

22

difference between a centroid and each of the data points within that cluster and taking the difference of paired clusters' average point-to-centroid distances.

Donndelinger (2018) found that GDI and KI consistently had similar location error values, while the GDI proved to have significantly lower area error values than KI in almost all cases. An exception occurred when convection was primarily airmass thunderstorms in the intra-seasonal sub study. Donndelinger (2018) also noted that location error values from both indices were lowest in the summer and highest in the winter. The opposite was found of the GDI area error, which had highest error values in the summer and lowest in the winter. GDI consistently depicts the spatial coverage of convection more accurately than KI with the most drastic difference in error noted in the winter and least in the spring (Donndelinger 2018).

Donndelinger (2018) also modified the GDI by adding multiple parameters as a fifth sub index, in order to determine if the GDI could be adjusted to more accurately portray convection over Africa. Positive results for area error were indicated by the addition of relative humidity (RH) at 300 mb. This is possibly due to ice crystals or the presence of upper level divergence. Donndelinger (2018) explains that a higher resolution model could likely provide even stronger positive forecast accuracy results, as the $1°$ by $1°$ GFS reanalysis data is unable to resolve airmass thunderstorms.

III. Methodology

Chapter Overview

    The purpose of this chapter is to describe the data used in this study, the setup and verification of the GALWEM GDI plots, as well as the methodology for analyzing the differences between the GDI and KI forecast for convection over the African region of interest. Both the GALWEM 00 HR forecast and GFS 00 HR analysis data, along with lightning data that will be used as truth for verification, were used for this study.

NCEP GFS Analysis Data, GALWEM Data, and GDI Calculation

    Similarly to Donndelinger (2018), the GFS analysis data was used to plot the GDI and confirm its accuracy with the National Oceanic and Atmospheric Association (NOAA) GDI forecasts. GFS analysis data provide a "snapshot" in time of the current conditions (Peng 2014). The National Center for Environmental Prediction (NCEP) GFS model analysis was downloaded from the University Corporation for Atmospheric Research (UCAR) Research Data Archive (RDA) (UCAR 2014).

    Analysis data uses a variety of observations on an irregular grid in order to produce a representation of the atmospheric state over a regular grid (Peng 2014). Creators of these analyses use a complex toolset including: statistical measures of the variability of the atmosphere itself, physical models of atmospheric behavior such as geostrophic balance, and mathematical physics models.

    In order to remain consistent with the setup of Donndelinger (2018), the GRIB2 GFS analysis data with $1°$ by $1°$ horizontal resolution was used (UCAR 2017). The data contains various parameters at pressure levels ranging between 1000 mb up to 10 mb. In order to calculate

the GDI, the temperature and relative humidity at 950 mb, 850 mb, 700 mb, and 500 mb are required. These parameters were extracted from the GRIB2 files via Matlab for the desired latitude/longitude range of 25°S - 25°N latitude and 20°W - 55°E longitude.

Similarly, the GALWEM data is also in GRIB2 format. However, the GALWEM data used in this study has a horizontal resolution of 17 km. This was the highest resolution GALWEM data available at this time for distribution and was chosen in an attempt to help resolve airmass thunderstorms, a weakness of the previous study. The GALWEM data is processed at the 16th Weather Squadron at Offutt AFB, NE. Since model data was only stored up to 10 days prior, this study only analyzes dates from late April-September of 2018, and is unable to exactly match the dates and times used by Donndelinger (2018). While this could be an area of further research, it was not seen as a limiting factor to the study due to the aforementioned results in Donndelinger (2018), which indicate that location error was lowest in the summer months for the GDI. Although the opposite was true of seasonal areal coverage, it was determined that the GDI outperformed the KI in terms of areal coverage with negligible location error differences (Donndelinger 2018). The GALWEM data also includes numerous atmospheric parameters across many atmospheric levels ranging from the surface pressure to 100 mb. However, the only variables needed to calculate the GDI are the temperature and relative humidity data at 950, 850, 700, and 500 mb.

In order to calculate the GDI in Mathematics Laboratory (Matlab), the required parameters were loaded across the specified latitude and longitude range, the empirical constants were defined, and the algorithm was setup to calculate one time file per run. Once the applicable variables were ingested, Equations 2.2-2.16 were utilized to build the resulting index. The NCEP and GALWEM GRIB2 files did not contain mixing ratio at each isobaric level, so relative

25

humidity values at each specified level were acquired in order to calculate them. To calculate

mixing ratio, the dew point temperature had to be calculated first using the relative humidity

(RH) and air temperature (T) at the desired levels (Sensirion 2001).

$$H = \frac{\log 10\,(RH) - 2}{0.4343} + \frac{17.62 * T}{243.12 + T} \qquad (3.1)$$

$$T_d = \frac{243.12 * H}{17.62 - H} \qquad (3.2)$$

Next, dew point temperature was used to calculate the saturation mixing ratio (e_s) and then the

mixing ratio (r) (Davies-Jones 2009).

$$e_s = 6.112 * e^{\frac{17.67*(T_d - 273.15)}{T_d - 273.15 + 243.5}} \qquad (3.3)$$

$$r = \frac{0.6220 * e_s}{Xmb - e_s} \qquad (3.4)$$

The "Xmb" in equation 3.4 above refers to the value of the pressure level in millibars where the

mixing ratio is calculated (i.e. 950 mb, 850 mb, 700 mb, or 500 mb). After calculation, mixing

ratios are plugged into Equations 2.5-2.7 to calculate the EPTP values at layers A-C. Once both

the temperature and relative humidity data were ingested for each isobaric level and the mixing

ratios were calculated, the sub-indices of GDI were calculated with the addition of the empirical

constants.

As stated previously in Gálvez and Davison (2016), the MWI and II are inhibiting factors

of convection and are only included in the final GDI values if their values are negative.

Furthermore, the Co index was an important factor for this study, especially when monitoring the

GDI values over the Ethiopian highlands (Donndelinger 2018).

After calculation, GDI was plotted for Africa. Initially, the Africa and Asia political and

geographical maps used by Donndelinger (2018) were used to plot the GDI, which were

accessed from the CIA World Databank II website (Pape 2004). A mapping package available

online called M_Map was downloaded for this study. This package increased color, map projection, and border options (Pawlowicz 2018). In order to determine if the GALWEM had any significant model biases, each base parameter that makes up the GDI was plotted.

Temperature and relative humidity were plotted at all four isobaric levels and potential temperature was plotted for layers A-C for three separate days and three separate times using the GALWEM data. The same procedure was done for the GFS analysis data, which was used as the observation, and each day/time plot was compared. Upon completion of this test, the variable plots for the GALWEM 00 HR forecast and the GFS 00 HR analysis resembled one another very closely in terms of shape, coverage, and magnitude. This examination further identified that the GALWEM data did not have any noticeable model biases present.

The next step was to further ensure the GALWEM GDI plots resembled the NOAA GDI forecast plots on the NCEP website. The colorbar was adjusted such that values of 10 or less were gray or black, values of 10-30 were blue or green, values of 30-40 were yellow, values of 40-50 were orange, values 50-65 were red, and values over 65 were magenta. With the minor adjustments to the colorbar, the three plots lined up quite well (Figures 3.1 and 3.2).
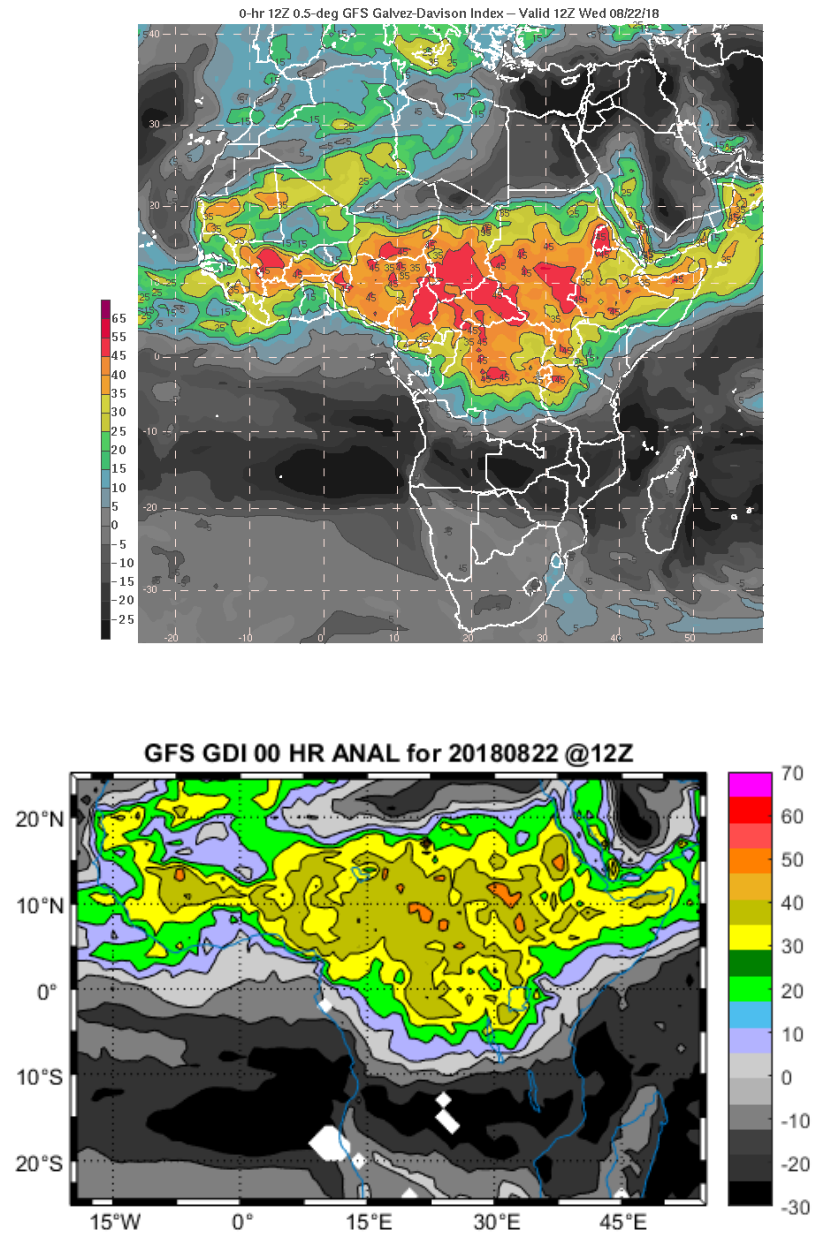
Figure 3.1: A comparison of NOAA-calculated GDI (GFS 0.5° horizontal resolution, top) and a recreation of GDI using GFS 1° horizontal resolution (bottom) for 22 Aug 2018 at 12Z.
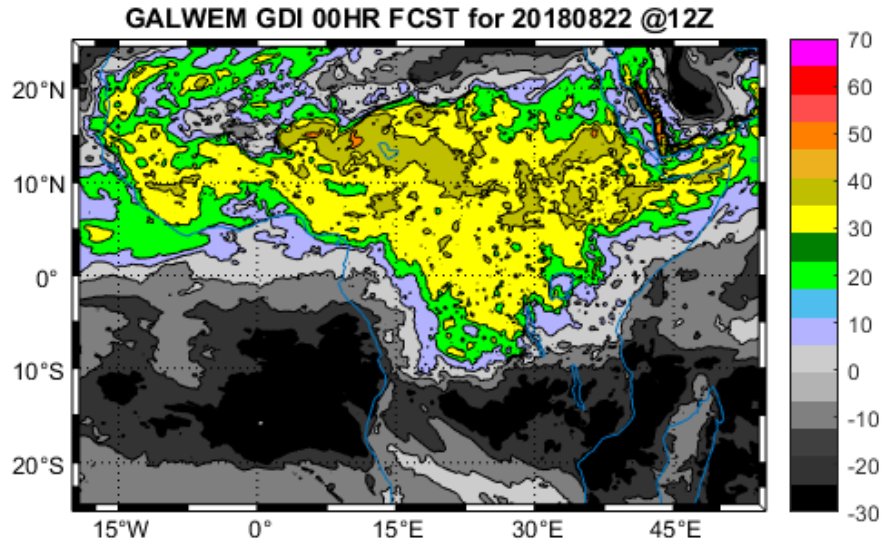
Figure 3.2: 00 HR GDI forecast for 22 Aug 2018 using 17 km GALWEM data.

K Index (KI) Calculation

Plotting KI was accomplished in a similar fashion to plotting the GDI. The KI utilized the same latitude and longitude area bounds of 25°S - 25°N and 20°W - 55°E, as well as the same M_Map projection. When calculating the KI, Equation 2.1 was used instead of Equations 2.2-2.16. Equation 2.1 required two dewpoint temperature values that are not included directly in the analysis GRIB2 files or the GALWEM 00 HR forecast files. In order to calculate these dewpoint temperatures, Equations 3.1 and 3.2 were utilized again to convert the air temperature and relative humidity at the 850 and 700 mb levels into dewpoint temperature. These dewpoint temperatures were then inserted into Equation 2.1 to calculate the KI over the study region.

Minor contour adjustments were made to match the KI thunderstorm frequency estimates (Table 2.1). A range of values from -30 to 50 were used for KI, while the GDI axis included a range of -30 to 70. Colors of GDI indices vary in increments of 10, as depicted in the colorbar on

29

the right of Figure 3.2. The KI map was made to look more similar to the GDI map with grey and black representing low KI values and no potential for convection, with green to magenta colors representing various convective potentials (Figure 3.3).
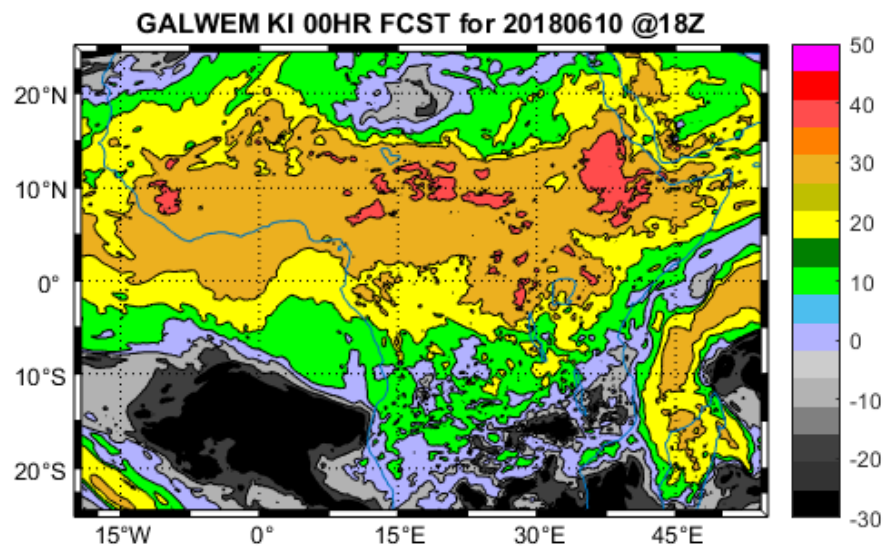
Figure 3.3: KI 00 HR forecast plotted using 17 km GALWEM data over Africa on 10 Jun 2018 at 18Z.

Plotting ATDNET Lightning Data

In order to verify the accuracy of the GDI forecasts, lightning data was plotted on the Africa map in Matlab across the entire study region. Lightning data was provided by the 14th Weather Squadron (14WS) and was collected from the Arrival Time Difference (ATD) thunderstorm detection system called Sferics or ATDNET (AFWA 2012). Sferics is a system used by the United Kingdom Meteorological Office. Sferics utilizes the arrival time differences of the signals from lightning strikes to identify location of the strikes. The ATDNET is a network of sensors for lightning detection. New Outstation (NOS) sensors monitor very low frequency

(VLF) of about 13.7 kHz, or a radio wave on the electromagnetic spectrum (AFWA 2012). This allows sensors to have a very long monitoring range. Once four NOS sites detect a signal from a lightning strike, the flash is located and recorded based on the arrival time at all four stations.

To display these strikes spatially, data extracted from these files included date, time, latitude, and longitude of each strike. The same latitude and longitude window used for GDI was utilized for lightning strikes to stay consistent. Lightning strikes were plotted as cyan asterisks over the GDI and KI plots to indicate where lightning was detected and to allow an initial inspection of index accuracy (Figure 3.4).
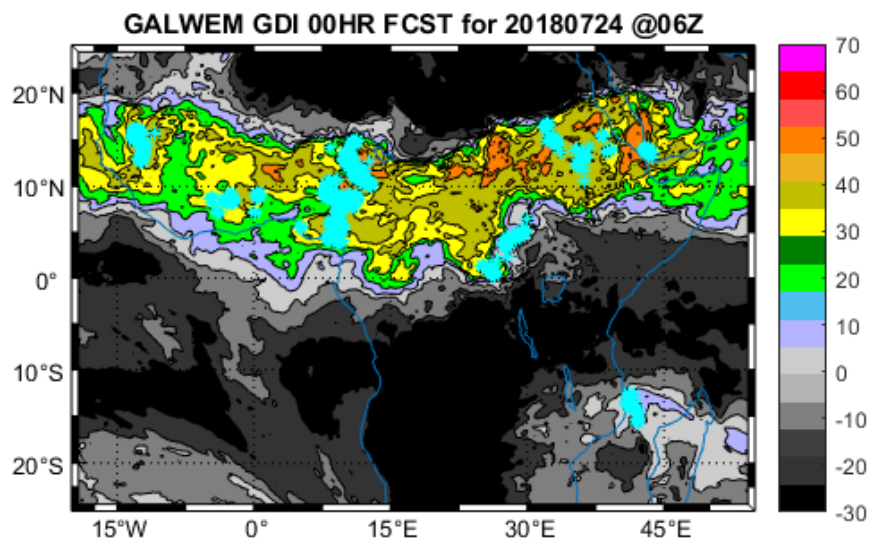
Figure 3.4: GDI using 17 km GALWEM on 24 Jul 2018 at 06Z with Sferics lightning data (cyan asterisks) for the same day and time overlaid.

NRL and *Weather.us* IR Satellite Images

Lightning data was compared to satellite images at the corresponding date and time. Most satellite imagery was acquired from the Naval Research Laboratory (NRL) Next Generation

31

Weather Satellite Project (NexSat), in partnership with the Cooperative Institute of Research in the Atmosphere (CIRA) (NexSat 2011). Some of the NexSat images were missing from the archived imagery page. For this reason, a secondary satellite source was accessed via the *Weather.us* webpage. Weather.us obtains map data from OpenStreetMap contributors, in conjunction with the GIScience Research Group at Heidelberg University (Weather.us 2018). NexSat images come from the Meteo8 satellite's infrared (IR) images, while *Weather.us* images come from the European Organization for the Exploitation of Meteorological Satellites (EUMETSAT). Both IR images use a color filter that highlights cold cloud top temperatures of -20°C or colder. The NexSat images cover the majority of the African continent, with only a few degrees of longitude not captured on the eastern edge of the image (Figures 3.5). Imagery from *Weather.us* covers the entirety of the African continent with similar resolution to the NexSat imagery (Figure 3.6).
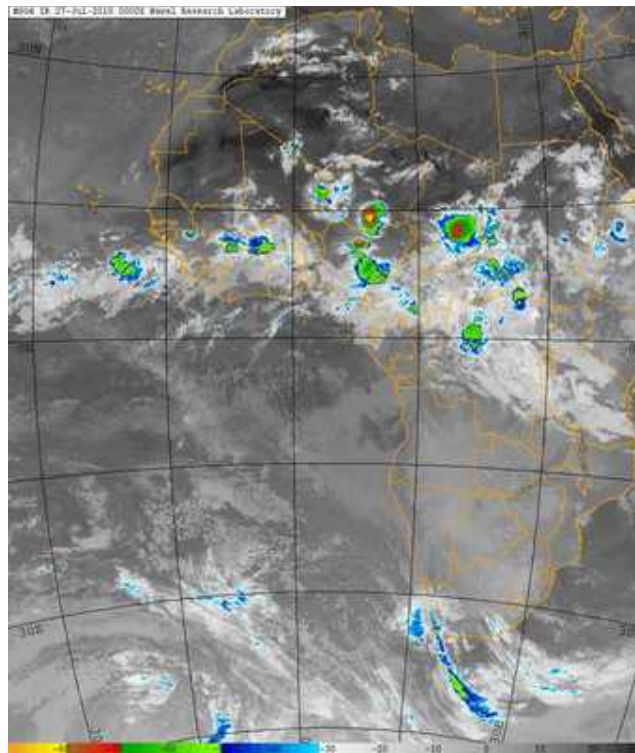
Figure 3.5: NexSat Meteo8 color IR satellite imagery over Africa on 27 Jul 2018 at 00Z with cloud top temperatures (°C) indicated by the filter on the bottom of the image.
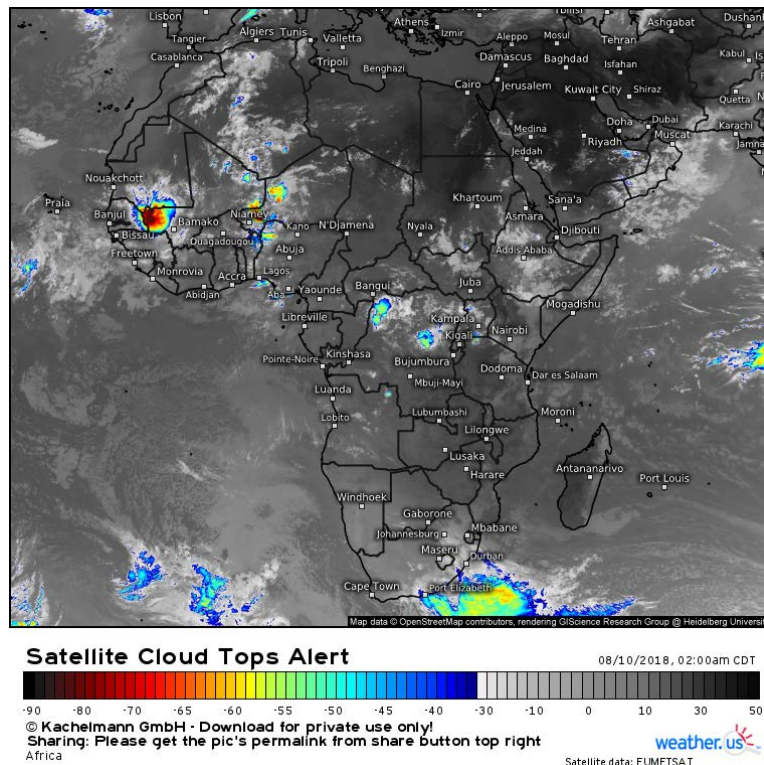
Figure 3.6: *Weather.us* EUMETSAT color IR satellite imagery over Africa on 10 Aug 2018 at 06Z with cloud top temperatures (°C) indicated by the filter on the bottom of the image.

After the lightning was plotted on the index forecast image, the lightning strikes were compared to the IR satellite imagery from the same time frame in order to ensure the strikes were associated with cold cloud tops. When referencing forecast model skew-T profiles, it was noted that the freezing level over Africa was between 550-500 mb or 16,000-19,000 feet (ft). In order for cloud electrification to occur, frozen drop or graupel particles must be present. Most lightning that occurs over Africa was associated with 40 dBZ echoes reaching a height of 8 km, approximately 26,000 ft, with clouds tops extending above that height (Toracinta et al. 2001). The -20°C level was approximately 25,000 ft aloft on model skew-T profiles in December, which corresponds to the white shades on the Meteo8 colored IR imagery used in this study (Donndelinger 2018). If lightning strikes did not match up with areas of appropriate cloud

33

heights, they could be removed. During the comparison between each satellite image and the plotted lightning strikes, all lightning strikes were kept.

Methods for Comparing Index Forecasts

Remaining consistent with methodology used in Donndelinger (2018), the clustering analysis method was used in the research. Clustering analysis has been used in several similar studies including identification of storms, clouds and precipitation fields (Marsban and Sandgathe 2005, Singh and Gill 2013). Cluster analysis recognizes specific features in both forecast and observations fields for the purpose of comparing their characteristics (Singh and Gill 2013). In the case of this study, the lightning and forecast data are grouped into the same number of clusters, or grouping of data points, then observation and forecast clusters are matched via geographical proximity and their location and spatial coverage differences are noted. Differences in location are referred to as location error and spatial or coverage differences are referred to as area error. This verbiage was repeated in this study to remain consistent with Donndelinger (2018). Lightning was used for verification, so the number of lightning clusters was chosen as the observed cluster while the index (GDI or KI) cluster was the forecast cluster. Although the GALWEM offers a higher resolution data set than the GFS 1° by 1° analysis data, lightning strikes occur at scales smaller than 17 km, and therefore cluster analysis was the most effective solution instead of a point-by-point method.

K-Means Clustering Method

K-means clustering focuses on idealizing the number of clusters to divide the data points amongst by balancing the number of clusters with the total sum of the distances between the data points and their centroids (Singh and Gill 2013). A centroid is the center of a cluster and is

calculated by averaging the locations of all the points within a cluster. K-means clustering groups data points in Matlab by randomly placing k number of centroids in the data and assigning each data point to the closest centroid (Singh and Gill 2013). The distance of each data point to the centroid is then summed. Next, Matlab randomly replaces the 'k' number of centroids throughout the data again and places the data points into the new clusters. This was done 10 times for each k number of clusters picked and the smallest sum of distances between data points and centroids was saved.

The number of clusters was first set to one and the lowest total sum of all distances between each data point and the centroid was recalled (Donndelinger 2018). Then, the same sum of distances was calculated with two, three, four, etc. clusters, up to 10 clusters. Once all the sums of distances were saved, the idealized number of clusters was identified using what is referred to as a k means plot (Figure 3.7).
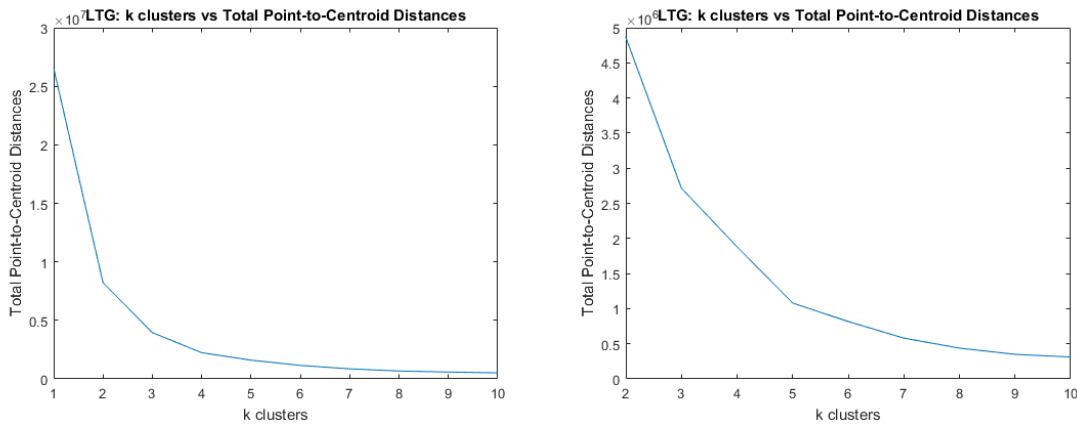
Figure 3.7: An example k means plot, full view from 1-10 clusters (left) and a zoomed-in view of 2-10 clusters (right), highlighting the curve indicating the ideal number of clusters, 5.

The total sum of distances between each data point and the centroid of the lightning cluster yielded total distances on the order of 10^6 and up to 10^7, as shown on the y-axis (Figure 3.7). This makes choosing an ideal number of clusters difficult, so a plot focusing on the rapidly changing number of point-to-centroid distances was created to highlight the ideal number of

35

clusters. The k means cluster plot emphasizes the decrease in total point-to-centroid distance

with increasing cluster number, k (Singh and Gill 2013). In the example above, 5 clusters are

chosen for k as 5 is the last increase in cluster number associated with a significant decrease in

total point-to-centroid distance. The ideal, k, number of clusters is found at the bottom of the

"knee" or "elbow" made by the curve in the k means plot or the last, sharp change in slope on the

plot. Beyond this point on the curve, the total sum of distances does not significantly decrease

with additional clusters. By using this method, the number of clusters was chosen objectively

based on the k means plot of the lightning data at each timeframe. The ideal number of clusters

was then applied to the lightning data and the GDI was analyzed at each particular time.

Error Analysis Method

Error analyses were conducted to assess forecast quality of the applicable index at each

desired timeframe. Observed lightning data are plotted along with the desired index over the

Africa map for a chosen time (Figure 1.1). Only the data points that indicated scattered

thunderstorms were likely to occur were kept. The scattered thunderstorm threshold of 35 or

greater was set for the GDI, while values of 30 or greater were kept for the KI (Figure 2.6 and

Table 2.1) (Donndelinger 2018). An example of the resulting lightning and scattered

thunderstorm threshold data can be seen in Figures 3.8 and 3.9.
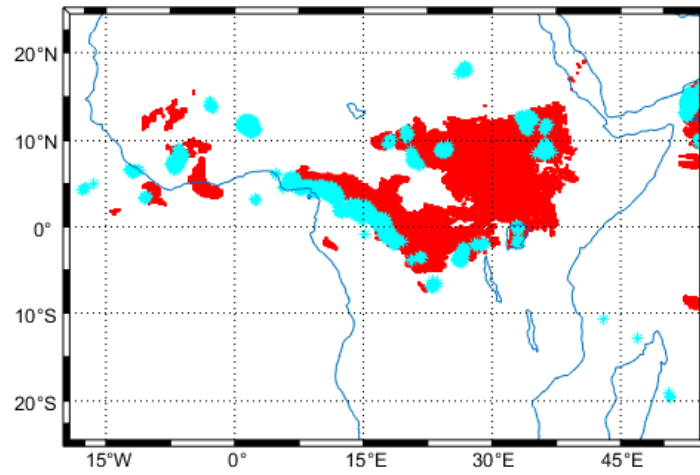
Figure 3.8: Lightning data plotted with cyan asterisks and GDI values 35 or above plotted with red dots on 24 May 2018 at 00Z.
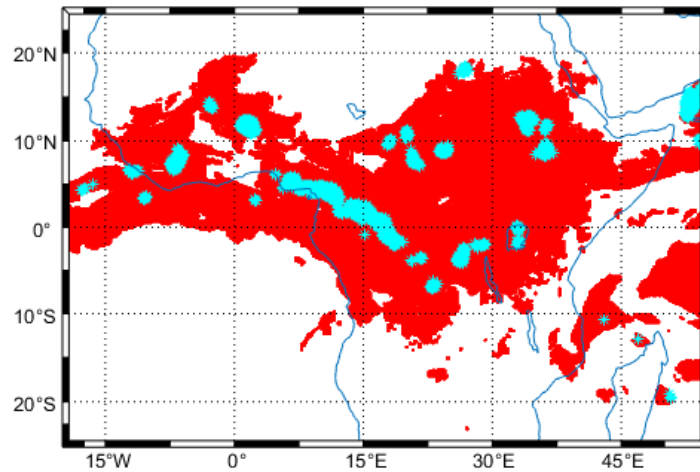
Figure 3.9: KI values 30 or greater plotted with red dots and lightning data plotted with cyan asterisks on 24 May 2018 at 00Z.
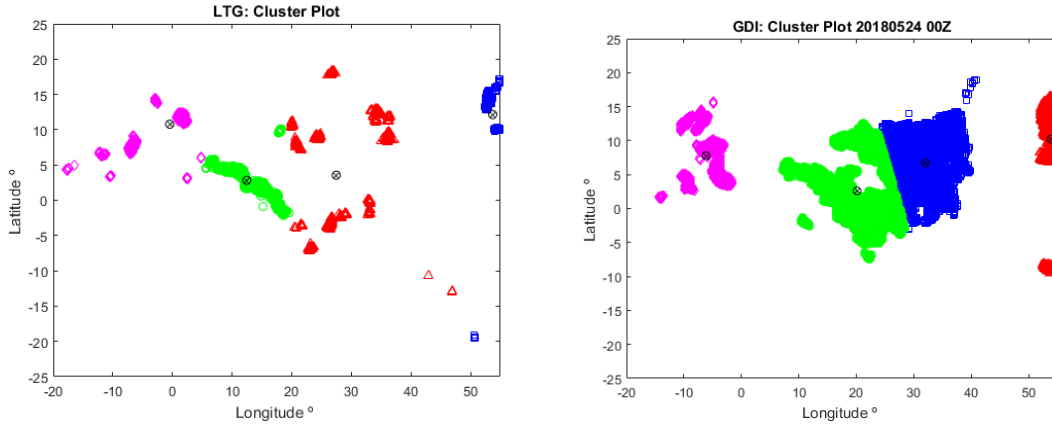
Figure 3.10: Lightning data (left) and GDI at or greater than 35 (right) divided into clusters on 24 May 2018 at 00Z.

Then, the lightning data were divided into the ideal number of clusters using the method described above (Chapter III, K-Means Clustering Method). Once the ideal number of clusters was determined, both the lightning and index data at or above the scattered thunderstorm threshold were divided into as many clusters (Figure 3.10). Specified colors were assigned to clusters with lightning cluster one not always lining up with index cluster one. Clusters were matched by the researcher examining clusters and paired based on geographic proximity. After clusters had been matched, the location and area error were calculated.

Clustering allows the researcher the ability to assess both location and area errors. These factors were calculated with the following method:

Location Error = Distance between forecast cluster centroid and observed cluster centroid

Area Error = Average distance between data points and forecasted cluster centroid – average
distance between data points and observed cluster centroid

Area error represents the expanse of a particular cluster, with each point-to-centroid distance weighted equally. Area error is the difference between the paired cluster's average point-to-centroid distances. When assessing how well a forecast cluster compares to the observed cluster, one should observe the location and areal coverage of the clusters in question. Both of these error

38

calculations were calculated for each cluster pair at each time. Location and area error values from each cluster pair were averaged for each of these timeframes.

GALWEM data for this study spans various days from late April through late September 2018. In order to have a sufficient number of study days and times, the 10th through 15th and 22nd through 26th of each month was selected for analysis with every six-hour period of 00Z, 06Z, 12Z, and 18Z covered for the selected day. Once the error values were calculated across all days and times, the error data was organized by month, Zulu time, convective regime, and West and East Africa.

For monthly analysis, data was collected across all days and times for each particular month. Then, the GDI and KI location and area errors were compared at the 95% confidence level to determine any monthly trends. While data could only be collected from late April through September, it was noted in Donndelinger (2018) that the location error was largest in the winter months, making this less of an issue for this study.

Next, the location and area error data were sorted according to Zulu time. This method allowed for at least 48 hours of separation between cases, which is generally enough time to allow for a change in weather patterns. After this, convective regimes were analyzed.

Convective regimes were determined subjectively by analysis of colored IR satellite imagery obtained via the Naval Research Laboratory and *Weather.us* websites (NexSat 2011; Weather.us 2018). To remain consistent with Donndelinger (2018), four convective regimes were used to categorize the cases: airmass thunderstorms (AT), Mesoscale Convective System (MCS), airmass predominate with MCS (AT/MCS), and MCS predominate with airmass thunderstorms (MCS/AT). The location and area error were analyzed for each regime across all times to determine which convective pattern, if any, the indices forecasted most accurately.

Lastly, in order to determine if the indices exhibited lower location error in one region compared to the other, and compared against the other index, new lightning data was requested for West and East Africa. The dividing line for West and East Africa was chosen as 25°E longitude, as a meridional line drawn here represents an accurate division of the western and eastern portions of the continent (Figure 3.10). This dividing line also allows for fairly even distribution of the Southern Hemisphere land area between the west and east regions, as well as separation between the highlands to the east and the monsoon region to the west.
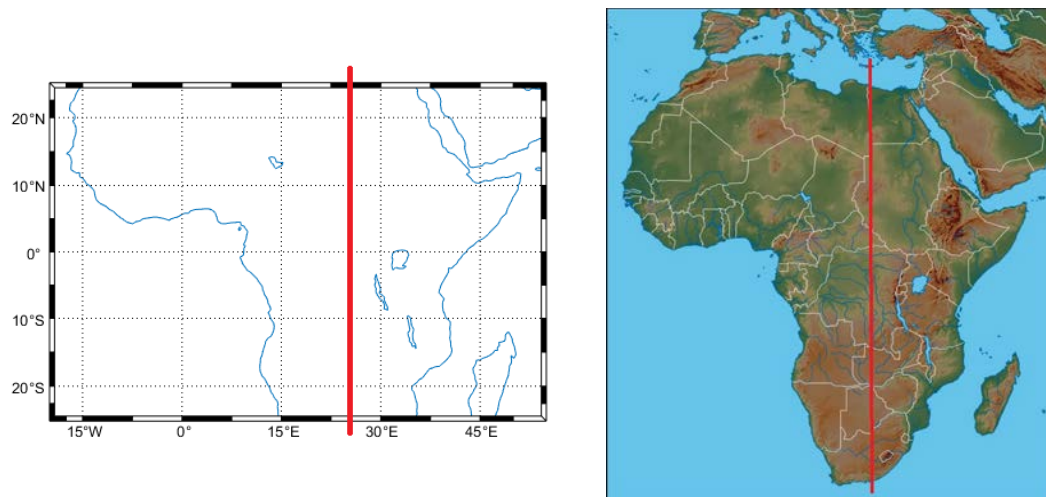
Figure 3.11: Coastline map of the region of interest (left) and topographic/land cover map (right) with vertical red line along the 25°E longitude line indicating the east and west boundary line (King 2006).

Bootstrapping Statistical Method

Bootstrapping is a statistical method used to expand a data set by inflating it without alteration of its characteristics for statistical analysis. Bootstrapping is based on the law of large numbers, making it a suitable method for creating sufficient data in order for the empirical distribution to be a good approximation of the true distribution (Orloff and Bloom 2014). This technique has been well known since the 1970s, but only became practical in more recent decades with high-speed computational resources to implement the method. Computations are

40

conducted on the data itself to estimate the variation of statistics that are computed from the same data (Orloff and Bloom 2014). In order to allow for independent cases that included variation in weather patterns, all the even days were chosen across the range of collected data. These days were the 10th, 12th, 14th, 22nd, 24th, and 26th. Four times were analyzed for each day including the 00Z, 06Z, 12Z, and 18Z times. GALWEM data was collected from the 22nd - 26th of April and then the 10th - 15th and 22nd - 26th of each month for the months of June-September. This resulted in 33 cases for each Zulu time.

The bootstrapping statistical analysis was done in several ways. First, all error data across all dates and times were ingested. Different means were then calculated for each timeframe. The code then sampled the given error data with replacement and calculated an artificial mean value. Each artificial mean value is close, but not necessarily equal to, the actual mean of the data. 10,000 artificial means were calculated from each data set to achieve a quality estimate of the 95% confidence interval (Orloff and Bloom 2014). The 95% confidence level is considered to be high confidence and is the desired level for this research. Bootstrapping allows researchers to estimate confidence intervals with high accuracy, even with small data sets.

There are multiple ways in which confidence intervals can be calculated from bootstrapped data. For a 95% confidence interval, the percentile method would use the critical values of .975 and .025, or the 9,750th and 250th largest values in a data set with 10,000 members as the end points above and below the actual mean, respectively (Orloff and Bloom 2014). Another, and more accurate method, is the bias-corrected and accelerated (BC_a) method (Efron and Tibshirani 1993). The BC_a method comes closest to fulfilling the standard of good confidence intervals, meaning they closely resemble exact confidence intervals and give dependably accurate coverage probabilities in all situations (Efron and Tibshirani 1993).

Confidence intervals constructed using BC_a are more accurate overall and recommended especially for small sample sizes, such as the limited MCS cases in this study (Wilks 2011). The BC_a method is more advanced due to its incorporation of the cumulative distribution function (CDF) of the standard Gaussian distribution along with a bias correction parameter that reflects median bias of the bootstrap distribution to account for partiality (Wilks 2011). This method also includes the acceleration parameter, which corrects for the skewness of the data. The BC_a method produces more accurate confidence intervals by incorporating more parameters into its calculation that encapsulate the characteristics of the data.

BC_a confidence intervals are calculated using the desired number of samples (10,000 in this study), the desired calculation (averaging), and the data for calculating the confidence intervals. Error bars were plotted using the errorbar function with the mean of the data set, the lower bounds, and upper bounds of the confidence interval as inputs. Confidence intervals for each data set were calculated and plotted on graphs (Figure 3.12). A 95% confidence interval is shown, where 95% of all possible mean values fall into the range encapsulated by the lower and upper error bar boundaries.
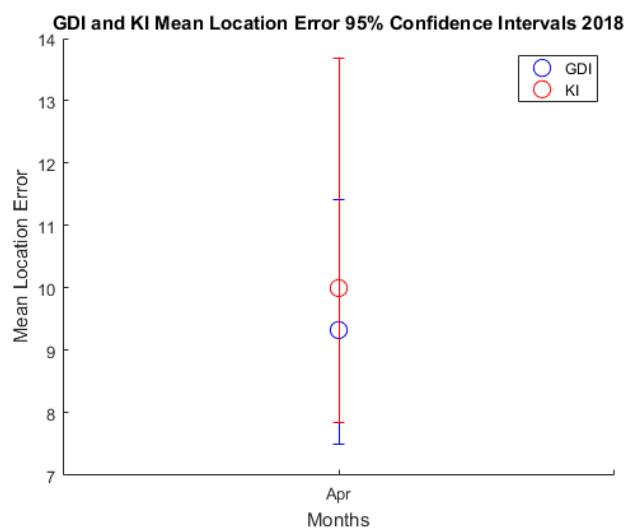
Figure 3.12: Sample confidence interval plot with 95% confidence interval (error bars) for the April 2018 GDI location error.

Confidence intervals were created for location and area error data using this method for each index across all days and times.

Summary

In order to conduct an error analysis of convective index forecasts in this study, the following methodology was implemented. First, convective indices were plotted using the GALWEM 00 HR forecast data, with lightning overlaid and validated using IR satellite imagery from the same timeframe. Then, the lightning and index data were separated into the same number of clusters using the k-means clustering method. Paired clusters were examined to calculate both location and area error values. Lastly, the error data was expanded using bootstrapping statistical methods and confidence intervals were calculated using the BC_a method.

IV. Results and Analysis

Chapter Overview

The purpose of this chapter is to analyze and discuss the results of the monthly, respective Zulu time, convective regime, regional, and GDI-A studies. A brief model and resolution comparison is also made between the GFS and GALWEM. Furthermore, a short discussion on Kelvin waves and their connection to forecast accuracy is included. The location and area errors are discussed to quantify how far off the forecast clusters were from the observed lightning clusters.

Monthly Study

As mentioned previously, data was collected from late April through late September of 2018 because the 16th Weather Squadron was only able to pull data from ten days prior. Based on the small sample size for each month, all times (00, 06, 12, and 18Z) were used for each monthly analysis. April data comprised the 22nd, 24th, and 26th of the month with four times for each day, resulting in 12 total samples. All other months included the 10th, 12th, 14th, 22nd, 24th, and 26th of the month with the same four Zulu times for a total of 24 samples.

For the original cases across all dates and times, the highest location error for GDI was found in May and the lowest location error for GDI was determined to be in the month of July. The highest and lowest area error for GDI was found to be in the months of August and May respectively. Similarly to the GDI, the location error for the KI was calculated to be the highest in May. The location error for the KI was lowest in August. The highest and lowest monthly area error for KI was determined to be in the months of April and July, respectively.

Next, the location and area errors were bootstrapped for each set of monthly data to ensure robust confidence intervals were being calculated and the 95% confidence interval was calculated for the bootstrapped data set. The monthly location and area error confidence intervals are plotted in blue for GDI and red for KI (Figure 4.1). The closer an error is to zero indicates the closer the forecast (respective index) is to the detected lightning strikes (observation). Results indicate that GDI and KI mean location error are relatively close in the spring and early summer months (April, May, and June) but begin to show some separation in the mid-to-late summer months (July and August) into the Fall (September). This indicates a departure from the results of Donndelinger (2018), in which the furthest separation of the location error between the two indices was shown in May and the August location error means nearly overlapped (Donndelinger 2018). In fact, the GDI and KI May data location errorbars for the 95% confidence level are actually the most similar among the months in this study. However, confidence intervals across all months overlap at the 95% confidence level, placing less confidence that one index's forecast is more accurate than the other's.

Further comparison of these location forecasts for monthly location error shows a decrease in the mean location error from May to July for GDI, and an overall negative trend in KI location error mean for KI as well. This is in line with the results of Donndelinger (2018), which show a decrease in location error between the spring and summer months for both GDI and KI (Donndelinger 2018). Upon further analysis of the GDI and KI location error for August, the 90% confidence intervals no longer overlap, indicating that it can be said with 90% confidence that KI decreases location error when compared to GDI in the month of August (Figure 4.2). This result is interesting and could relate to KI's relative skill at airmass thunderstorm forecasting. This will be discussed more in the convective regime study. Overall,

45

the GDI and KI performed similarly in terms of location forecast across the monthly study period.
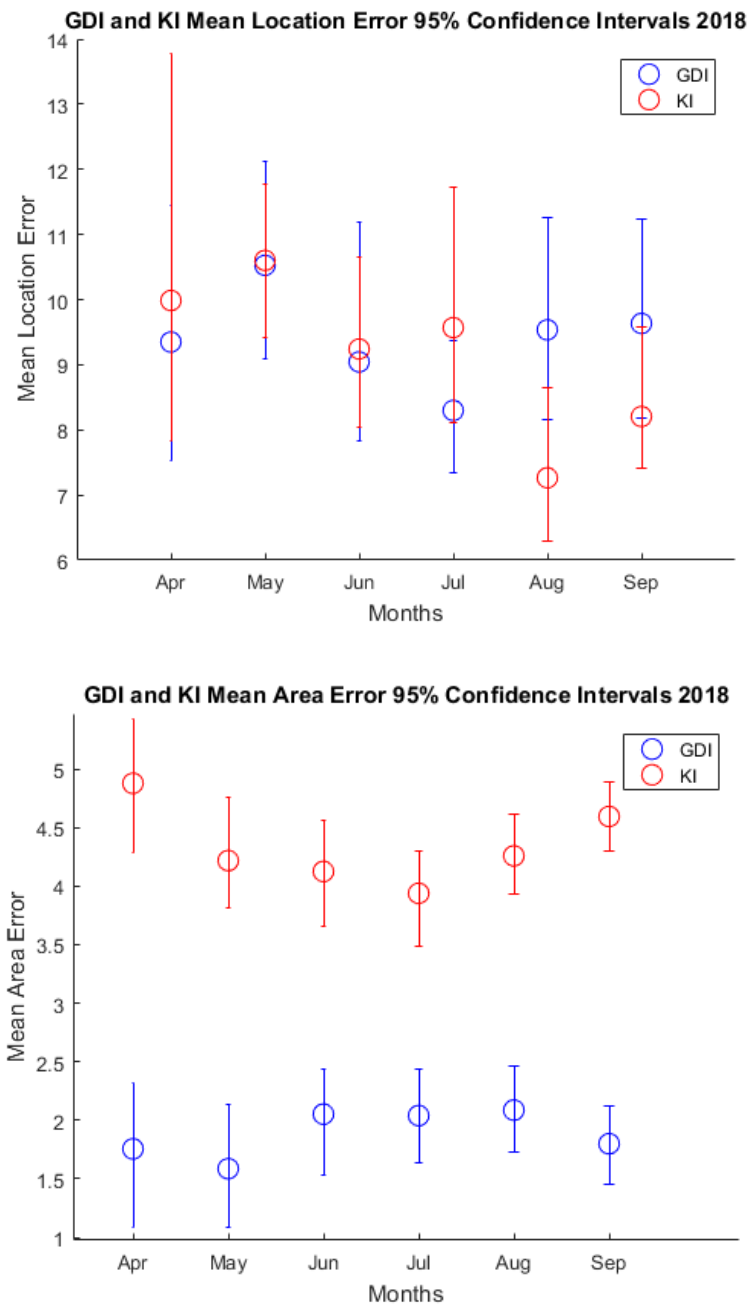
Figure 4.1: Monthly GDI/KI location (top) and area (bottom) error confidence intervals at the 95% confidence level.
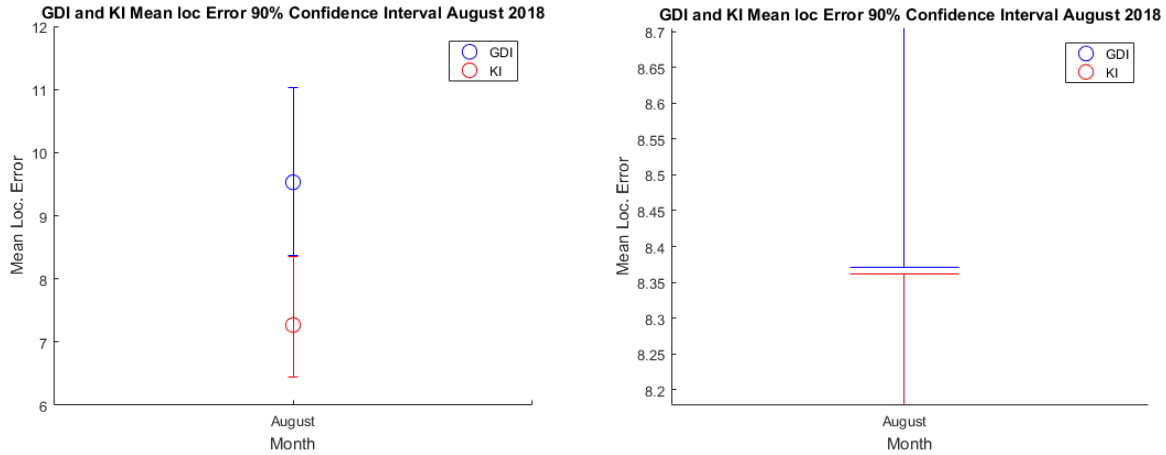
Figure 4.2: 90% Confidence Interval for the total location error (left) and zoomed-in location error (right) for August showing separation between GDI and KI.

Zulu Time Study

After the monthly data and confidence intervals were calculated and analyzed, the error data were further analyzed by each Zulu time. For the GDI, the highest and lowest location error was calculated to be the 12Z and 18Z times, respectively. The highest and lowest area error for the GDI was determined to be 00Z and 18Z, respectively. For the KI, the highest location error was found to be among the 06Z cases, with the highest area error a tie among the 00Z and 06Z times. The lowest location and area error was found to be in the 18Z cases for the KI. The bootstrapped 95% confidence intervals for location and area error across each Zulu time for both indices is shown in Figure 4.3. The Zulu time appears to have a slight correlation to the convective regimes. This will be discussed in the next section.
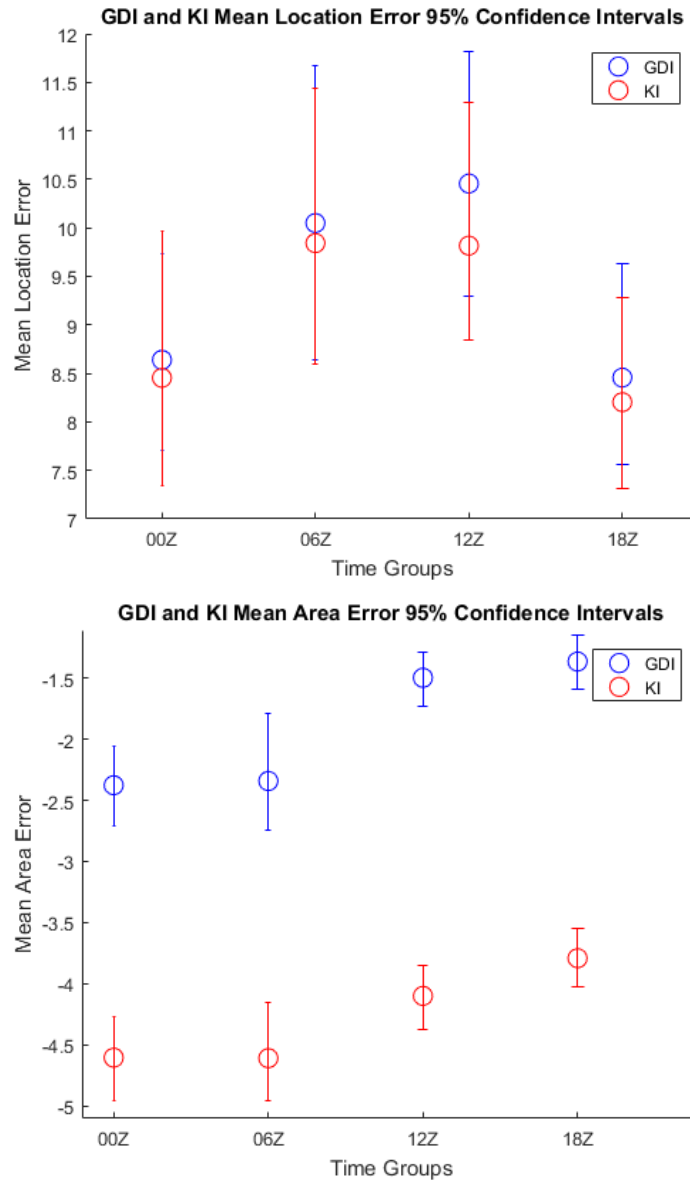
Figure 4.3: 95% confidence intervals for GDI and KI location (top) and area (bottom) errors across each Zulu time.

Convective Regime Study

The third analysis technique grouped similar convective regime cases together to determine forecast accuracy, as well as any possible trends in the location and area error for each predominate thunderstorm type. First, purely airmass thunderstorm days were grouped together across all times and their location and area errors were averaged. The four convective regimes

were kept from the previous study to keep consistency. These four convective regimes are as follows: purely airmass thunderstorms (AT), purely MCS convection (MCS), predominately airmass storms with MCS convection present (AT/MCS), and predominately MCS convection with airmass storms present (MCS/AT). The highest and lowest location error for the GDI was found to be in the MCS and AT cases, respectively. For GDI, the MCS cases also exhibited the highest area error while the AT/MCS cases exhibited the lowest area error. Therefore, when using the GALWEM, the GDI performs best when the primary convection type is airmass thunderstorms and worst when the primary convection type is MCS.

For KI, the location errors all fell within .092 degrees of one another, suggesting the KI performs with similar accuracy no matter the convective regime. However, the location error was highest among the AT cases, with the lowest location error a tie between the MCS and AT/MCS regimes. This suggests the opposite skill of the GDI in that the KI performed best when the primary convection type was MCS-based, and worst when the primary convection type was airmass thunderstorms. These results are interesting because they differ from the results for GDI that Donndelinger (2018) found. In the previous study, Donndelinger (2018) determined that the location error for GDI was the highest when the predominate source was airmass storms, while the lowest location error for GDI was achieved when the predominate convection source was from MCSs. This suggests that the higher horizontal resolution model is able to more accurately forecast the location of smaller convective systems. Furthermore, Donndelinger (2018) found that the GDI was able to outperform KI in the predominately MCS cases but was not able to outperform KI in the predominately AT cases at the 95% confidence level. In this study, the GDI consistently had a higher mean location error than the KI, but similar to Donndelinger (2018), results indicate this is not significant at the 95% confidence level. Another similarity between

49

this study and Donndelinger (2018) is that the mean GDI location error fluctuated much more than the KI. Most importantly, all of the location error confidence intervals overlap, and therefore no one index can be selected with 95% confidence over the other index when they have the same convective regime.

Initially, it was thought that connections could be drawn between the Zulu time analysis study and the convective regime analysis study. Since it was observed that the AT regime exhibited the lowest location error of the four convective regimes, determining the distribution of these regimes by Zulu time provides insight to this theory. For this study, there were 47 AT cases. In the previous Zulu time study, the 18Z and 00Z times exhibited the lowest and second lowest location errors overall, respectively. Furthermore, the location errors of the 18Z and 00Z timeframe were lower than the 06Z and 12Z timeframe location errors by about 1.5 degrees each. There were 7 AT cases for the 18Z timeframe and 7 AT cases for the 00Z timeframe. Therefore, only 14 of the total 47 AT samples fall during these two timeframes. Furthermore, the most AT cases (21) of any timeframe actually occurred 12Z. The 12Z timeframe had the highest location error of all four Zulu time groups. This is quite counterintuitive because airmass storms are generally most prevalent during the afternoon. For the aforementioned reasons, it can be concluded that no correlation exists between the Zulu time and the convective regime location error. The confidence intervals for each convective pattern are shown in Figures 4.4 and 4.5.

The location error for purely MCS storms exhibits the largest error bar variation due to the 14 June 00Z example, which had location errors of 22.55 and 16.92 degrees for the GDI and KI, respectively. It was decided that this time should still be included due to the small sample size of 12 for the purely MCS cases.
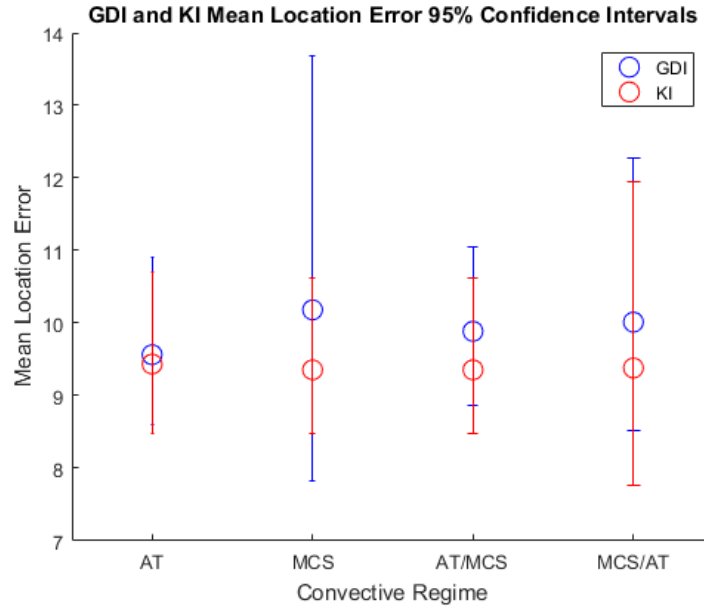
Figure 4.4: 95% confidence intervals for GDI and KI location error across convective regimes.
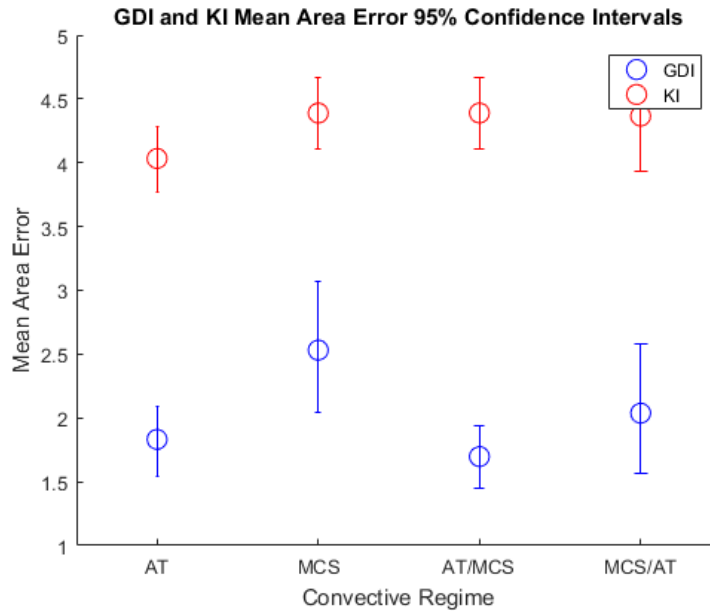
Figure 4.5: 95% confidence intervals for GDI and KI area error across convective regimes.

Regional Study

The GDI was developed for the tropics and performs particularly well in the 15°-25° latitude belts, especially over oceans and eastern fringes of continents where trade wind climate prevails (Gálvez and Davison 2016). Initial trends appeared to support lower area error over the

51

western half of the African study region, providing motivation to test the above finding by Gálvez and Davison. Therefore, the African study region of 20°W - 55°E and 25°S - 25°N was divided into West and East Africa using a subjective dividing line of the 25°E longitude line (Figure 3.11). New lightning data was requested from the 14th Weather Squadron that encompassed the new West Africa region (20°E - 25°E) and the new East Africa region (25°E - 55°E). Next, the same methods described in Chapter III were applied for all sampled days and times across the west and east to calculate location and area errors for each region.

Based on time permitted, these errors were not further tested by month, Zulu time or convective regime, although this would be a useful expansion of the current research. Once the location and error areas of both the GDI and KI were calculated for each region and bootstrapped, the 95% confidence intervals showed that the overall location error mean for the West African region was lower than location error mean for the East African region. One interesting note is that the KI outperforms the GDI in the west for location error while the opposite is true in the east. Furthermore both indices had a lower location error for West Africa than East Africa. However, neither of these results can be concluded with 95% confidence for either region (Figure 4.6).

The area error was overall very close in both the west and east for like indices with the GDI significantly outperforming the KI. Unlike the location error, these results were significant at the 95% confidence level, and possibly higher, for area error (Figure 4.7).
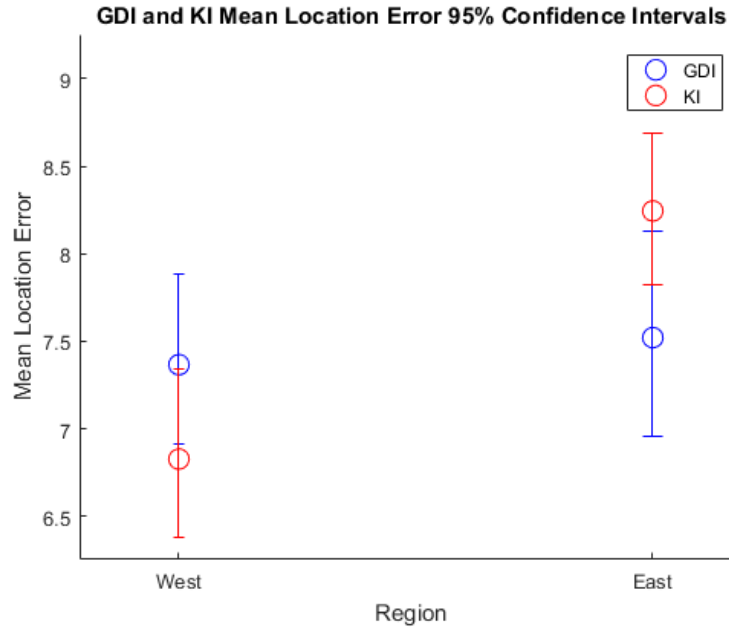
Figure 4.6: 95% confidence intervals for GDI and KI location error for West and East Africa.
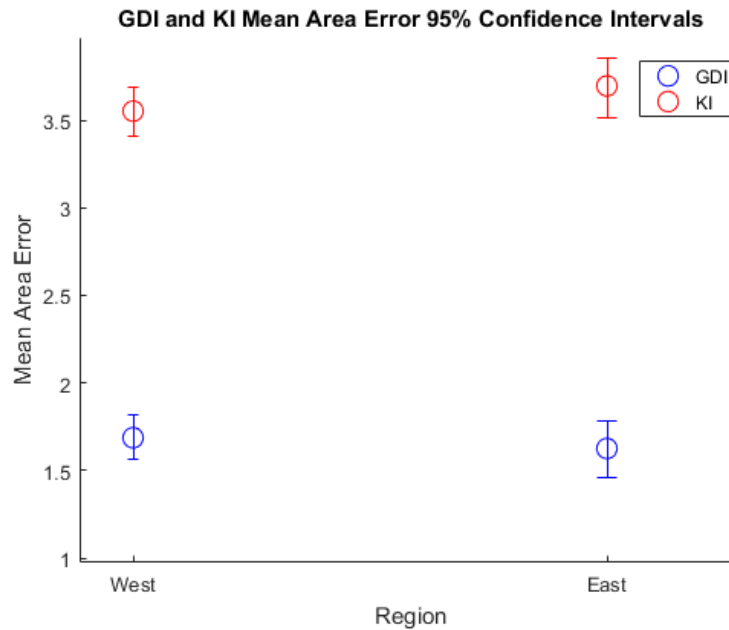
Figure 4.7: 95% confidence intervals for GDI and KI area error for West Africa and East Africa.

Although the GDI location error for the west is only about .2 degrees less than the location error for the eastern GDI, it is still interesting that this contradicts the findings of Gálvez and Davison. This could be due to several factors. First, only 33 days were sampled across 6 months. This is by no means an accepted population size for a climatic data study. Generally, the

53

meteorological community accepts 30-year data sets as a substantial population size for climate studies (Wuebbles 2017). Access to GALWEM reanalysis data would allow a more robust and trustworthy data set and is considered an area of future research. Furthermore, the Saudi Arabian Peninsula was included in the East African study region. Saudi Arabia is notoriously arid, especially in the low-levels, and this makes the GDI a very unsuitable convective index for the region due to its preference for deep layers of moisture. If possible, it would be ideal to exclude Southwest Asia from this study to determine quantitatively if this improves the East Africa error. Another possibility for the higher location error mean in the east could be because the GALWEM under-forecasts orographic precipitation due to smoother orography (Boyle 2016). This would create an issue in East Africa, as the Ethiopian highlands, Kenya, and Tanzania provide a broad region for orographic lift and precipitation. Overall, West Africa has a lower elevation than East Africa. Another possible reason that the location error mean was lower overall in West Africa compared to East Africa could be related to Kelvin wave influence on precipitation and convection during. This study covers the late spring through early fall months of the Northern Hemisphere (April – September). As previously stated in Chapter I, Kelvin waves modulate African precipitation, especially along the equator and during the West African Monsoon period (April-July). Therefore, Kelvin waves could be aiding the convective indices' forecast, especially for the KI, which showed significant difference in location error between West and East Africa. Lastly, both indices seemed to have some trouble with convection in the far southern portions of the study region. Although these regions are within the 15°-25° latitudinal belt for which Gálvez and Davison state the GDI works exceptionally well, there were several examples in this study where this skewed the location error for that particular timeframe. The poor forecast accuracy in Southern Africa is probably because the dates used in this study

encompass the Southern Hemisphere winter (April-October), which generally coincides with the dry season (Zijlma 2018). Donndelinger (2018) found that location error was highest during the winter months, so this correlates well with this finding.

Model Comparison Study

Since the GALWEM was used in this study and Donndelinger (2018) used the GFS, it was imperative that a brief comparison of like data sets should be completed. Although Donndelinger (2018) focused mainly on 2016 cases and this study focused on 2018, like months can be compared due to similar climate patterns in the tropics. This allows conclusions to be drawn about model performance. It has been noted that the GFS data used in Donndelinger (2018) was 1° horizontal resolution while the GALWEM data used in this study was 17 km horizontal resolution. The higher resolution model data for GALWEM was requested in an attempt to improve upon the poor forecast accuracy of airmass thunderstorms using the GDI and KI via GFS reanalysis data. The 17 km GALWEM data was the highest available horizontal resolution data available for download and would therefore aid in the resolution of terrain, smaller-scale storms, and other weather features. While this theory is sound, the results show the opposite effect for this comparison. Higher location error was noted between bootstrapped means of the GDI in all matching 2016 and 2018 months, and two out of three matching months for KI (Figure 4.8). This result could indicate that the 17 km data is not high enough to fully resolve airmass thunderstorms.

The GALWEM is based on the United Kingdom Meteorological (UKMet) Office's Unified Model. The GALWEM, like the Unified Model, is a grid point model. The 17 km horizontal resolution of this model indicates that there are 17 kilometers between each grid point.

The smallest features that can be forecast in a grid point model should have full wavelengths of five to seven grid points (Colorado State 2003).
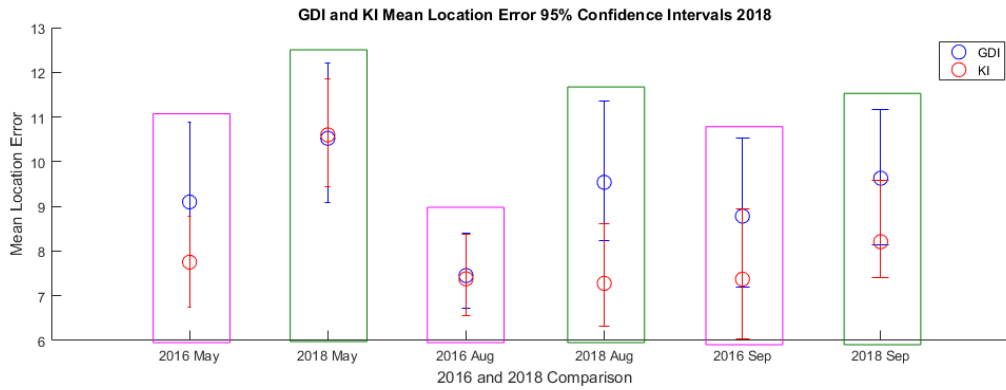
Figure 4.8: Similar month 95% confidence interval comparison between the current and Donndelinger (2018) study showing location error. Pink outline indicates 2016 months and green outline indicates 2018 months.
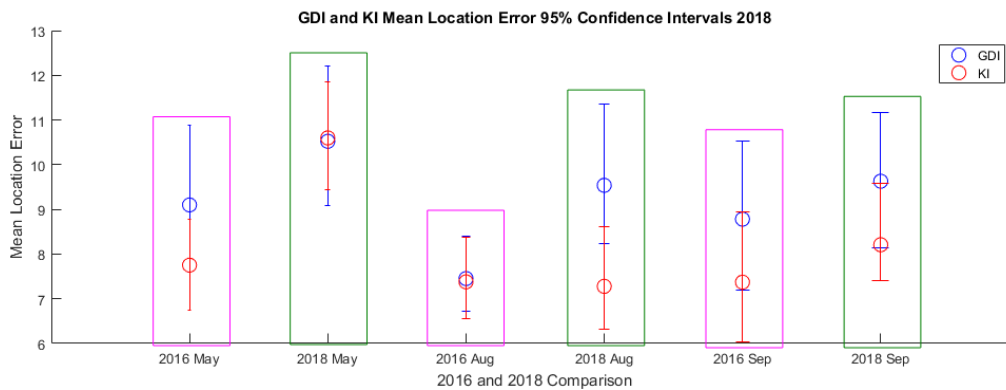
Figure 4.9: Similar month 95% confidence interval comparison between the current and Donndelinger (2018) study showing area error. Pink outline indicates 2016 months and green outline indicates 2018 months.

This means that a horizontal resolution of approximately 4 kilometers is needed to fully resolve a typical airmass thunderstorm, which is on the order of 24 km in diameter (NWS 2018). While this very high resolution was not available at this time, repeating these studies with data using at least 4 km horizontal resolution would be a useful extension of this research. Furthermore, an interesting trend was present for the area error in the like-months study.

When comparing the 2018 months with the 2016 months, it can be noted in Figure 4.9 that the GDI had lower area error in each case. The constant improvement for areal thunderstorm

coverage has been one of the most significant findings of this study. Donndelinger (2018) found that the GDI outperformed the KI in terms of areal thunderstorm coverage in all studies except the intra-seasonal study, when convection was predominately from airmass thunderstorms. In this study, the GDI consistently outperformed KI under all situations, including airmass thunderstorms, and the difference between the area error values of like months, as well as between the GDI and KI, appears to be even more significant when using the 17 km GALWEM data. The consistent reduction in area error for GDI was promising and could possibly be even more significant if a higher resolution data set were used.

GDI-A Study

In the previous study, Donndelinger (2018) tested several additions and alterations to the GDI in an attempt to tune the index to African thunderstorm forecasting and more specifically, to reduce the location error of the index. It was determined that average vertical velocities, upper-level potential temperature proxies, and upper-level relative humidity additions to the GDI, either had little-to-no effect on the location error, or actually increased the location error of the forecast. However, the previous study noted that the low and mid-level relative humidity and equivalent potential temperature proxies each showed reduction of location error for the sampled days in August 2016. While these exact dates were not available for the GALWEM data set used in this study, the August 2018 cases were used in this GDI-A study in order to remain consistent with the Donndelinger (2018) GDI-A study. Furthermore, August is one of the most active thunderstorm months in Africa.

57

GDI-A: Relative Humidity (RH)

The mid-level relative humidity at 700 mb was tested first as it showed the most promise in Donndelinger (2018). The GDI-A$_{RH700}$ was calculated by simply adding the 700 mb relative humidity onto the GDI calculation, as noted in Equation 3.5.

$$GDIA_{RH700} = ECI + MWI + II + Co + RH700 \tag{3.5}$$
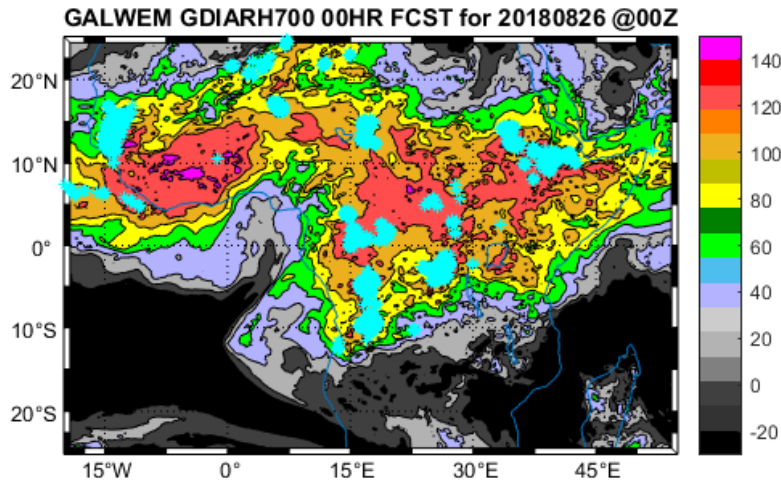
Figure 4.10: GDI-A$_{RH700}$ and lighting plotted over the study region on 26 Aug 2018 at 00Z.

Once the GDI-A$_{RH700}$ was calculated, it was plotted over the study region and the same basic method as described in Chapter III was used to determine location and area error (Figure 4.10). One small change that was needed to the code, as described in Donndelinger (2018), was the alteration of the scattered thunderstorm threshold. The same threshold of 110 (GDI), as used in the previous GDI-A$_{RH700}$ study, was used here to keep consistent methods (Donndelinger 2018). When the initial GDI location error for August was compared against the GDI-A$_{RH700}$, it was determined that the addition of relative humidity at 700 mb to the original GDI, did in fact reduce the location error. However, these results were not significant at the 95 or 90%

confidence levels (Figures 4.11 and 4.12). The use of the higher-resolution GALWEM data did not significantly improve the results from the previous study and it can determined that the addition of 700 mb relative humidity to the GDI alone, was not enough to improve location forecasting at the 95% confidence level.
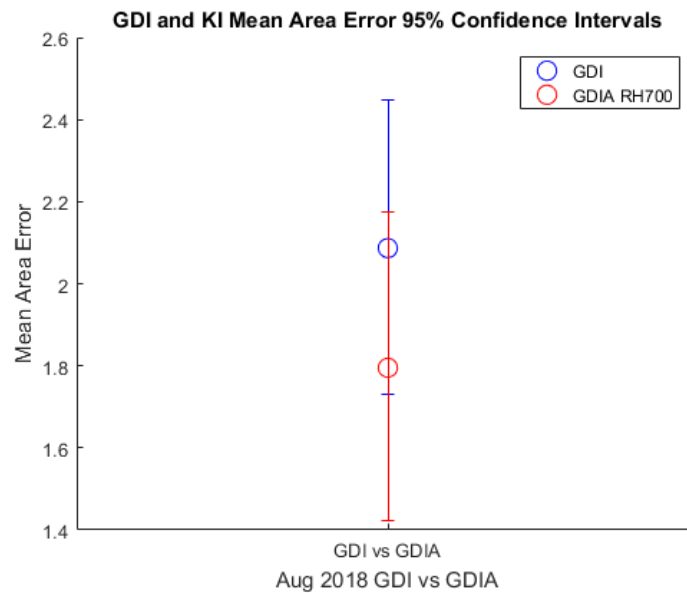
Figure 4.11: 95% confidence interval comparison of GDI (blue) and GDI-A$_{RH700}$ (red) for the August 2018 samples.
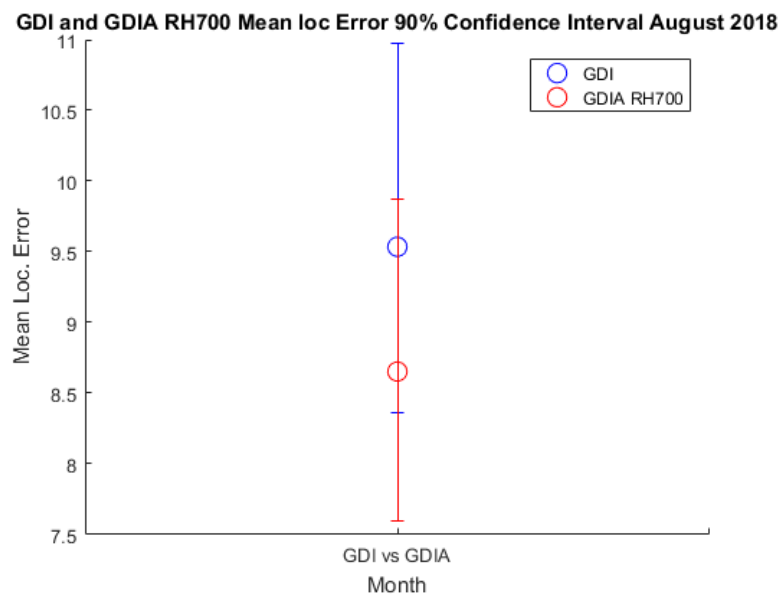
Figure 4.12: 90% confidence interval comparison of GDI (blue) and GDI-A$_{RH700}$ (red) for the August 2018 samples.

GDI-A: Equivalent Potential Temperature Proxies (EPTP)

The next step was to test the equivalent potential temperature proxies (EPTPs). The EPTP modification, as noted in Donndelinger (2018), involves changing only the level at which the highest EPTP was calculated.

$$GDIA_{EPTPXXX} = ECI\ (EPTPXXX) + MWI + II + Co \qquad\qquad (3.6)$$

In Equation 3.6, *XXX* refers to the pressure level (in mb). For these GDI-A$_{EPTP}$ modifications, Donndelinger (2018) altered the level at which the EPTP$_c$ was calculated, changing the level from 500 mb to 900 mb, 850 mb, 800 mb, 700 mb, and 600 mb (Formula 2.4). These levels were chosen based on the concept that the 500 mb dynamics in the higher latitudes of the Caribbean Sea would be captured at lower levels in the lower latitudes of northern Africa (Donndelinger 2018). It was determined that the low-level EPTP modifications worked the best for reducing location error and that the EPTP600 alteration actually increased location error. Of the three low-level EPTP modifications, EPTP900 reduced the location error the most drastically (Donndelinger 2018). Therefore, EPTP900 was selected for analysis in this study to determine if the 17 km GALWEM data could improve the location error further.

Once the GALWEM GDI-A$_{EPTP900}$ was plotted, the GDI-A$_{EPTP900}$ values were further separated into clusters of 55 or greater to indicate scattered thunderstorm potential (Donndelinger 2018) (Figure 4.14). Much like Donndelinger (2018), results of this GALWEM GDI-A$_{EPTP900}$ study indicate that the location error was also reduced for the August 2018 data when compared to the original GALWEM GDI location error values. In fact, the location error reduction was significant even at the 90% confidence level (Figure 4.15). This was a significant improvement to some of the other case studies analyzed in this research and could be an area of further research.
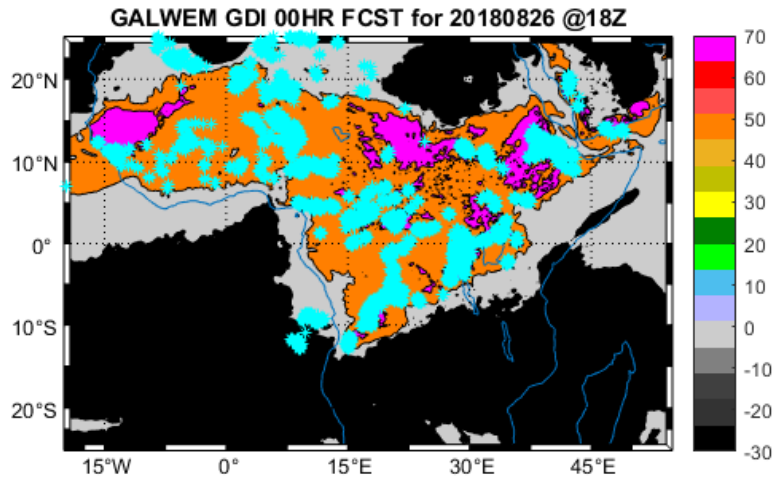
Figure 4.13: GDI-A$_{EPTP900}$ values and detected lightning in cyan asterisks for 26 Aug 2018 at 18Z.
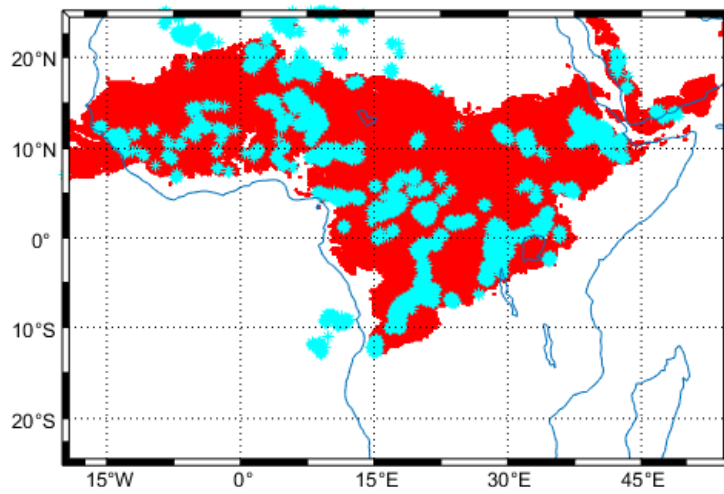
Figure 4.14: GDI-A$_{EPTP900}$ values of 55 and greater in red dots with lightning plotted over top in cyan asterisks for 26 Aug 2018 at 18Z.
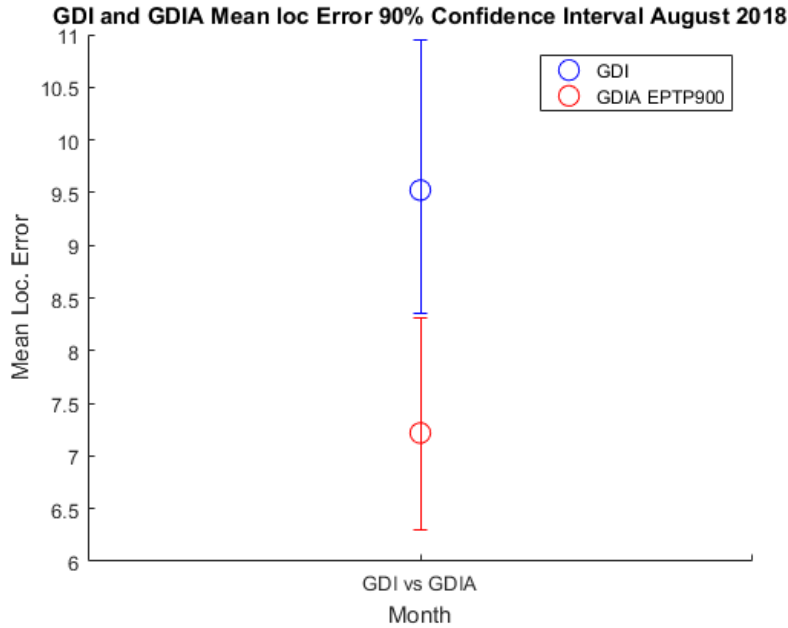
Figure 4.15: 90% Confidence Interval for GDI-A$_{EPTP900}$ (red) compared to the original GDI (blue) for August of 2018.

Elevated Layer A Study

Upon completion of the GDI-A$_{EPTP900}$ case study, it was reasoned that another modification of the GDI could be to raise the level at which Layer A was calculated. The reasoning behind this was that less available low-level moisture over portions of the African continent, especially the interior and near the Sahara, would lead to higher-based thunderstorms. Therefore, the new test height of Layer A was selected as 875 mb instead of 950 mb, as calculated in the original GDI algorithm (Formula 2.5).

The GDI for the Elevated Layer A was calculated using the August days and times once again, and then 60 was chosen as the scattered thunderstorm threshold (Figure 4.17). Once the Elevated Layer A location and area errors were averaged and bootstrapped, it was determined that the location error was reduced overall, but was not significant at the 95 or 90% confidence level (Figures 4.18 and 4.19).
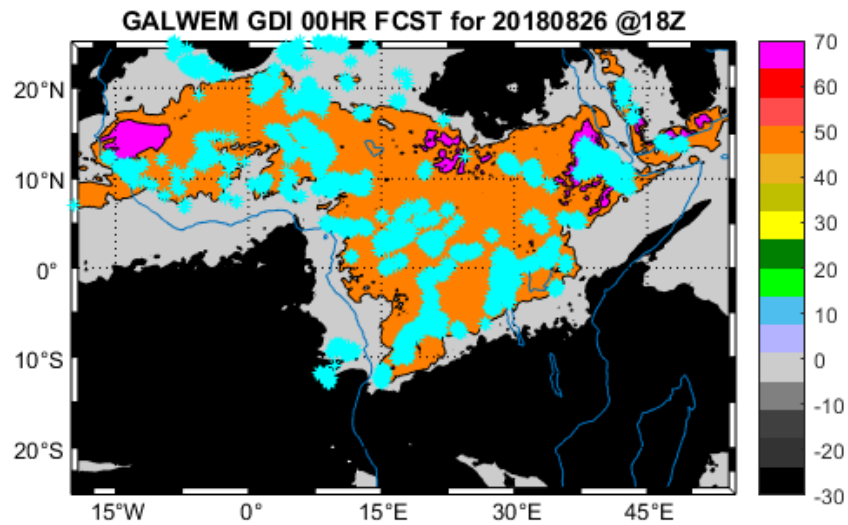
Figure 4.16: GDI values for the Elevated Layer A modification with lightning in cyan asterisks plotted over top for 26 Aug 2018 at 18Z.
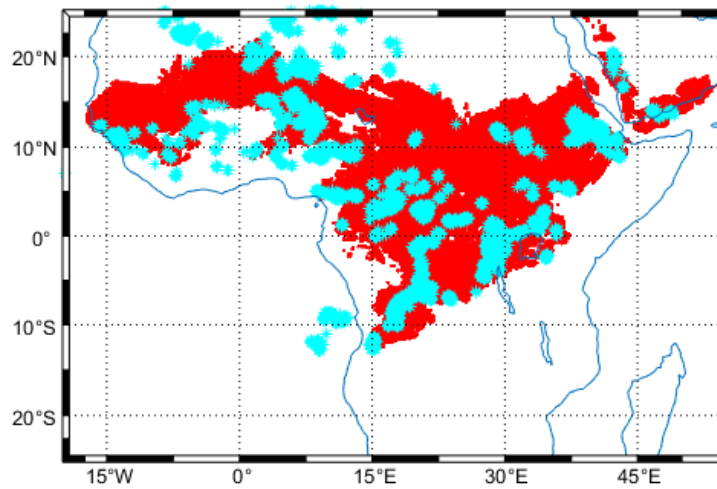
Figure 4.17: GDI-A values of 60 or above for the Layer A modification in red dots with lightning in cyan asterisks plotted over top for 26 Aug 2018 at 18Z.

GDI and GDIA Mean Location Error 95% Confidence Intervals
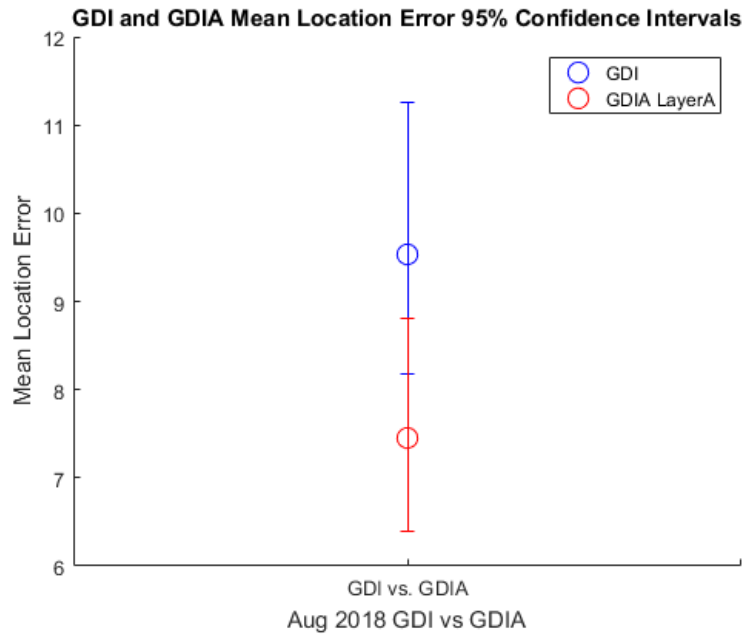
Figure 4.18: 95% location error confidence interval of GDI vs. the GDI-A with Elevated Layer A modification for the August 2018 Elevated Layer A case study.

GDI and GDIA Mean loc Error 90% Confidence Interval August 2018
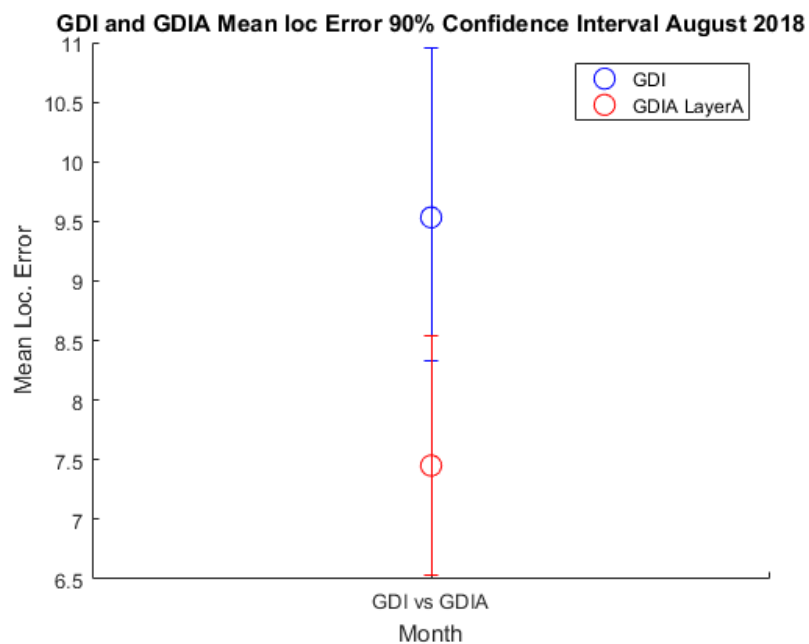
Figure 4.19: 90% location error confidence interval of GDI vs. the GDI-A with Elevated Layer A modification for the August 2018 Elevated Layer A case study.

Although it was not determined with 90% confidence that changing the height at which the potential temperature was calculated for Layer A from 950 mb to 875 mb reduces the location error, it would be a worthwhile extension of this case study to test this concept using multiple height changes, such as 925 mb and 900 mb. It is possible that one of these layer changes could work to further reduce the location error, as hinted at by the lower location error values achieved in this case study.

Another useful alteration to this case study would be to change the scattered thunderstorm threshold. The threshold was set as 60 for this case study, but 55 and 65 would be reasonable choices as well.

Kelvin Wave Study

Kelvin Wave Sign and Regional Study

The final study that was conducted with the GALWEM data was an analysis of Kelvin wave presence and sign over Africa and whether or not these had any effect on the location error of the convective index forecasts. Observed Kelvin wave imagery was obtained from the North Carolina Institute for Climate Studies (NCICS) and accessed at the following link: https://ncics.org/pub/mjo/archive. Coordination with the product creator, Dr. Carl Schreck from the NCICS, confirmed the correct images were being analyzed.

The Kelvin wave sign and regional study looked at the atmospheric conditions during multiple cases in the lowest 5% of GDI location error. The initial goal was to analyze the cases that exemplified location error within one diameter of the widely-used, base lightning watch. A lightning watch generally uses a range ring of 25 nautical miles (nm) and therefore, a diameter would be 50 nm (or about 92.6 km). Near the equator, 1 degree of longitude (or latitude) is

approximately 111 km. This would mean that the "good" location forecasts would need a location error on less than 1 degree. Some of the lowest location errors achieved in this study were around 3 degrees, so this was not a realistic goal. Therefore, the goal was reset to the lowest 5% of cases, which all exhibited less than 4.7 degrees for GDI location error. Of the six lowest location error examples, two dates did not have any Kelvin waves present, so they were excluded. These dates are 26 April and 24 July 2018 (Figures 4.20 and 4.21). The remaining examples were as follows: 10 May 2018 at 06Z, 26 August 2018 at 18Z, 22 September 2018 at 18Z, and 24 September 2018 at 06Z.
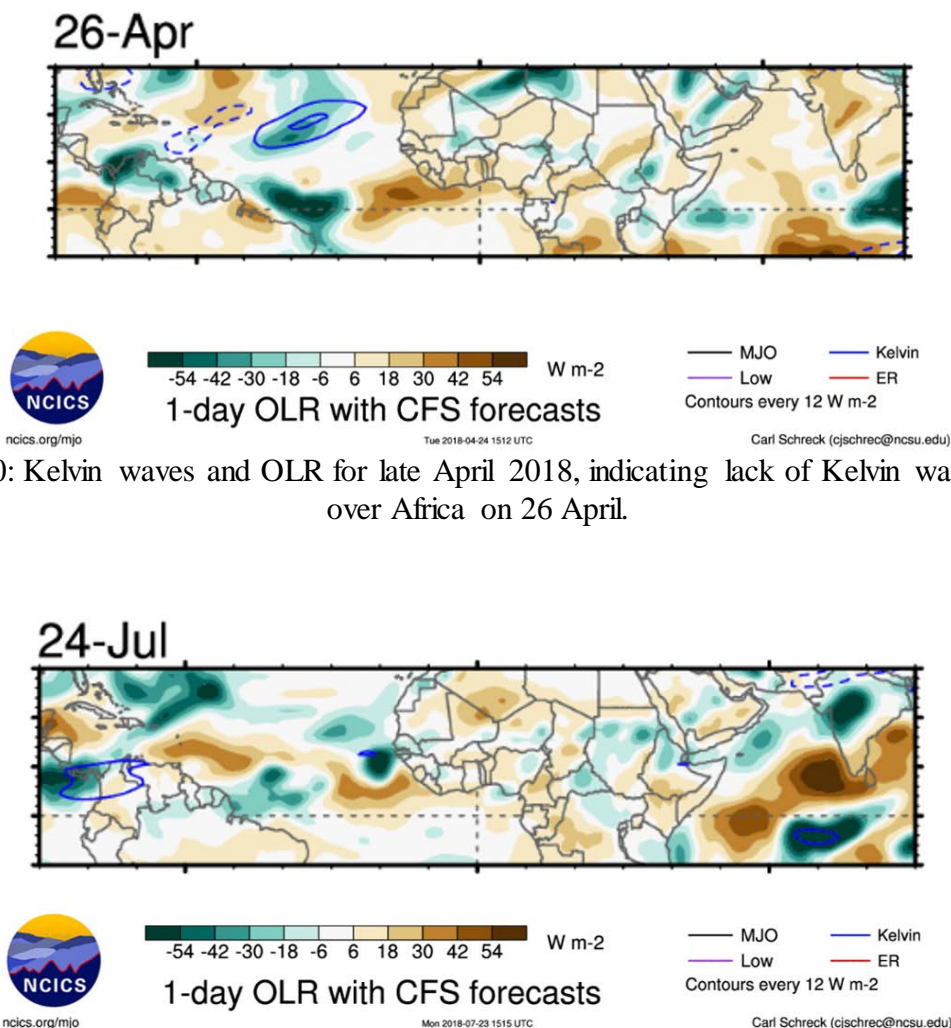
Figure 4.20: Kelvin waves and OLR for late April 2018, indicating lack of Kelvin wave presence over Africa on 26 April.

Figure 4.21: Kelvin waves and OLR for late July 2018 indicating lack of Kelvin wave presence over Africa on 24 July.

Table 4.1 Lowest 5% of GDI location error examples across the full study region with corresponding regional GDI location errors.

Date/Time	Kelvin Wave Present? (Y/N)	Full study region GDI loc. Error (degrees)	West Africa GDI loc. error (degrees)	East Africa GDI loc. error (degrees)
26 Apr 2018/06Z	N	4.20	7.95	3.43
10 May 2018 at 06Z	Y	4.69	4.20	14.32
24 Jul 2018 at 06Z	N	4.24	5.20	8.65
26 Aug 2018 at 18Z	Y	4.23	5.82	2.89
22 Sep 2018 at 18Z	Y	3.57	7.30	8.23
24 Sep 2018 at 06Z	Y	3.03	6.97	11.00

The 1-day Kelvin wave images of observed and Climate Forecast System (CFS) forecasts are analyzed for these examples. The 1-Day Kelvin wave images were not archived each day, so some of the days in the sample set reference the CFS forecasted Kelvin wave location and sign, as the observed are not present. For this study, the observed and CFS-forecasted outgoing longwave radiation (OLR) charts are used. In Kelvin wave and OLR graphics, dashed blue lines are positive Kelvin waves and indicate drying/suppression of convective activity, while solid blue lines are negative Kelvin waves, which indicate wet/convective activity (Schreck 2018).

The 10 May 2018 case is the first example. The 06Z GDI from this day had a calculated location error of 4.20 degrees. Kelvin waves are observed on 10 May off the West African coast, in Northwest Africa, in West Central Africa and off the East African coast (Figure 4.22)

67
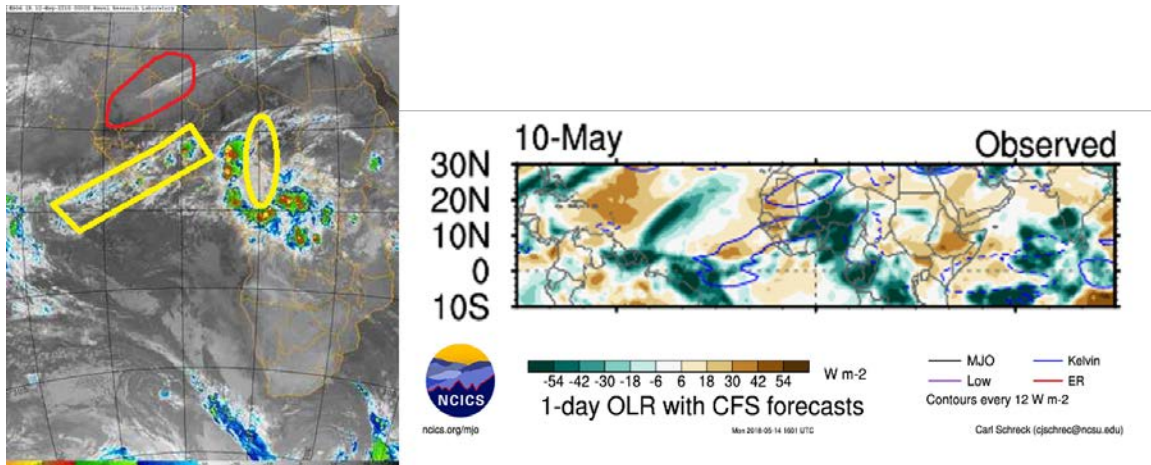
Figure 4.22: Comparison of IR satellite imagery with Kelvin waves outlined in yellow and red (left) and Kelvin waves and OLR (right) for 10 May 2018 over Africa (Schreck 2018).

The Kelvin waves off the West Coast and in Northwest Africa are both negative and therefore point to wet/convective activity. The Kelvin waves in West Central Africa and off the East coast are positive in sign and therefore indicate dry/suppressed weather for that day. Except for the wave off the East Africa coast, which is not covered by this IR image, the IR imagery for this day supports these convective regions fairly well (Figure 4.22).

The yellow rectangle outlined in the satellite imagery, highlights the region of convective activity that correlates with the observed, negative Kelvin wave that stretches from off the west coast of Africa through Guinea and northeastward through Niger and Nigeria. This region lines up well overall with the expected saturated and convective activity that is typically associated with negative Kelvin waves.

The yellow oval outlines a positive Kelvin wave as shown in Figure 4.20, which indicates drying and suppression. This region lines up well with the IR imagery that shows a dry, and mainly cloudless, region east of the MCS near Niger and Chad.

Lastly, the red oval in northwest Africa correlates to the negative Kelvin wave shown in Figure 4.20. This negative Kelvin wave should mean convective activity in this region over

68

Senegal, Mauritania, Mali, etc., but there is little to no convection indicated on the IR satellite. This could be due to the relative lack of moisture in this region.

Analysis of the regional location errors can help draw connections between the positioning of these waves with location error reductions. For 10 May 2018 at 06Z, the West African GDI location error is 4.2064 degrees, while the East African GDI location error is 14.32 degrees. This shows a connection between the expected increase in convective activity associated with the negative Kelvin waves and lower location error in West Africa. Furthermore, positive Kelvin waves present in East Africa indicate drying and suppression associated with the much higher location error in East Africa. The next chronological example among the lowest 5% of location error examples is 26 August 2018 at 18Z.

For 26 August 2018 at 18Z, the GDI location error of the entire study region is 4.23 degrees. During this day, there is a small, positive Kelvin wave observed over Western Africa (Figure 4.23).
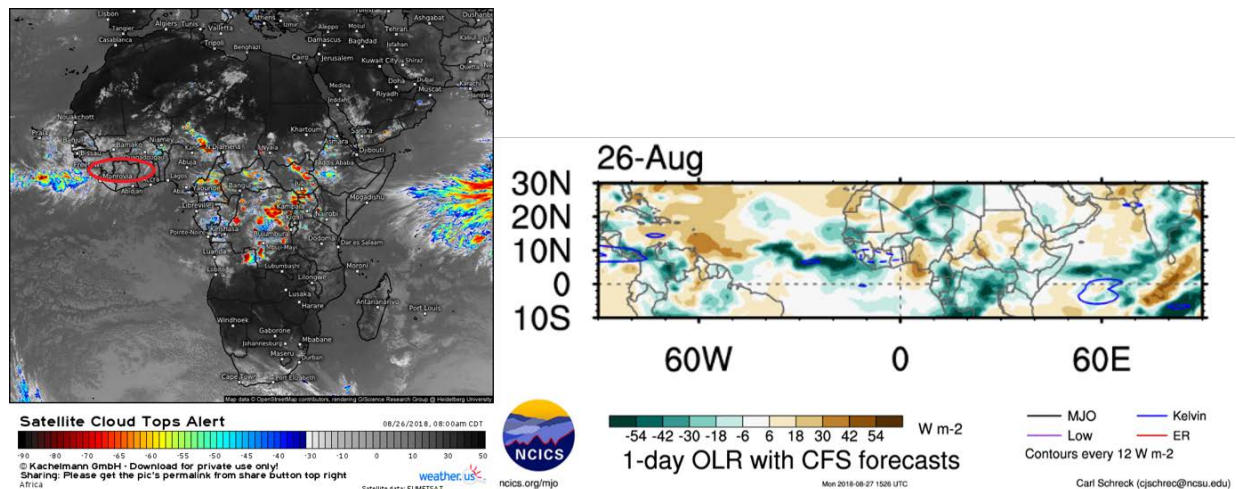
Figure 4.23: Comparison of IR satellite imagery with Kelvin wave outlined in red (left) and Kelvin waves and OLR (right) over Africa for 26 August 2018. The positive Kelvin wave lines up with the relatively cloud-free region outlined in the red oval on the IR imagery (Schreck 2018).

Referencing the regional study, the GDI location error for West Africa on this day and time is 5.82 degrees for West Africa and 2.89 degrees for East Africa. While both of these location errors are fairly low, the difference between the West and the East could very well be a product of the positive Kelvin wave presence in West Africa. This positive Kelvin wave suggests drying and suppression of storms in the West and this is supported by lack of convection in this region (Figure 4.23). This example shows a link between positive Kelvin wave presence and decreased location forecast skill regionally.
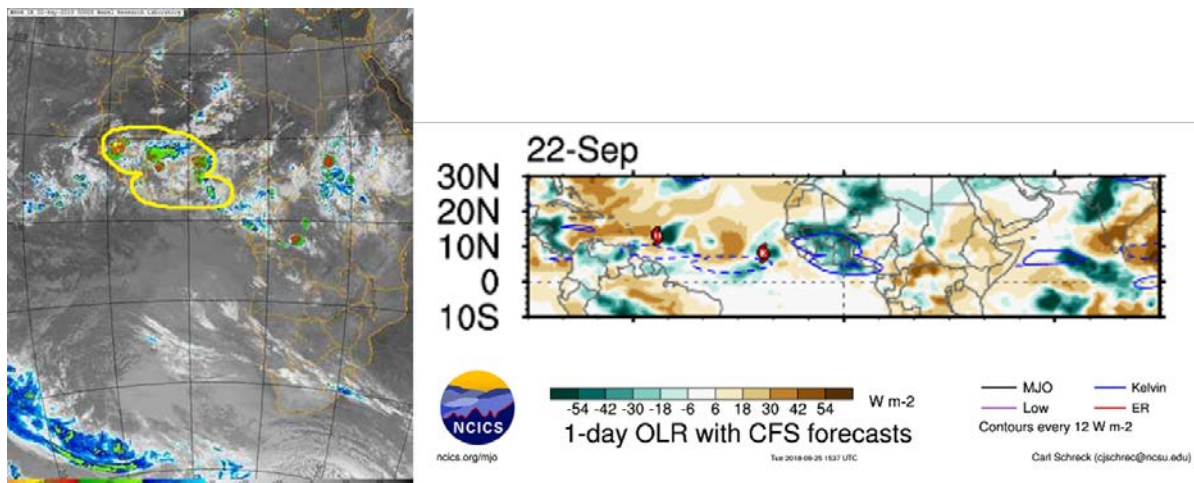
Figure 4.24: Comparison of IR satellite imagery with negative Kelvin wave outlined in yellow (left) and Kelvin waves and OLR (right) over Africa for 22 September 2018. The negative Kelvin wave lines up with convective region in West Africa outline in the yellow oval (Schreck 2018).

The next low location error example to be analyzed is the 22 September 2018 at 18Z timeframe. The GDI location error for this date and time was 3.57 degrees for the entire study region. For 22 September, a negative Kelvin wave is observed over the majority of West Africa (Figure 4.24). This negative Kelvin wave suggests wet and convective conditions. The IR satellite imagery supports the convective activity for this day along the West African coastline (Figure 4.24).

Analyzing the results of the regional study, it is noted that the West Africa GDI location error is 7.30 degrees, whereas the East Africa GDI location error is 8.23 degrees. Although it is not a significant difference, this example still shows connection between negative Kelvin waves and decreased location error (increased location forecast skill).

The last example among the lowest 5% of location error is 24 September 2018 at 06Z. The GDI location error for this day and time was 3.03 degrees for the whole study region. There were two small Kelvin waves observed during this day. The first wave was a positive Kelvin wave over far Western Africa. The other wave is a very small, negative wave over Central Africa (Figure 4.25). These two waves would suggest a drying and suppression of storms in the far western portions of the continent along the coastline and increased convective activity in the direct central interior of Africa. The IR imagery tends to line up well with the implied suppression and bolstering of convection associated with these two narrow waves (Figure 4.25).
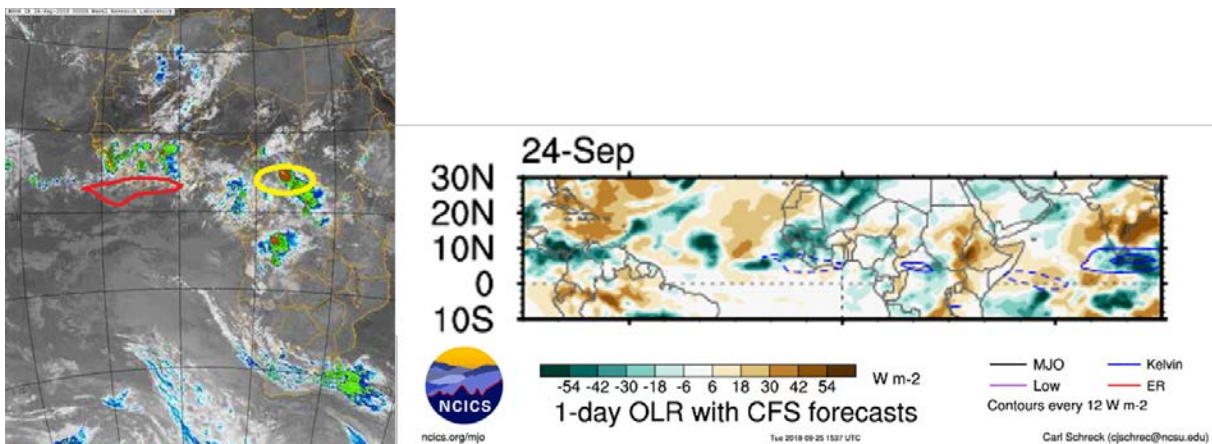
Figure 4.25: Comparison of IR satellite imagery with Kelvin waves outlined in yellow and red (left) and Kelvin waves and OLR (right) over Africa for 24 September 2018. The red outline shows a positive Kelvin wave that lines up with an area of little-to-no convective activity while the yellow oval outlines a negative Kelvin wave coinciding with an MCS (Schreck 2018).

Reviewing the regional study, the West Africa GDI location error is actually higher than the East Africa GDI location error in this case. The West and East GDI location errors are 6.97 and 11.00 degrees, respectively. This is the first example among the lowest location error

examples in which the regional location error does not line up well with the presence and type of Kelvin wave.

The convective regime study showed that the GDI location error exhibited the highest error when the predominant convection source was due to MCSs. Convective activity on this day was primarily MCS-based with multiple MCSs in Central/West Africa. However, this should suggest that the GDI location error would be higher in the west than the east due to the presence of MCSs and a positive Kelvin wave, but the opposite is true. Therefore, there must additional factors affecting the location error for this example. These Kelvin waves are fairly limited in terms of areal coverage. This could mean that the Kelvin waves did not play much of a role in altering convection overall for this day. Therefore, one should consider other factors such as current cloud coverage and dynamic forcing.

Although only a small handful of examples were analyzed in this Kelvin wave study, there seems to be a connection between the presence/type of Kelvin wave and the regional location forecast accuracy: negative (positive) Kelvin wave seems to correspond to a lower (higher) location error. While no statistically significant conclusions can be drawn from such a small sample size, this would be a good extension of the current research. Furthermore, it would be important to look more closely at examples in which the regional GDI location error differed greatly between West and East Africa when Kelvin waves are present somewhere over the continent, especially if waves are located in both regions.

OLR and Kelvin Wave Study

In this study, another connection can be made between the OLR and Kelvin wave sign. As previously discussed, negative (solid blue lines) Kelvin waves suggest wet and convective

activity while positive (dashed blue lines) imply drying and suppression of convective activity. Similarly, negative OLR indicates strong cloud cover and wet/convective areas with positive OLR indicating plenty of outgoing radiation and a lack of convective activity. Therefore, if the sign of the Kelvin wave and sign of the OLR region are the same, this should enhance the signal (i.e. negative Kelvin wave presence over a negative OLR region should indicate significant convective potential). When the sign of the Kelvin wave and OLR do not match, this leads creates some uncertainty in the type and intensity of the convection. This left four cases to be examined: 1) negative Kelvin wave and negative OLR (22 Sep 2018), 2) negative Kelvin wave and positive OLR (10 May 2018), 3) positive Kelvin wave and negative OLR (22 Jun 2018), 4) positive Kelvin wave and positive OLR (22 Jun 2018).

The aforementioned 22 September 2018 case is an example of negative Kelvin wave presence overlying a negative OLR region (Figure 4.24). This day was classified an MCS-day in the convective regime study, showing correlation between the matching sign of the Kelvin wave and OLR with resulting enhanced convective activity (Figure 4.24). The next case to be investigated was a negative Kelvin wave over a region of positive OLR.

The 10 May 2018 case is an example of a negative Kelvin wave over a positive OLR region. The core of the negative Kelvin wave that is shown over the West African coast, coincides with an area of positive OLR (Figure 4.22). Positive OLR suggests a lack of cloud cover and moisture. Therefore, strong positive OLR suggests almost no cloud cover, while weak positive OLR suggests limited cloud coverage. The West Africa coast is under a weak-to-moderate, positive OLR region. Combining the attributes of the wet, convective negative Kelvin wave with the limited cloud coverage suggested by the weak to moderate OLR region, slight potential still exists for convective activity. This was the case along the West Africa coast, as

airmass thunderstorms were the primary source of convection in this region (Figure 4.22). The next case to examine is that of a positive Kelvin wave in a region of negative OLR.

The 22nd of June 2018 is an example of a positive Kelvin wave over a region of negative OLR. On 22 June, a broad, positive Kelvin wave was forecasted over Central Africa with moderate to strong, negative OLR present over the country of Niger (Figure 4.26).
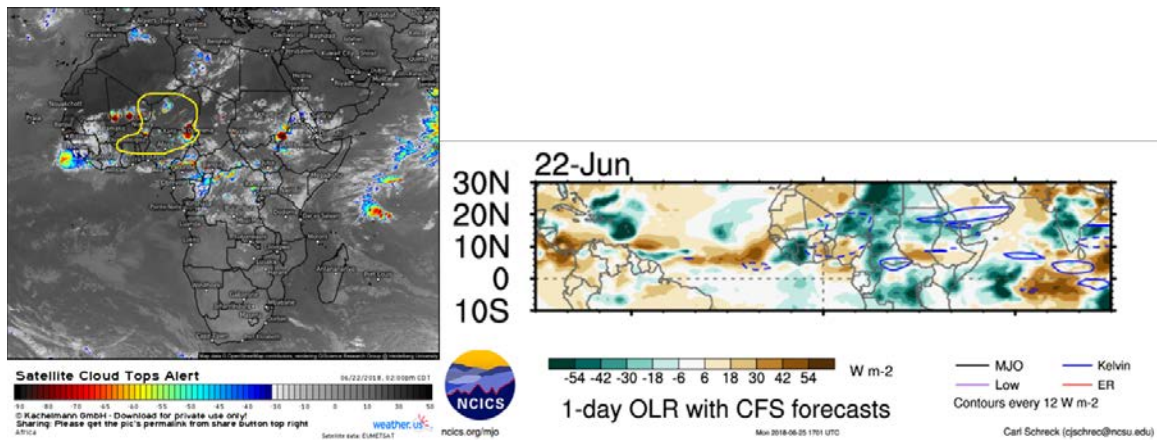
Figure 4.26: Comparison of IR satellite imagery with positive Kelvin wave outlined in yellow (left) and Kelvin waves and OLR (right) over Africa for 22 June 2018 (Schreck 2018).

Negative OLR suggests cloud coverage, while positive Kelvin waves suggest drying and suppression. Similarly to the last case, this situation allows for the possibility of limited convection. Overall, convection was fairly limited over Niger with the primary source of convection being airmass thunderstorms. However, an MCS setup in the afternoon in northeast Nigeria (Figure 4.26). This once again shows that there is a correlation between the sign and strength of OLR and the sign and position of the Kelvin wave, as the strongest region of negative OLR only exhibited airmass storms. However, the presence of the MCS near northeast Nigeria suggests that OLR is the dominant of the two contributing factors when it comes to convective initiation.

22 June 2018 also serves as a good example of the last case in which a positive Kelvin wave exists in a region of positive of OLR. Weak-to-moderate, positive OLR is present for this

day across most of Nigeria and throughout Benin, Togo, and Ghana (Figure 4.26). As positive OLR would suggest, cloud cover is very limited in these regions at 18Z (Figure 4.26). Furthermore, there is little-to-no convection present at this time, supporting the correlation between regions of positive OLR and Kelvin waves and a lack of convective activity. These results are summarized in Tables 4.2 and 4.3 below.

Table 4.2: The four cases and corresponding dates when these conditions occurred.

		OLR	
		Negative OLR (strong cloud cover)	Positive OLR (weak cloud cover)
Kelvin waves (KW)	Negative KW (wet/convective)	22 Sep 2018	10 May 2018
	Positive KW (dry/suppressed)	22 Jun 2018	22 Jun 2018

Table 4.3: The resulting convection type for each case and date as listed in Table 4.2.

		OLR	
		Negative OLR (strong cloud cover)	Positive OLR (weak cloud cover)
Kelvin waves (KW)	Negative KW (wet/convective)	MCS	Weak airmass
	Positive KW (dry/suppressed)	Airmass	Little to no convection

V. Conclusions and Recommendations

Chapter Overview

The purpose of this chapter is to state the conclusions of this research as well as to recommend additional research in order to improve convective forecasting in Africa, especially for storm location. The conclusions are drawn from the results and analysis detailed in Chapter IV.

Conclusions of Research

The main goal of this research was to determine whether or not the Global Air and Land Weather Exploitation Model (GALWEM) is able to improve upon convective forecasting in Africa when compared to the Global Forecasting System (GFS) through the use of two convective indices called the Gálvez-Davison Index (GDI) and the K Index (KI). The study followed similar methodology procedures to Donndelinger (2018) in order to compare his findings using the coarser, GFS 1° horizontal resolution reanalysis data against the results of the 17 km 00 HR GALWEM data. To do so, base parameters of the GALWEM had to be plotted against GFS analysis data in order to assure the GALWEM had no significant model biases. Next, the observed (lightning) and forecasted (index) clusters were split into an objectively chosen number of clusters by use of k-means clustering. Lastly, the observed and forecasted clusters were paired subjectively by the user based on geographic location and two types of error were calculated: 1) location error was calculated to measure the distance between cluster centers of observed and forecasted convection, and 2) area error was calculated to measure the difference in spatial coverage between observed and forecasted convection. Overall, the GDI and

KI consistently had similar location error values, much like Donndelinger (2018). Also similar to the previous study, GDI showed significantly lower area error than KI when using the GALWEM. One main difference between this study and Donndelinger (2018) is that GDI significantly outperformed KI in terms of areal coverage for every case study, whereas Donndelinger (2018) found that the indices performed similarly when the convection was mostly airmass thunderstorms in the intra-seasonal study. Furthermore, this study included a look into regional performance of the indices, as well as a brief analysis of Kelvin wave presence and its effect on the location forecast.

Monthly Study Conclusions

The months of April through September were used for this study. The following dates were selected for use in this study: 10th, 12th, 14th, 22nd, 24th, and 26th. Each day included a sample from 00Z, 06Z, 12Z, and 18Z. All of these samples were used due to the small sample size of each month. Prior to full statistical analysis, the GDI and KI location and area errors were calculated and averaged across all times by month. The results show that the highest and lowest location errors for GDI are found to be in the months of May and July, respectively. The highest area error for GDI was found to be in the month of August, whereas the lowest area error for this index was found in the month of May. Similar to the GDI, the highest location error for the KI was across the May samples. However, the lowest location error for KI was found in the month of August. Lastly, the highest and lowest monthly area error for KI was determined to be in the months of April and July, respectively.

After bootstrapping to ensure robust confidence intervals for each month's data set, the results indicate the GDI and KI mean location error are relatively close in value in the Spring and early Summer months (April, May, June) but begin to show some separation in the mid-to-late

Summer months (July and August) into the early Fall (September). These results indicate a departure from Donndelinger (2018), in which the two indices showed furthest separation in terms of location error in the month of May. In this study, the mean location errors between the two indices are actually the most similar out of all the months at the 95% confidence level. However, indices' error bars overlap for each month at the 95% confidence level, indicating that it cannot be said with high confidence (95%) that one index outperforms the other.

Both indices' mean location error showed an overall decreasing trend between May and July, similar to Donndelinger (2018) study. The greatest difference between the GDI and KI location error is in the month of August. However, the error bars for each index still overlap at the 90% confidence level, indicating that it can still not be said with 90% confidence that one index performs better than the other in the month of August.

Zulu Time Study Conclusions

Location and area error were analyzed for each date according to Zulu time in order to provide at least a 48-hour separation between samples. This was done in an attempt to create data sets with independent weather patterns from one sample to the next.

Results show that the highest and lowest location errors for GDI were determined to be 12Z and 18Z, respectively. The highest and lowest area error for GDI was determined to be 00Z and 18Z, respectively. This suggests that the GDI performs best for afternoon thunderstorm forecasting. Typically, during the months of April through September, the study region experiences greater frequency of diurnal, airmass thunderstorms during the afternoons. This would suggest that the GDI performs best for airmass thunderstorms. This will be discussed in the next section.

For KI, the highest mean location and area errors were noted in the 06Z sample, and the lowest location and area errors occurred in the 18Z samples. Much like the GDI, the KI performed best in the afternoon hours. This suggests that the KI generally works best for afternoon thunderstorm forecasting. This will be discussed in the next section as well.

Convective Regime Conclusions

In the convective regime study, samples were divided amongst four convective regimes: purely airmass thunderstorms (AT), purely MCS convection (MCS), primarily airmass convection with MCS(s) present (AT/MCS), and primarily MCS convection with airmass storms present (MCS/AT). The location and area errors were calculated across all days and times and their results bootstrapped to 10,000 samples.

The GDI performed best when the primary convection type was airmass thunderstorms. This is the opposite result of what Donndelinger (2018) found, suggesting that the higher-resolution GALWEM, did in fact, resolve smaller features well and provides a better handle on airmass storms than the GFS reanalysis 1° horizontal resolution data.

The KI did not show as consistent of a trend as the GDI. The lowest location error for the KI was a tie between the MCS and AT/MCS cases, although as previously stated in Section IV, the KI location errors were all within .092 degrees of one another. This shows that the KI performs with nearly the same accuracy when determining cluster location no matter the convective regime present. The lowest area error for KI was noted in the AT regime. Therefore, it can be concluded that the KI performs best overall when the primary convection type is airmass storms.

In this study, GDI once again significantly outperformed KI at the 95% confidence level in terms of area error. In fact, most regimes show more than twice as high an area error for KI

compared to GDI. Therefore, GDI can confidently be used over the KI to forecast area thunderstorm coverage.

Regional Study Conclusions

For this study, the entire study region was split into west and east at the 25°E longitude line. New lightning data were requested and location and area error were calculated and averaged across all days and times. Results indicate that the location error was overall lower in West Africa than East Africa. The KI outperformed the GDI in West Africa and the opposite was true in East Africa. However, neither of these results can be concluded with 95% confidence for either region.

The area error was similar between the west and east for like indices with the GDI having significantly lower error than the KI. Unlike the location error, these results are significant at the 95% confidence level.

These results contradict the findings of Gálvez and Davison (2016), which state the GDI generally works best for open ocean areas and the eastern fringes of continents. This could be due to the relatively small data set, the inclusion of Southwest Asia in the study region, the relatively poor forecast skill of both indices in southern Africa, or a combination of more than one of these elements.

Model Comparison Study Conclusions

In the model comparison study, the like months in this data set and Donndelinger (2018) were compared to determine if the higher-resolution GALWEM data could improve the forecast, especially in terms of the location error, when compared to the GFS reanalysis 1° horizontal resolution model data. While these dates are not the exact same because GALWEM data could

only be pulled from 10 days prior, the results indicate the GALWEM actually has higher location error in almost all cases.

For the GDI, the 2018 (GALWEM) samples all exhibit higher mean location error than the 2016 (GFS) GDI samples in corresponding months. For KI, the 2018 (GALWEM) samples show higher mean location error than the 2016 (GFS) samples in two out of three months, with August being the only example for which the mean location error was lower in 2018 than in 2016. The GDI area error shows more positive results, however.

The GDI mean area error for the 2018 months was consistently lower than the 2016 months for each matching month. This suggests that the higher resolution GALWEM data is, once again, able to more accurately portray the areal coverage of convection over Africa when compared to the low resolution GFS. The ability of the 17 km GALWEM data to reduce the area error continues to be one of the most significant findings of this study. For KI, the opposite results were found with the area error actually being higher in the 2018 months than their corresponding 2016 months.

Although these results are subjective due to lack of matching days and a slightly different study region, it is promising that the GDI continued to show lower area error than the GFS.

GDI-A Study Conclusions

Based on the results of several modifications and additions Donndelinger (2018) made to the GDI, the most promising African GDI alterations (GDI-As) from his study were tested with GALWEM data to determine if the higher resolution model could reduce location error further. The two GDI-As tested were the GDI-A_{RH700} and the GDI-$A_{EPTP900}$. Furthermore, this study analyzed an alteration to the Layer A height (Formula 2.5).

The GDI-A$_{RH700}$ proved to lower location error when compared to the original GDI. However, the reduced error was not significant at the 95 or 90% confidence level. The use of the higher resolution GALWEM data did not significantly improve upon the results of the previous study and it can be said with confidence that the addition of 700 mb relative humidity to the GDI is not enough to greatly improve the location forecast accuracy.

Similar to the GDI-A$_{RH700}$ and Donndelinger (2018), the GDI-A$_{EPTP900}$ showed a reduction in the location error when compared to the original GDI. However, these results are significant at the 90% confidence level. This is the only test in this entire study that showed a significant decrease in location error and should be a focus of further research.

Lastly, the GDI-A study analyzed the lowest potential temperature layer. In this study, the Layer A height was modified from 950 mb to 875 mb. This was done in an effort to capture more high-based thunderstorms, especially in arid regions near the Sahara and interior continental areas. Results showed that the Elevated Layer A test reduced the location error when compared to the original GDI, but these results were not significant at the 95 or 90% confidence levels. This test could be expanded by further modifying the Layer A base height to 900 mb and 925 mb and changing the scattered thunderstorm threshold from 60 to 55 and/or 60. This would allow for several more tests.

Kelvin Wave Study Conclusions

Lastly, a brief Kelvin wave study was completed. The first portion of this study analyzed sign and presence of Kelvin waves to determine if these had any correlation to location error, using the regional study results as support. Part two of this study looked at both Kelvin wave and OLR sign to determine the type of convection present. For both portions of the Kelvin wave study, images were obtained from the North Carolina Institute for Climate Studies (NCICS) and

show outgoing longwave radiation (OLR) and 1-day observed or Climate System Forecast (CFS) Kelvin waves.

Part one of this study analyzed the six cases within the top 5% of lowest location error. The following dates and times were examined: 26 April 2018 at 06Z, 10 May 2018 at 06Z, 24 July 2018 at 06Z, 26 August 2018 at 18Z, 22 September 2018 at 18Z, and 24 September 2018 at 06Z. IR satellite imagery was also compared against the Kelvin wave images to determine whether or not the sign of the Kelvin wave lined up with an active (negative wave) or suppressed (positive wave) convective region. Both the 26th of April and 24th of July had no observed Kelvin Waves present and were therefore discarded from this study. Therefore, the first sample to be analyzed was the 10th of May 2018 at 06Z.

For 10 May at 06Z, the GDI location error was 4.20 degrees for the whole study region. Kelvin waves were observed off the West African Coast, Northwest Africa, West Central Africa, and off the East African coast. Except for the Kelvin wave over Northwest Africa, the sign and position of each wave lines up well with position and presence of, or lack thereof, convective activity. The negative wave over Northwest Africa should imply a wet and convective region but there is little to no convective activity. This could be due to the lack of moisture in the Sahara, among other factors. When analyzing the regional study, the West and East African GDI location error are 4.2064 and 14.32 degrees, respectively. Regional location errors show the correlation between negative waves over West Africa and lower location error. On the other hand, correlation can also be shown between the positive waves over Central and East Africa, indicating suppression of convective activity, and higher location error. The next case is the 26th of August 2018 18Z.

The GDI location error for 26 August at 18Z is 4.23 degrees for the entire study region. During this day, a small, positive Kelvin wave was observed over the West African coastline. A fairly dry and cloudless region is shown on IR imagery over the same region during this day, which is in line with the expected drying and suppression associated with the presence of a positive Kelvin wave here. Analysis of the regional study location errors for GDI show values of 5.82 and 2.89 degrees in West and East Africa, respectively. While these location errors are both quite low, the presence of the small, positive Kelvin wave in West Africa once again shows a correlation between positive waves decreasing forecast skill (i.e. higher location error). The next sample analyzed is the 22nd of September 2018 at 18Z.

For 22 September at 18Z, the GDI location error is 3.57 degrees for the whole study region. For this day, a broad, negative Kelvin wave is present over most of the West African coast. This negative Kelvin wave suggests wet conditions and convective activity, which is in fact the case when the IR imagery is reviewed. When the regional GDI location error is analyzed, it is determined that the West Africa location error is 7.23 degrees, while the East Africa location error for GDI is 8.23 degrees. Like the last example, this case does not show as significant a difference between the location error of the west and east as does the 10 May case, but still shows a correlation between negative Kelvin wave presence and lower location error regionally. The last case to be analyzed is the 24th of September at 06Z.

The GDI location error for 24 September at 06Z across the entire study region is 3.03 degrees. Two Kelvin waves are observed during this day: a narrow, positive wave just south of the West African coast and small, negative wave over central Africa. Both areas line up with the weather pattern implied by the sign of the Kelvin wave over their particular region when the IR satellite imagery is analyzed.

A review of the regional GDI location error for this day and time reveals errors of 6.97 and 11.00 degrees for West and East Africa, respectively. The initial conclusion is that this case does not fall in line with the previous examples. However, further analysis shows that the small, negative Kelvin wave over Central Africa straddles the west/east dividing line implemented in the regional study with the majority of this wave actually in the West African study region. This suggests that the Central African Kelvin wave should have more effect on West Africa than East Africa. This would mean a positive and negative Kelvin wave over West Africa and only a small portion of the negative wave present over East Africa. This should indicate fairly neutral conditions in the west and a slightly decreased location error in the west. While this seems to be the case in West Africa, as 6.97 degrees is a fairly moderate location error, the East Africa GDI location error is fairly high. Therefore, it seems that there is more to this case than the others. To determine a root cause for the location error difference, the convective regime for this day and time was reviewed. This particular example was classified by the author as an MCS/AT sample. The MCS/AT regime exhibited the second highest location error among the four convective regimes. As the majority of MCSs form over East and Central Africa, this could be one of the main reasons the East African GDI location error is higher than that of West Africa.

Not only does there appear to be a correlation between the sign of Kelvin waves and the location error, but there also appears to be correlation between the sign of the OLR and Kelvin wave with the type and amount of convective activity. This was shown by analyzing four cases: 1) negative Kelvin wave and negative OLR, 2) negative Kelvin wave and positive OLR, 3) positive Kelvin wave and negative OLR, 4) positive Kelvin wave and positive OLR. The 22 September case showed a negative Kelvin wave that coincided with a region of strong, negative OLR. The maximum convective potential indicated by the presence of both strong, negative

OLR and negative Kelvin waves correlated well with satellite imagery, which showed MCSs over West Africa.

For case 2, negative Kelvin waves and positive OLR, 10 May 2018 was the sample analyzed. On this day, weak, positive OLR and a negative Kelvin wave overlapped off the West Africa coast and along the far West African countries. Although OLR was positive, storm activity was still possible due to the negative Kelvin wave presence. During this day, satellite imagery showed airmass storms in this region. This indicates that, although positive OLR was present, storm initiation is still possible since the OLR was weak. Therefore, OLR strength is of importance.

The 22nd of June was an example of both cases 3 and 4, as there was a broad, positive Kelvin wave over Central Africa encompassing a region of both negative and positive OLR. Strong, negative OLR was present over Niger and northeast Nigeria at this time. In the region of strongest, negative OLR, only airmass storms are present. However, in northeast Nigeria, an MCS formed. This case shows that although positive Kelvin waves can stifle convection somewhat, OLR seems to be the more significant factor for convective support. For the same day, positive OLR is present over majority of Nigeria, Benin, Togo, and Ghana. Satellite indicates little to no cloud cover or convection for this region, showing correlation between positive OLR and Kelvin waves and minimal convection possibility.

While this case study is a very narrow one, results show an overall consistent correlation between Kelvin wave presence/sign and location error. However, as indicated by the last sample analyzed here, more factors such as the convective regime for the day and time in question, should be analyzed in order to determine which other features affect the location forecast accuracy.

Recommendations for Action

Overall, this study concluded that the GDI did not significantly improve the location forecast accuracy when compared to the KI for convection over Africa. However, the GDI showed significant improvement over the KI in terms of areal convective coverage with 95% confidence. Therefore, it is recommended that forecasters use the GDI over the KI to forecast African convection, as it boasts a more accurate areal coverage forecast with very little difference in location error.

When like months from Donndelinger (2018) and this study were compared, results show that the GDI location forecast accuracy did not improve using the 17 km GALWEM data. However, the results once again showed a decrease in the area coverage between like months when using the GFS and GDI. Overall, the GDI improved upon the areal coverage forecast when compared across months, times, convective regimes, and regions. Significant confidence should be placed in GDI's areal forecast coverage.

The GDI proved to perform best when the predominate convective pattern was airmass thunderstorm-based, and worst when the predominate convection was due to MCSs. The opposite was the case in Donndelinger (2018). This could very well be a product of the increased model resolution used in this study that aided resolution of smaller terrain, weather, and other features.

Alterations to the GDI proved to consistently lower location error. The addition of 700 mb relative humidity did not lower location error at the 95 or 90% confidence level. Raising the height at which the Layer A Potential Temperature was calculated also proved to lower location error, but was also not significant at the 95 or 90% confidence level. Lastly, the alteration of the height at which Layer C was calculated in the equivalent potential temperature proxy (EPTP)

87

study proved to lower location error as well. While the decrease in location error when compared to the original GDI was not significant at the 95% confidence level, it was significant at the 90% confidence level. This was the only study in which the location error decrease was significant at the 90% confidence level. For this reason, it is recommended that the EPTP 900 mb (GDI-$A_{EPTP900}$) modification be considered as a change to the GDI for African convection forecasting.

To determine convective potential, it is recommended that forecasters examine OLR and Kelvin wave charts. Use of these charts can help determine the type and intensity of convection when matching the sign of the OLR with the Kelvin Waves. This can help forecasters subjectively narrow down areas of convection and aid decision-making guides.

Future Research Recommendations

First and foremost, future research would ideally include a data set that spans at least multiple years. While this was not a possibility due to the archive capabilities of the 16th Weather Squadron, this would provide a much more robust study period and allow more significant trends to present themselves.

Another future research idea would be to repeat methods in this and Donndelinger (2018) with even higher GALWEM data resolution in order to determine if a higher resolution data set could aid in location forecast accuracy. This study indicated little to no improvement in terms of location forecast accuracy between the GALWEM and GFS, despite the much higher resolution 17 km GALWEM data used in this study.

The regional study showed a lower location error overall in West Africa compared to East Africa. One aspect that could be investigated further would be to pinpoint the regions in Africa where the GDI achieves the highest forecast skill to aid forecasting ability at the local

level. This could in turn aid lightning forecasts from base to base and ideally lower false alarm rates for lightning watches, giving base operations leaders more planning time.

The EPTP900 modification to the GDI proved to lower location error and was significant at the 90% confidence level. This was the only test in which the location error reduction was significant at least at the 90% confidence level. Therefore, the EPTP900 alteration should be investigated further. Ideally, a larger span of dates and times should be used to provide a more robust data set. This could be further investigated to determine if this change to the GDI works best for certain seasons, regionally, or under one convective regime than another.

The Elevated Layer A study is another recommended expansion of the current research. While results showed that changing the height of Layer A from 950 mb to 875 mb did not reduce the location error at the 95 or 90% confidence level, other levels including 925 and 900 mb should be tested to determine if these could be the ideal height for this layer.

Lastly, although a very brief case study, the Kelvin wave study performed in this research showed a correlation between Kelvin wave presence and sign and the location error of the GDI regionally. Furthermore, investigation of OLR and Kelvin wave sign showed correlation between these two factors and the type and intensity of convection. This suggests that Kelvin waves could help forecasters determine whether more or less convection should be expected in Kelvin wave regions in the coming days and Kelvin wave charts could serve as an additional tool, alongside the GDI and dynamical tools, when drawing thunderstorms charts over the continent. The case study should be expanded to include more dates and times in order to determine if the correlation stands true given a bigger sample size.

Summary

Overall, the GDI is applicable to forecasting convection over the African continent. The GDI consistently outperforms the KI in terms of areal convection coverage, with little difference in the location forecast. Forecasters can place confidence in the GDI when predicting convection over Africa. When used along with other forecasting tools such as satellite imagery, the GDI can help forecasters to create an accurate picture of the current weather patterns and the expected progression, furthering improving our understanding of the climate system. Although there is much more to be done, the GDI has once again proved to increase forecast accuracy and can therefore aid strategic, operational land and air movements. Although modifications to the index, such as the EPTP900, have shown promise, further research should be completed to tailor the GDI specifically to the African continent to provide the best forecasting tool for our weather personnel in order to support the customer.

Overall, results indicate the following:

1.) The GDI should be used instead of the KI as the GDI decreases area error for convection at the 95% confidence level when compared to KI with little change to the location forecast accuracy.

2.) OLR and Kelvin wave imagery should be analyzed and used in conjunction with the GDI to aid thunderstorm forecasting over the African continent.

    a. OLR should be prioritized over Kelvin wave sign when both OLR and Kelvin wave sign are being considered.

Appendix A: Monthly Study Error Values

Table A1: GDI and KI location and area errors for April 2018.

	GDI Location Error	GDI Area Error	KI Location Error	KI Area Error
22-Apr				
00Z	11.0585	-2.3586	10.1777	-6.2594
06Z	10.1457	-0.1676	8.6034	-3.6068
12Z	16.1837	-2.7599	22.0443	-6.3218
18Z	8.9697	-1.7264	5.2807	-4.1465
	GDI Location Error	GDI Area Error	KI Location Error	KI Area Error
24-Apr				
00Z	7.7640	-2.0483	12.2039	-4.8023
06Z	13.4614	-0.6717	16.7154	-4.2185
12Z	12.6368	-1.0855	12.4409	-5.0577
18Z	9.7394	-1.3633	6.2243	-4.2531
	GDI Location Error	GDI Area Error	KI Location Error	KI Area Error
26-Apr				
00Z	6.2744	-3.8422	7.0391	-6.2202
06Z	3.9952	-3.2322	6.2069	-5.8842
12Z	5.6584	-1.1595	6.1660	-4.3140
18Z	6.1260	-0.6050	6.8091	-3.4221
Monthly Avg.	9.3344	-1.7517	9.9926	-4.8756

Table A2: GDI and KI location and area errors for May 2018.

	GDI Location Error	GDI Area Error	KI Location Error	KI Area Error
10-May				
00Z	9.8616	-0.9584	7.4367	-3.1850
06Z	4.6919	2.1883	9.7188	-0.7218
12Z	8.6737	-1.8316	11.1456	-5.2771
18Z	7.0807	-1.3284	8.3782	-4.9392
	GDI Location Error	GDI Area Error	KI Location Error	KI Area Error
12-May				
00Z	5.5435	-1.6484	4.4884	-3.5718
06Z	6.4352	-1.7238	9.9652	-3.0621
12Z	11.3293	-0.7242	9.2939	-3.0444
18Z	9.6941	-2.0199	12.0144	-4.7481
	GDI Location Error	GDI Area Error	KI Location Error	KI Area Error
14-May				
00Z	11.1496	-3.3484	8.2827	-4.8447
06Z	16.2339	-3.5486	14.9247	-4.7351
12Z	19.0710	-2.3398	14.8227	-4.2100
18Z	11.8950	-1.1320	12.9345	-3.3617
	GDI Location Error	GDI Area Error	KI Location Error	KI Area Error
22-May				
00Z	9.7081	-3.2079	10.6165	-6.4098
06Z	7.2013	-1.1700	7.3770	-4.9798
12Z	12.9287	-0.8866	12.1429	-4.3791
18Z	9.4364	-0.6770	8.2564	-3.4691
	GDI Location Error	GDI Area Error	KI Location Error	KI Area Error
24-May				
00Z	5.3976	-0.5973	8.8197	-4.1276
06Z	16.0423	-1.5417	12.5210	-3.5519
12Z	7.5315	-0.3778	6.9549	-3.4932
18Z	17.0388	-1.2080	14.4691	-5.0465
	GDI Location Error	GDI Area Error	KI Location Error	KI Area Error
26-May				
00Z	11.5331	-3.9340	10.1056	-5.5206
06Z	12.4711	-3.8397	16.2992	-5.9317
12Z	7.3489	-1.2034	8.0638	-4.5037
18Z	14.2985	-1.0775	15.3248	-4.0723
Monthly Avg.	10.5248	-1.5890	10.5982	-4.2161

Table A3: GDI and KI location and area errors for June 2018.

	GDI Location Error	GDI Area Error	KI Location Error	KI Area Error
10-Jun				
00Z	9.1426	-1.8255	16.2344	-3.5208
06Z	10.2012	-3.7855	10.8951	-5.1356
12Z	7.2535	-0.7654	5.9873	-2.6291
18Z	5.3862	-2.3890	9.2360	-3.9504
	GDI Location Error	GDI Area Error	KI Location Error	KI Area Error
12-Jun				
00Z	6.4152	-1.1649	4.4944	-3.4233
06Z	15.8026	-3.9952	10.4371	-6.0353
12Z	7.4388	-0.8586	10.2036	-2.6174
18Z	8.2354	-1.1490	5.8273	-3.1645
	GDI Location Error	GDI Area Error	KI Location Error	KI Area Error
14-Jun				
00Z	10.2478	-0.5699	11.7935	-2.7128
06Z	22.5519	-3.2241	16.9234	-5.2196
12Z	4.9851	-1.2565	8.7479	-3.9859
18Z	8.6206	-1.8180	10.4721	-4.0343
	GDI Location Error	GDI Area Error	KI Location Error	KI Area Error
22-Jun				
00Z	7.5432	-4.0460	7.3018	-5.2908
06Z	11.6424	-4.5728	4.3513	-6.1784
12Z	6.1154	-2.5580	6.7610	-4.4500
18Z	6.2203	-1.3989	7.5183	-3.5634
	GDI Location Error	GDI Area Error	KI Location Error	KI Area Error
24-Jun				
00Z	10.8112	-2.6334	10.5198	-4.9750
06Z	13.2117	-1.2522	13.8695	-3.5927
12Z	5.3722	-1.5714	4.3860	-4.0338
18Z	6.2275	-1.2752	8.7626	-3.8750
	GDI Location Error	GDI Area Error	KI Location Error	KI Area Error
26-Jun				
00Z	6.1632	-2.2025	6.6187	-4.2215
06Z	9.3304	-1.8043	9.3664	-3.6638
12Z	11.5109	-1.7845	9.4732	-4.8602
18Z	6.6773	-1.3955	11.7591	-4.1251
Monthly Avg.	9.0461	-2.0540	9.2475	-4.1358

Table A4: GDI and KI location and area errors for July 2018.

	GDI Location Error	GDI Area Error	KI Location Error	KI Area Error
10-Jul				
00Z	5.0956	-1.8869	3.9914	-4.2642
06Z	5.6985	-2.2591	4.7575	-4.1992
12Z	13.0923	-1.2454	9.9600	-3.5834
18Z	6.0965	-0.3126	4.8603	-2.6818
	GDI Location Error	GDI Area Error	KI Location Error	KI Area Error
12-Jul				
00Z	8.3368	-1.3431	8.0187	-3.8288
06Z	11.1848	-2.4867	9.5815	-4.6345
12Z	6.6112	-1.7240	8.2995	-3.7115
18Z	6.3326	-2.9367	6.8770	-4.2041
	GDI Location Error	GDI Area Error	KI Location Error	KI Area Error
14-Jul				
00Z	7.0583	-3.2878	8.6601	-4.6676
06Z	11.8976	-3.0592	8.5326	-4.1172
12Z	12.0097	-2.6462	11.1436	-4.4149
18Z	9.1956	-1.6467	6.7281	-3.3822
	GDI Location Error	GDI Area Error	KI Location Error	KI Area Error
22-Jul				
00Z	4.9454	-1.2186	11.0651	-2.2767
06Z	6.7786	-0.8390	11.5699	-2.1985
12Z	12.7649	-1.1169	13.9086	-3.5824
18Z	7.1775	-0.4703	6.7234	-2.5633
	GDI Location Error	GDI Area Error	KI Location Error	KI Area Error
24-Jul				
00Z	8.6299	-3.1762	20.7173	-4.7685
06Z	4.2401	-2.3456	3.7173	-3.9463
12Z	11.0462	-2.7696	10.2822	-4.8388
18Z	6.2613	-1.5908	10.4808	-3.3306
	GDI Location Error	GDI Area Error	KI Location Error	KI Area Error
26-Jul				
00Z	7.5508	-4.2464	5.8833	-6.8921
06Z	10.0417	-3.2610	22.2275	-4.6542
12Z	8.6660	-1.0424	11.3261	-2.9584
18Z	8.5529	-1.9906	10.3047	-4.8532
Monthly Avg.	8.3027	-2.0376	9.5673	-3.9397

Table A5: GDI and KI location and area errors for August 2018.

	GDI Location Error	GDI Area Error	KI Location Error	KI Area Error
10-Aug				
00Z	14.8167	-2.9197	8.9988	-5.1423
06Z	15.1046	-2.6173	9.7463	-5.6560
12Z	17.4452	-1.8329	10.3504	-5.1082
18Z	14.7327	-1.5006	10.0848	-4.3521
	GDI Location Error	GDI Area Error	KI Location Error	KI Area Error
12-Aug				
00Z	10.0446	-2.3571	4.4495	-4.7200
06Z	10.4336	-2.6645	7.4471	-4.8344
12Z	7.7480	-1.7618	5.6368	-4.2957
18Z	6.8826	-1.3885	3.9533	-3.1345
	GDI Location Error	GDI Area Error	KI Location Error	KI Area Error
14-Aug				
00Z	6.0347	-3.5683	6.3974	-4.3572
06Z	10.7106	-3.7724	9.8543	-5.9749
12Z	11.0573	-1.9367	8.6963	-4.7153
18Z	11.0912	-0.1388	7.1345	-2.4909
	GDI Location Error	GDI Area Error	KI Location Error	KI Area Error
22-Aug				
00Z	7.0080	-2.5564	3.8885	-4.4163
06Z	5.6336	-1.3037	4.0015	-3.6850
12Z	7.9666	-1.2645	7.5917	-3.3794
18Z	7.1462	-1.6960	5.5129	-3.9401
	GDI Location Error	GDI Area Error	KI Location Error	KI Area Error
24-Aug				
00Z	6.4114	-2.4243	5.3432	-4.0629
06Z	5.8282	-3.2847	7.4255	-4.7422
12Z	7.4356	-2.2719	7.2255	-4.0223
18Z	7.2499	-2.3282	6.8981	-3.9922
	GDI Location Error	GDI Area Error	KI Location Error	KI Area Error
26-Aug				
00Z	5.8948	-1.9228	4.5505	-3.8599
06Z	9.8743	-3.2106	9.0433	-5.1406
12Z	18.1157	-0.9693	16.2929	-3.7045
18Z	4.2300	-0.4589	3.9379	-2.5301
Monthly Avg.	10.0985	-2.0896	7.2692	-4.2607

Table A6: GDI and KI location and area errors for September 2018.

	GDI Location Error	GDI Area Error	KI Location Error	KI Area Error
10-Sep				
00Z	13.8026	-3.0206	7.2664	-5.3321
06Z	16.7440	-0.2744	7.7366	-4.5350
12Z	10.2962	-1.0713	9.4584	-3.8523
18Z	7.4765	-1.0032	6.6476	-3.4292
	GDI Location Error	GDI Area Error	KI Location Error	KI Area Error
12-Sep				
00Z	17.0426	-2.4047	16.6382	-5.3590
06Z	8.3719	-2.1528	10.2761	-5.1173
12Z	10.7871	-0.8805	9.8462	-3.8752
18Z	9.4647	-0.7273	9.7679	-3.7138
	GDI Location Error	GDI Area Error	KI Location Error	KI Area Error
14-Sep				
00Z	12.3116	-2.1458	6.2355	-5.1127
06Z	10.6442	-2.2412	9.6938	-5.2148
12Z	*	*	*	*
18Z	*	*	*	*
	GDI Location Error	GDI Area Error	KI Location Error	KI Area Error
22-Sep				
00Z	4.8309	-2.0821	4.8174	-5.0464
06Z	5.6345	-2.6053	5.6446	-5.3807
12Z	13.4898	-0.9019	9.1771	-3.4585
18Z	3.5730	-2.0354	5.7012	-4.0876
	GDI Location Error	GDI Area Error	KI Location Error	KI Area Error
24-Sep				
00Z	8.2096	-1.6099	6.9529	-4.3563
06Z	3.0375	-3.4100	9.2589	-6.1313
12Z	11.0498	-1.8495	7.6169	-4.5384
18Z	9.5374	-0.9564	6.8450	-4.0340
	GDI Location Error	GDI Area Error	KI Location Error	KI Area Error
26-Sep				
00Z	8.1550	-1.9213	8.8472	-4.5432
06Z	6.4062	-3.0684	6.2574	-5.5074
12Z	11.3584	-1.4370	8.9150	-3.9699
18Z	9.9519	-1.8599	6.8179	-4.4669
Monthly Avg.	9.6443	-1.8027	8.2008	-4.5937
* = Model data unavailable				

Appendix B: Zulu Time Study Error Values

Table B1: All 00Z GDI and KI location and area errors.

Date/Time	GDI Location Error	GDI Area Error	KI Location Error	KI Area Error
0422/00Z	11.0585	-2.3586	10.1777	-6.2594
0424/00Z	7.7640	-2.0483	12.2039	-4.8023
0426/00Z	6.2744	-3.8422	7.0391	-6.2202
0510/00Z	9.8616	-0.9584	7.4367	-3.1850
0512/00Z	5.5435	-1.6484	4.4884	-3.5718
0514/00Z	11.1496	-3.3484	8.2827	-4.8447
0522/00Z	9.7081	-3.2079	10.6165	-6.4098
0524/00Z	5.3976	-0.5973	8.8197	-4.1276
0526/00Z	11.5331	-3.9340	10.1056	-5.5206
0610/00Z	9.1426	-1.8255	16.2344	-3.5208
0612/00Z	6.4152	-1.1649	4.4944	-3.4233
0614/00Z	10.2478	-0.5699	11.7935	-2.7128
0622/00Z	7.5432	-4.0460	7.3018	-5.2908
0624/00Z	10.8112	-2.6334	10.5198	-4.9750
0626/00Z	6.1632	-2.2025	6.6187	-4.2215
0710/00Z	5.0956	-1.8869	3.9914	-4.2642
0712/00Z	8.3368	-1.3431	8.0187	-3.8288
0714/00Z	7.0583	-3.2878	8.6601	-4.6676
0722/00Z	4.9454	-1.2186	11.0651	-2.2767
0724/00Z	8.6299	-3.1762	20.7173	-4.7685
0726/00Z	7.5508	-4.2464	5.8833	-6.8921
0810/00Z	14.8167	-2.9197	8.9988	-5.1423
0812/00Z	10.0446	-2.3571	4.4495	-4.7200
0814/00Z	6.0347	-3.5683	6.3974	-4.3572
0822/00Z	7.0080	-2.5564	3.8885	-4.4163
0824/00Z	6.4114	-2.4243	5.3432	-4.0629
0826/00Z	5.8948	-1.9228	4.5505	-3.8599
0910/00Z	13.8026	-3.0206	7.2664	-5.3321
0912/00Z	17.0426	-2.4047	16.6382	-5.3590
0914/00Z	12.3116	-2.1458	6.2355	-5.1127
0922/00Z	4.8309	-2.0821	4.8174	-5.0464
0924/00Z	8.2096	-1.6099	6.9529	-4.3563
0926/00Z	8.1550	-1.9213	8.8472	-4.5432
Avg.	8.6301	-2.3781	8.4501	-4.6088

Table B2: All 06Z GDI and KI location and area errors.

Date/Time	GDI Location Error	GDI Area Error	KI Location Error	KI Area Error
0422/06Z	10.1457	-0.1676	8.6034	-3.6068
0424/06Z	13.4614	-0.6717	16.7154	-4.2185
0426/06Z	3.9952	-3.2322	6.2069	-5.8842
0510/06Z	4.6919	2.1883	9.7188	-0.7218
0512/06Z	6.4352	-1.7238	9.9652	-3.0621
0514/06Z	16.2339	-3.5486	14.9247	-4.7351
0522/06Z	7.2013	-1.1700	7.3770	-4.9798
0524/06Z	16.0423	-1.5417	12.5210	-3.5519
0526/06Z	12.4711	-3.8397	16.2992	-5.9317
0610/06Z	10.2012	-3.7855	10.8951	-5.1356
0612/06Z	15.8026	-3.9952	10.4371	-6.0353
0614/06Z	22.5519	-3.2241	16.9234	-5.2196
0622/06Z	11.6424	-4.5728	4.3513	-6.1784
0624/06Z	13.2117	-1.2522	13.8695	-3.5927
0626/06Z	9.3304	-1.8043	9.3664	-3.6638
0710/06Z	5.6985	-2.2591	4.7575	-4.1992
0712/06Z	11.1848	-2.4867	9.5815	-4.6345
0714/06Z	11.8976	-3.0592	8.5326	-4.1172
0722/06Z	6.7786	-0.8390	11.5699	-2.1985
0724/06Z	4.2401	-2.3456	3.7173	-3.9463
0726/06Z	10.0417	-3.2610	22.2275	-4.6542
0810/06Z	15.1046	-2.6173	9.7463	-5.6560
0812/06Z	10.4336	-2.6645	7.4471	-4.8344
0814/06Z	10.7106	-3.7724	9.8543	-5.9749
0822/06Z	5.6336	-1.3037	4.0015	-3.6850
0824/06Z	5.8282	-3.2847	7.4255	-4.7422
0826/06Z	9.8743	-3.2106	9.0433	-5.1406
0910/06Z	16.7440	-0.2744	7.7366	-4.5350
0912/06Z	8.3719	-2.1528	10.2761	-5.1173
0914/06Z	10.6442	-2.2412	9.6938	-5.2148
0922/06Z	5.6345	-2.6053	5.6446	-5.3807
0924/06Z	3.0375	-3.4100	9.2589	-6.1313
0926/06Z	6.4062	-3.0684	6.2574	-5.5074
Avg.	10.0510	-2.3393	9.8468	-4.6117

Table B3: All 12Z GDI and KI location and area errors.

Date/Time	GDI Location Error	GDI Area Error	KI Location Error	KI Area Error
0422/12Z	16.1837	-2.7599	22.0443	-6.3218
0424/12Z	12.6368	-1.0855	12.4409	-5.0577
0426/12Z	5.6584	-1.1595	6.1660	-4.3140
0510/12Z	8.6737	-1.8316	11.1456	-5.2771
0512/12Z	11.3293	-0.7242	9.2939	-3.0444
0514/12Z	19.0710	-2.3398	14.8227	-4.2100
0522/12Z	12.9287	-0.8866	12.1429	-4.3791
0524/12Z	7.5315	-0.3778	6.9549	-3.4932
0526/12Z	7.3489	-1.2034	8.0638	-4.5037
0610/12Z	7.2535	-0.7654	5.9873	-2.6291
0612/12Z	7.4388	-0.8586	10.2036	-2.6174
0614/12Z	4.9851	-1.2565	8.7479	-3.9859
0622/12Z	6.1154	-2.5580	6.7610	-4.4500
0624/12Z	5.3722	-1.5714	4.3860	-4.0338
0626/12Z	11.5109	-1.7845	9.4732	-4.8602
0710/12Z	13.0923	-1.2454	9.9600	-3.5834
0712/12Z	6.6112	-1.7240	8.2995	-3.7115
0714/12Z	12.0097	-2.6462	11.1436	-4.4149
0722/12Z	12.7649	-1.1169	13.9086	-3.5824
0724/12Z	11.0462	-2.7696	10.2822	-4.8388
0726/12Z	8.6660	-1.0424	11.3261	-2.9584
0810/12Z	17.4452	-1.8329	10.3504	-5.1082
0812/12Z	7.7480	-1.7618	5.6368	-4.2957
0814/12Z	11.0573	-1.9367	8.6963	-4.7153
0822/12Z	7.9666	-1.2645	7.5917	-3.3794
0824/12Z	7.4356	-2.2719	7.2255	-4.0223
0826/12Z	18.1157	-0.9693	16.2929	-3.7045
0910/12Z	10.2962	-1.0713	9.4584	-3.8523
0912/12Z	10.7871	-0.8805	9.8462	-3.8752
0922/12Z	13.4898	-0.9019	9.1771	-3.4585
0924/12Z	11.0498	-1.8495	7.6169	-4.5384
0926/12Z	11.3584	-1.4370	8.9150	-3.9699
Avg.	10.4681	-1.4964	9.8238	-4.0996

Table B4: All 18Z GDI and KI location and area errors.

Date/Time	GDI Location Error	GDI Area Error	KI Location Error	KI Area Error
0422/18Z	8.9697	-1.7264	5.2807	-4.1465
0424/18Z	9.7394	-1.3633	6.2243	-4.2531
0426/18Z	6.1260	-0.6050	6.8091	-3.4221
0510/18Z	7.0807	-1.3284	8.3782	-4.9392
0512/18Z	9.6941	-2.0199	12.0144	-4.7481
0514/18Z	11.8950	-1.1320	12.9345	-3.3617
0522/18Z	9.4364	-0.6770	8.2564	-3.4691
0524/18Z	17.0388	-1.2080	14.4691	-5.0465
0526/18Z	14.2985	-1.0775	15.3248	-4.0723
0610/18Z	5.3862	-2.3890	9.2360	-3.9504
0612/18Z	8.2354	-1.1490	5.8273	-3.1645
0614/18Z	8.6206	-1.8180	10.4721	-4.0343
0622/18Z	6.2203	-1.3989	7.5183	-3.5634
0624/18Z	6.2275	-1.2752	8.7626	-3.8750
0626/18Z	6.6773	-1.3955	11.7591	-4.1251
0710/18Z	6.0965	-0.3126	4.8603	-2.6818
0712/18Z	6.3326	-2.9367	6.8770	-4.2041
0714/18Z	9.1956	-1.6467	6.7281	-3.3822
0722/18Z	7.1775	-0.4703	6.7234	-2.5633
0724/18Z	6.2613	-1.5908	10.4808	-3.3306
0726/18Z	8.5529	-1.9906	10.3047	-4.8532
0810/18Z	14.7327	-1.5006	10.0848	-4.3521
0812/18Z	6.8826	-1.3885	3.9533	-3.1345
0814/18Z	11.0912	-0.1388	7.1345	-2.4909
0822/18Z	7.1462	-1.6960	5.5129	-3.9401
0824/18Z	7.2499	-2.3282	6.8981	-3.9922
0826/18Z	4.2300	-0.4589	3.9379	-2.5301
0910/18Z	7.4765	-1.0032	6.6476	-3.4292
0912/18Z	9.4647	-0.7273	9.7679	-3.7138
0922/18Z	3.5730	-2.0354	5.7012	-4.0876
0924/18Z	9.5374	-0.9564	6.8450	-4.0340
0926/18Z	9.9519	-1.8599	6.8179	-4.4669
Avg.	8.4562	-1.3626	8.2044	-3.7924

Appendix C: Convective Regime Study Error Values

Table C1: GDI and KI airmass thunderstorm location and area errors.

Day/Time	Convection Type	GDI Location Error	GDI Area Error	KI Location Error	KI Area Error
0514/12Z	AT	19.0710	-2.3398	14.8227	-4.2100
0522/12Z	AT	12.9287	-0.8866	12.1429	-4.3791
0522/18Z	AT	9.4364	-0.6770	8.2564	-3.4691
0524/12Z	AT	7.5315	-0.3778	6.9549	-3.4932
0526/06Z	AT	12.4711	-3.8397	16.2992	-5.9317
0526/12Z	AT	7.3489	-1.2034	8.0638	-4.5037
0526/18Z	AT	14.2985	-1.0775	15.3248	-4.0723
0610/06Z	AT	10.2012	-3.7855	10.8951	-5.1356
0610/12Z	AT	7.2535	-0.7654	5.9873	-2.6291
0610/18Z	AT	5.3862	-2.3890	9.2360	-3.9504
0612/00Z	AT	6.4152	-1.1649	4.4944	-3.4233
0612/06Z	AT	15.8026	-3.9952	10.4371	-6.0353
0612/12Z	AT	7.4388	-0.8586	10.2036	-2.6174
0614/12Z	AT	4.9851	-1.2565	8.7479	-3.9859
0622/12Z	AT	6.1154	-2.5580	6.7610	-4.4500
0626/00Z	AT	6.1632	-2.2025	6.6187	-4.2215
0626/06Z	AT	9.3304	-1.8043	9.3664	-3.6638
0626/12Z	AT	11.5109	-1.7845	9.4732	-4.8602
0710/00Z	AT	5.0956	-1.8869	3.9914	-4.2642
0710/06Z	AT	5.6985	-2.2591	4.7575	-4.1992
0710/12Z	AT	13.0923	-1.2454	9.9600	-3.5834
0710/18Z	AT	6.0965	-0.3126	4.8603	-2.6818
0712/12Z	AT	6.6112	-1.7240	8.2995	-3.7115
0712/18Z	AT	6.3326	-2.9367	6.8770	-4.2041
0714/00Z	AT	7.0583	-3.2878	8.6601	-4.6676
0714/06Z	AT	11.8976	-3.0592	8.5326	-4.1172
0714/12Z	AT	12.0097	-2.6462	11.1436	-4.4149
0722/00Z	AT	4.9454	-1.2186	11.0651	-2.2767
0722/06Z	AT	6.7786	-0.8390	11.5699	-2.1985
0722/12Z	AT	12.7649	-1.1169	13.9086	-3.5824
0724/12Z	AT	11.0462	-2.7696	10.2822	-4.8388
0726/06Z	AT	10.0417	-3.2610	22.2275	-4.6542
0726/12Z	AT	8.6660	-1.0424	11.3261	-2.9584
0814/18Z	AT	11.0912	-0.1388	7.1345	-2.4909
0822/00Z	AT	7.0080	-2.5564	3.8885	-4.4163
0822/06Z	AT	5.6336	-1.3037	4.0015	-3.6850
0822/12Z	AT	7.9666	-1.2645	7.5917	-3.3794
0822/18Z	AT	7.1462	-1.6960	5.5129	-3.9401
0824/06Z	AT	5.8282	-3.2847	7.4255	-4.7422
0824/12Z	AT	7.4356	-2.2719	7.2255	-4.0223
0826/12Z	AT	12.6280	-1.2393	12.4925	-3.0084
0912/06Z	AT	8.3719	-2.1528	10.2761	-5.1173
0912/12Z	AT	10.7871	-0.8805	9.8462	-3.8752
0914/00Z	AT	12.3116	-2.1458	6.2355	-5.1127
0914/06Z	AT	10.6442	-2.2412	9.6938	-5.2148
0922/12Z	AT	13.4898	-0.9019	9.1771	-3.4585
0926/12Z	AT	11.3584	-1.4370	8.9150	-3.9699
	Avg.	9.2239	-1.8316	9.1694	-3.9961

Table C2: GDI and KI airmass thunderstorm location and area errors.

	Convection Type	GDI Location Error	GDI Area Error	KI Location Error	KI Area Error
Day/Time					
0424/00Z	MCS	7.7640	-2.0483	12.2039	-4.8023
0424/18Z	MCS	9.7394	-1.3633	6.2243	-4.2531
0426/00Z	MCS	6.2744	-3.8422	7.0391	-6.2202
0426/06Z	MCS	3.9952	-3.2322	6.2069	-5.8842
0510/00Z	MCS	9.8616	-0.9584	7.4367	-3.1850
0514/06Z	MCS	16.2339	-3.5486	14.9247	-4.7351
0614/00Z	MCS	22.5519	-3.2241	16.9234	-5.2196
0624/06Z	MCS	13.2117	-1.2522	13.8695	-3.5927
0814/06Z	MCS	10.7106	-3.7724	9.8543	-5.9749
0910/00Z	MCS	13.8026	-3.0206	7.2664	-5.3321
0922/00Z	MCS	4.8309	-2.0821	4.8174	-5.0464
0922/18Z	MCS	3.5730	-2.0354	5.7012	-4.0876
	Avg.	10.2124	-2.5316	9.3723	-4.8611

Table C3: GDI and KI airmass and MCS thunderstorm location and area errors.

Day/Time	Convection Type	GDI Location Error	GDI Area Error	KI Location Error	KI Area Error
0422/00Z	AT/MCS	11.0585	-2.3586	10.1777	-6.2594
0422/06Z	AT/MCS	10.1457	-0.1676	8.6034	-3.6068
0422/12Z	AT/MCS	16.1837	-2.7599	22.0443	-6.3218
0426/12Z	AT/MCS	5.6584	-1.1595	6.1660	-4.3140
0426/18Z	AT/MCS	6.1260	-0.6050	6.8091	-3.4221
0510/12Z	AT/MCS	8.6737	-1.8316	11.1456	-5.2771
0512/12Z	AT/MCS	11.3293	-0.7242	9.2939	-3.0444
0512/18Z	AT/MCS	9.6941	-2.0199	12.0144	-4.7481
0514/18Z	AT/MCS	11.8950	-1.1320	12.9345	-3.3617
0522/00Z	AT/MCS	9.7081	-3.2079	10.6165	-6.4098
0522/06Z	AT/MCS	7.2013	-1.1700	7.3770	-4.9798
0524/00Z	AT/MCS	5.3976	-0.5973	8.8197	-4.1276
0524/06Z	AT/MCS	15.8995	-1.6118	14.8152	-4.5598
0524/18Z	AT/MCS	15.1767	-1.5499	17.3999	-4.3511
0526/00Z	AT/MCS	11.5331	-3.9340	10.1056	-5.5206
0612/18Z	AT/MCS	8.2354	-1.1490	5.8273	-3.1645
0614/18Z	AT/MCS	8.6206	-1.8180	10.4721	-4.0343
0622/18Z	AT/MCS	6.2203	-1.3989	7.5183	-3.5634
0624/12Z	AT/MCS	5.3722	-1.5714	4.3860	-4.0338
0624/18Z	AT/MCS	6.2275	-1.2752	8.7626	-3.8750
0626/18Z	AT/MCS	6.6773	-1.3955	11.7591	-4.1251
0712/06Z	AT/MCS	11.1848	-2.4867	9.5815	-4.6345
0714/18Z	AT/MCS	9.1956	-1.6467	6.7281	-3.3822
0722/18Z	AT/MCS	7.1775	-0.4703	6.7234	-2.5633
0724/18Z	AT/MCS	6.2613	-1.5908	10.4808	-3.3306
0810/00Z	AT/MCS	14.8167	-2.9197	8.9988	-5.1423
0810/06Z	AT/MCS	15.1046	-2.6173	9.7463	-5.6560
0810/12Z	AT/MCS	17.4452	-1.8329	10.3504	-5.1082
0812/06Z	AT/MCS	10.4336	-2.6645	7.4471	-4.8344
0812/12Z	AT/MCS	7.7480	-1.7618	5.6368	-4.2957
0814/12Z	AT/MCS	11.0573	-1.9367	8.6963	-4.7153
0824/18Z	AT/MCS	7.2499	-2.3282	6.8981	-3.9922
0826/06Z	AT/MCS	9.8743	-3.2106	9.0433	-5.1406
0826/18Z	AT/MCS	4.2300	-0.4589	3.9379	-2.5301
0910/06Z	AT/MCS	16.7440	-0.2744	7.7366	-4.5350
0910/12Z	AT/MCS	10.2962	-1.0713	9.4584	-3.8523
0912/00Z	AT/MCS	17.0426	-2.4047	16.6382	-5.3590
0922/06Z	AT/MCS	4.8309	-2.0821	4.8174	-5.0464
0924/12Z	AT/MCS	11.0498	-1.8495	7.6169	-4.5384
0926/00Z	AT/MCS	8.1550	-1.9213	8.8472	-4.5432
0926/06Z	AT/MCS	6.4062	-3.0684	6.2574	-5.5074
0926/18Z	AT/MCS	9.9519	-1.8599	6.8179	-4.4669
	Avg.	9.8402	-1.7594	9.2740	-4.4351

Table C4: GDI and KI MCS and airmass thunderstorm location and area errors.

Day/Time	Convection Type	GDI Location Error	GDI Area Error	KI Location Error	KI Area Error
0422/18Z	MCS/AT	8.9697	-1.7264	5.2807	-4.1465
0424/06Z	MCS/AT	13.4614	-0.6717	16.7154	-4.2185
0424/12Z	MCS/AT	12.6368	-1.0855	12.4409	-5.0577
0510/06Z	MCS/AT	4.6919	2.1883	9.7188	-0.7218
0510/18Z	MCS/AT	7.0807	-1.3284	8.3782	-4.9392
0512/00Z	MCS/AT	5.5435	-1.6484	4.4884	-3.5718
0512/06Z	MCS/AT	6.4352	-1.7238	9.9652	-3.0621
0514/00Z	MCS/AT	11.1496	-3.3484	8.2827	-4.8447
0610/00Z	MCS/AT	9.1426	-1.8255	16.2344	-3.5208
0614/06Z	MCS/AT	22.5519	-3.2241	16.9234	-5.2196
0622/00Z	MCS/AT	7.5432	-4.0460	7.3018	-5.2908
0622/06Z	MCS/AT	11.6424	-4.5728	4.3513	-6.1784
0624/00Z	MCS/AT	10.8112	-2.6334	10.5198	-4.9750
0712/00Z	MCS/AT	8.3368	-1.3431	8.0187	-3.8288
0724/00Z	MCS/AT	8.6299	-3.1762	20.7173	-4.7685
0724/06Z	MCS/AT	4.2401	-2.3456	3.7173	-3.9463
0726/00Z	MCS/AT	7.5508	-4.2464	5.8833	-6.8921
0726/18Z	MCS/AT	8.5529	-1.9906	10.3047	-4.8532
0810/18Z	MCS/AT	14.7327	-1.5006	10.0848	-4.3521
0812/00Z	MCS/AT	10.0446	-2.3571	4.4495	-4.7200
0812/18Z	MCS/AT	6.8826	-1.3885	3.9533	-3.1345
0814/00Z	MCS/AT	6.0347	-3.5683	6.3974	-4.3572
0824/00Z	MCS/AT	6.4114	-2.4243	5.3432	-4.0629
0826/00Z	MCS/AT	5.8948	-1.9228	4.5505	-3.8599
0910/18Z	MCS/AT	7.4765	-1.0032	6.6476	-3.4292
0912/18Z	MCS/AT	9.4647	-0.7273	9.7679	-3.7138
0924/00Z	MCS/AT	8.2096	-1.6099	6.9529	-4.3563
0924/06Z	MCS/AT	3.0375	-3.4100	9.2589	-6.1313
0924/18Z	MCS/AT	9.5374	-0.9564	6.8450	-4.0340
	Avg.	8.8516	-2.0557	8.7411	-4.3513

Appendix D: Regional Study Error Values

Table D1: West Africa regional study GDI and KI location and area errors for the period from late April through mid-June 2018.

Day/Time	Region	GDI Location Error	GDI Area Error	KI Location Error	KI Area Error
0422/00Z	West	4.3140	-1.2741	10.2082	-4.3719
0422/06Z	West	8.2462	-2.8871	9.4730	-6.1271
0422/12Z	West	15.4743	-1.1276	13.2554	-4.7933
0422/18Z	West	13.4726	-1.1608	5.1106	-4.7302
0424/00Z	West	4.9584	-2.6743	8.2013	-5.9567
0424/06Z	West	7.3200	-1.9230	6.0346	-4.7606
0424/12Z	West	4.9992	-1.0614	10.0786	-3.5102
0424/18Z	West	4.4723	-0.7988	8.3861	-3.1638
0426/00Z	West	6.9881	-2.2549	10.1615	-5.0076
0426/06Z	West	7.9558	-1.3908	8.4118	-4.4178
0426/12Z	West	6.1294	-1.8051	7.2665	-3.9696
0426/18Z	West	5.8975	-1.2576	5.4111	-3.3910
0510/00Z	West	4.0019	-2.2578	6.0808	-3.9016
0510/06Z	West	4.2064	-1.5777	4.2587	-3.1498
0510/12Z	West	5.6360	-2.6033	7.0801	-4.4068
0510/18Z	West	5.1794	-1.2855	4.1893	-2.7708
0512/00Z	West	4.7065	-2.0403	3.9961	-3.3336
0512/06Z	West	5.4216	-1.1598	5.8350	-2.3298
0512/12Z	West	10.4740	-2.1255	10.8710	-3.3880
0512/18Z	West	4.1140	-1.1773	5.2494	-2.5193
0514/00Z	West	7.2825	-2.1486	6.9418	-3.4466
0514/06Z	West	7.7368	-1.8401	5.5175	-3.1957
0514/12Z	West	11.0369	-1.9721	10.5345	-3.4658
0514/18Z	West	4.5620	-1.0712	4.6001	-2.6919
0522/00Z	West	7.7330	-2.3316	5.1159	-5.0133
0522/06Z	West	11.9521	-1.3254	6.0988	-4.1265
0522/12Z	West	9.7150	-1.0138	5.7134	-3.8644
0522/18Z	West	6.5814	-0.1870	3.6659	-2.2946
0524/00Z	West	5.8442	-1.4857	4.2414	-3.7528
0524/06Z	West	3.6896	-0.6101	4.4326	-2.5302
0524/12Z	West	6.4170	-0.5470	6.1596	-2.2592
0524/18Z	West	6.2345	-1.4007	4.4571	-3.1116
0526/00Z	West	14.2708	-2.7479	11.0007	-5.0426
0526/06Z	West	4.6366	-2.1975	3.9815	-3.8802
0526/12Z	West	7.8490	-2.4172	7.1699	-4.4553
0526/18Z	West	9.8597	-1.3534	6.4733	-3.5074
0610/00Z	West	3.8943	-1.2482	5.6454	-3.0108
0610/06Z	West	9.9633	-2.8084	6.7749	-3.8533
0610/12Z	West	6.0208	-2.6947	6.3456	-3.4866
0610/18Z	West	8.7315	-1.4157	11.6724	-2.4066
0612/00Z	West	3.6645	-0.5128	1.6069	-2.6664
0612/06Z	West	5.9163	-2.2329	2.9599	-4.2552
0612/12Z	West	7.8055	-1.3513	7.5875	-3.2425
0612/18Z	West	4.9120	-0.6795	7.0080	-2.4041
0614/00Z	West	4.6051	-1.0802	4.0271	-3.0541
0614/06Z	West	4.6051	-1.0802	4.0271	-3.0541

Table D2: West Africa regional study GDI and KI location and area errors for the period from mid-June through mid-August 2018.

0614/12Z	West		7.7769	-1.8347	6.1837	-3.7443
0614/18Z	West		7.4863	-1.8318	5.5356	-3.3943
0622/00Z	West		4.3059	-1.9198	7.5079	-3.3189
0622/06Z	West		5.4442	-1.9931	4.7021	-3.3023
0622/12Z	West		8.1118	-1.3409	7.2888	-3.0722
0622/18Z	West		7.3854	-0.4015	8.3476	-2.4542
0624/00Z	West		12.4516	-2.1225	9.9963	-4.1586
0624/06Z	West		6.8660	-1.5404	4.6109	-3.4190
0624/12Z	West		6.2617	-2.0591	4.7043	-4.3570
0624/18Z	West		7.6271	-1.1042	3.5506	-3.1271
0626/00Z	West		4.9384	-2.6154	5.7360	-3.6888
0626/06Z	West		7.9472	-1.9906	6.6193	-3.4075
0626/12Z	West		11.8305	-1.4042	10.5848	-3.8802
0626/18Z	West		6.1969	-1.4232	5.9825	-3.1483
0710/00Z	West		8.7504	-0.8764	7.5847	-4.0435
0710/06Z	West		7.2323	-2.0294	5.1172	-3.0253
0710/12Z	West		5.6051	-1.6790	5.0797	-3.3534
0710/18Z	West		5.2582	-1.1388	4.9177	-3.1361
0712/00Z	West		3.5477	-0.9941	6.8720	-3.1061
0712/06Z	West		4.6864	-1.5743	5.9201	-3.3532
0712/12Z	West		3.8828	-1.3736	3.8254	-3.1002
0712/18Z	West		4.6009	-0.8701	3.4726	-2.0521
0714/00Z	West		5.6103	-2.2528	2.4792	-3.5312
0714/06Z	West		8.3083	-2.4097	6.2217	-3.3725
0714/12Z	West		15.2492	-3.7607	17.6839	-5.0047
0714/18Z	West		11.1529	-1.2707	6.6521	-2.9154
0722/00Z	West		6.7162	-0.8278	2.2105	-2.0410
0722/06Z	West		5.7957	-2.4824	2.9593	-3.6822
0722/12Z	West		9.0620	-0.5207	8.0737	-2.2097
0722/18Z	West		8.9525	-0.2492	7.8230	-1.8330
0724/00Z	West		7.1890	-2.1006	7.2130	-3.8500
0724/06Z	West		5.2031	-2.6585	4.8444	-4.1634
0724/12Z	West		8.8965	-3.0188	11.1216	-4.0682
0724/18Z	West		9.3848	-1.5974	7.5127	-3.1972
0726/00Z	West		5.1789	-2.1690	6.2545	-2.8385
0726/06Z	West		8.6114	-2.1366	5.8670	-3.0755
0726/12Z	West		9.0679	-0.4925	6.8522	-2.1087
0726/18Z	West		8.1901	-1.2051	3.8752	-2.1104
0810/00Z	West		15.7427	-2.0322	7.6524	-4.7869
0810/06Z	West		9.2133	-2.0186	6.9979	-5.6258
0810/12Z	West		17.2382	-1.1452	11.7161	-3.8263
0810/18Z	West		3.9951	-0.5140	4.5678	-3.4863
0812/00Z	West		6.0189	-1.9180	6.8792	-4.7912
0812/06Z	West		7.7847	-1.7325	6.2133	-4.2415
0812/12Z	West		8.0515	-1.4577	6.2017	-3.8772
0812/18Z	West		8.2783	-0.8558	1.8593	-2.5912
0814/00Z	West		7.7155	-2.8822	8.4932	-4.4331
0814/06Z	West		5.0114	-3.2988	4.2617	-4.8455

Table D3: West Africa regional study GDI and KI location and area errors for the period from mid-August through late September 2018.

0814/12Z	West		11.4545	-2.0030		9.8747	-3.9306
0814/18Z	West		7.1048	-0.4761		6.0120	-2.3057
0822/00Z	West		5.4427	-1.0218		4.6741	-3.2993
0822/06Z	West		5.2078	-1.7413		7.2417	-3.4246
0822/12Z	West		7.4175	-0.4655		10.4789	-3.3301
0822/18Z	West		6.7076	-1.7422		4.7721	-4.1478
0824/00Z	West		4.6162	-2.7334		3.4344	-4.6088
0824/06Z	West		7.7174	-1.7268		2.6316	-3.5762
0824/12Z	West		4.5611	-1.8742		6.5096	-2.4661
0824/18Z	West		4.8592	-1.7253		5.4905	-3.3554
0826/00Z	West		7.5114	-1.8676		4.1262	-3.5178
0826/06Z	West		8.6874	-2.2353		9.1407	-3.8169
0826/12Z	West		15.4416	-2.3272		14.4169	-3.6472
0826/18Z	West		5.8252	-1.1483		7.0137	-2.7055
0910/00Z	West		12.4766	-2.7007		9.4180	-4.3897
0910/06Z	West		12.9047	-3.2111		9.0624	-4.8417
0910/12Z	West		6.6712	-2.1956		9.1694	-3.8317
0910/18Z	West		5.1020	-1.6079		6.7191	-2.8067
0912/00Z	West		7.4731	-2.1180		10.7003	-2.7816
0912/06Z	West		8.6055	-3.1080		11.6872	-4.5071
0912/12Z	West		9.9297	-0.4604		15.2912	-2.2823
0912/18Z	West		10.5987	-0.6974		12.5008	-2.6982
0914/00Z	West		9.2435	-1.5930		7.0076	-3.9156
0914/06Z	West		7.3952	-2.8072		7.5026	-4.6252
0922/00Z	West		5.3424	-1.7763		6.0580	-3.5514
0922/06Z	West		5.2365	-2.6041		3.6655	-4.0849
0922/12Z	West		9.2089	-1.7148		11.1359	-3.2864
0922/18Z	West		7.3027	-1.1835		7.0380	-3.0468
0924/00Z	West		5.3987	-1.4199		4.2720	-3.3676
0924/06Z	West		6.9711	-2.4124		7.0549	-3.7663
0924/12Z	West		8.9314	-1.9296		7.1807	-3.5412
0924/18Z	West		4.4580	-1.4929		5.0532	-3.0725
0926/00Z	West		2.9022	-1.4054		5.7398	-3.7617
0926/06Z	West		5.1793	-2.8124		6.0438	-4.8626
0926/12Z	West		8.5325	-1.9123		13.6727	-3.5377
0926/18Z	West		6.0660	-0.2285		6.1465	-2.8009
	Avg.		7.3676	-1.6861		6.8298	-3.5516

Table D4: East Africa regional study GDI and KI location and area errors for the period from late August through mid-June 2018.

Day/Time	Region	GDI Location Error	GDI Area Error	KI Location Error	KI Area Error
0422/00Z	East	5.9646	-2.3326	6.5983	-4.7377
0422/06Z	East	7.9044	-1.2224	8.3548	-3.6114
0422/12Z	East	9.7922	-0.7718	6.7824	-2.7587
0422/18Z	East	9.9288	-0.7771	4.6326	-2.5255
0424/00Z	East	7.3305	-2.1264	7.9756	-3.4320
0424/06Z	East	6.7765	-1.1826	5.7545	-3.2920
0424/12Z	East	7.0135	-1.2445	12.4373	-3.0072
0424/18Z	East	11.8520	-1.6105	8.0026	-3.4672
0426/00Z	East	2.1404	-1.6508	8.3235	-3.2202
0426/06Z	East	3.4321	-1.4519	7.2867	-3.1170
0426/12Z	East	8.0141	-0.3524	6.8289	-2.3648
0426/18Z	East	6.1801	-1.0009	7.0828	-3.0983
0510/00Z	East	12.7108	1.2098	5.3486	-1.8610
0510/06Z	East	14.3231	1.2236	10.3816	-3.2671
0510/12Z	East	11.1286	-0.5550	9.4310	-4.3955
0510/18Z	East	11.3984	-0.4937	8.4398	-3.5250
0512/00Z	East	9.0626	-1.5368	4.8737	-3.8566
0512/06Z	East	7.7922	-2.2573	6.0156	-4.5852
0512/12Z	East	7.1906	-0.2858	5.0549	-2.6823
0512/18Z	East	8.6116	-0.0970	7.4312	-3.1436
0514/00Z	East	12.9826	-3.7578	9.7488	-5.2753
0514/06Z	East	13.2180	-2.7917	7.8137	-4.9605
0514/12Z	East	8.0573	-1.0470	6.8928	-4.0417
0514/18Z	East	11.7921	-0.8372	8.3554	-3.7607
0522/00Z	East	3.6767	-2.1407	5.9947	-4.2936
0522/06Z	East	2.9898	-2.4566	5.2662	-5.0841
0522/12Z	East	8.4515	-1.0936	10.5141	-3.5742
0522/18Z	East	7.9389	-1.0569	12.5221	-3.1442
0524/00Z	East	7.5468	-1.6282	8.7626	-4.0924
0524/06Z	East	7.4507	-1.4826	6.0855	-3.9877
0524/12Z	East	7.5674	-0.4822	10.7406	-4.2171
0524/18Z	East	3.9022	-1.1283	11.8532	-4.2252
0526/00Z	East	6.2058	-1.1184	9.4807	-4.5657
0526/06Z	East	9.0517	-2.4391	12.4577	-4.9112
0526/12Z	East	7.9252	0.1371	12.4249	-2.6353
0526/18Z	East	7.7242	-0.1777	12.8737	-3.5027
0610/00Z	East	5.4718	-1.6487	8.4232	-3.2127
0610/06Z	East	10.1244	-2.4518	10.9752	-3.7335
0610/12Z	East	7.2891	-0.3612	9.3639	-2.4017
0610/18Z	East	10.5958	-1.9477	10.0655	-4.3520
0612/00Z	East	7.6971	-2.2578	9.3940	-4.9789

Table D5: East Africa regional study GDI and KI location and area errors for the period from mid-June through early August 2018.

0612/12Z	East		6.7084	-0.8722	7.3036	-2.6079
0612/18Z	East		3.9116	-1.2415	5.7337	-2.4409
0614/00Z	East		8.2109	-2.2561	6.1466	-4.1957
0614/06Z	East		6.0351	-3.6649	3.4846	-5.7648
0614/12Z	East		2.6098	-0.1604	10.5561	-2.0718
0614/18Z	East		5.1912	-1.1632	7.9097	-4.2771
0622/00Z	East		9.8734	-2.5522	10.1403	-4.8658
0622/06Z	East		12.3121	-3.3489	11.0519	-4.6261
0622/12Z	East		5.2731	-0.5427	6.5037	-2.4565
0622/18Z	East		4.9186	-1.4368	6.5643	-3.1408
0624/00Z	East		4.0501	-2.3043	4.5887	-3.8666
0624/06Z	East		8.7284	-3.2698	6.0293	-5.0011
0624/12Z	East		3.4433	-0.8291	7.1510	-3.0767
0624/18Z	East		2.7182	-1.4908	11.0363	-3.6521
0626/00Z	East		4.1866	-1.7661	8.9696	-3.3305
0626/06Z	East		2.1875	-2.2587	12.1421	-4.9596
0626/12Z	East		4.3855	-0.4851	7.0874	-2.2318
0626/18Z	East		6.9642	-1.4237	10.7097	-3.8475
0710/00Z	East		4.6045	-1.9998	10.5764	-3.0086
0710/06Z	East		7.4112	-2.2895	9.6867	-3.1711
0710/12Z	East		1.8290	-1.4427	12.9936	-2.6124
0710/18Z	East		5.1843	-1.9930	5.2187	-4.0850
0712/00Z	East		5.6029	-2.8004	10.0821	-5.0018
0712/06Z	East		8.2451	-4.2241	9.0054	-4.0835
0712/12Z	East		7.0210	-0.7091	9.9947	-2.1209
0712/18Z	East		12.3685	-2.2131	6.9715	-4.4530
0714/00Z	East		10.8443	-2.3828	8.8144	-4.0578
0714/06Z	East		18.2818	-2.8798	12.7339	-4.7485
0714/12Z	East		8.0481	-1.6389	6.1453	-3.0409
0714/18Z	East		6.3518	-2.3670	6.4859	-3.4722
0722/00Z	East		15.6563	-3.3189	4.5819	-3.8332
0722/06Z	East		12.4184	-1.9810	7.1101	-2.9866
0722/12Z	East		4.7724	-0.9488	9.9289	-2.0953
0722/18Z	East		2.2273	-1.8563	12.8893	-3.1039
0724/00Z	East		10.0425	-1.6408	10.0759	-2.8116
0724/06Z	East		8.6594	-1.6450	7.0266	-2.5452
0724/12Z	East		7.1587	-1.1464	4.0475	-2.6639
0724/18Z	East		7.3459	-1.7582	5.2227	-3.0072
0726/00Z	East		9.2046	-2.0830	5.9156	-3.5107
0726/06Z	East		7.4170	-2.6039	10.6686	-4.1035
0726/12Z	East		3.4092	-1.0035	9.7953	-2.7154
0726/18Z	East		4.4589	-2.3954	12.2790	-4.0176
0810/00Z	East		12.7488	-2.6017	8.3954	-4.2311

Table D6: East Africa regional study GDI and KI location and area errors for the period from early August through late September 2018.

0810/06Z	East		16.5612	-2.3796		13.0473	-4.3655
0810/12Z	East		5.6753	-0.9847		6.1506	-2.3262
0810/18Z	East		6.3440	-1.3677		6.9408	-3.3169
0812/00Z	East		3.6721	-1.7451		5.3215	-2.8730
0812/06Z	East		4.4203	-2.5833		4.7841	-4.0059
0812/12Z	East		3.5480	-1.5867		5.5581	-2.9163
0812/18Z	East		3.6637	-2.2770		4.2713	-3.4102
0814/00Z	East		9.8514	-1.4156		5.5135	-3.6158
0814/06Z	East		10.8114	-2.9804		8.2063	-4.7251
0814/12Z	East		4.9166	-0.5312		6.5890	-2.4655
0814/18Z	East		3.6428	-1.1247		4.6895	-2.8422
0822/00Z	East		5.9170	-2.5158		6.8311	-3.6829
0822/06Z	East		7.6910	-2.3296		6.6420	-3.8075
0822/12Z	East		7.0663	-1.3976		4.6874	-2.8885
0822/18Z	East		4.4716	-2.0207		6.3808	-3.4656
0824/00Z	East		7.6753	-2.4062		7.2213	-3.3004
0824/06Z	East		8.4824	-2.5873		6.4590	-3.5502
0824/12Z	East		3.0025	-1.1005		4.1740	-2.2812
0824/18Z	East		2.7213	-2.2603		4.4802	-3.3126
0826/00Z	East		4.4922	-3.1504		5.7568	-4.7583
0826/06Z	East		8.6484	-2.4005		10.3772	-3.4564
0826/12Z	East		5.4340	-1.1803		5.3463	-2.1044
0826/18Z	East		2.8930	-2.4187		4.4766	-3.6535
0910/00Z	East		14.7845	-1.7634		7.8991	-4.0862
0910/06Z	East		12.6584	-1.0682		8.3668	-3.3821
0910/12Z	East		2.8799	0.1754		7.9192	-2.6187
0910/18Z	East		5.6641	-1.0382		9.8499	-4.1544
0912/00Z	East		14.1609	-2.1705		8.8580	-5.4920
0912/06Z	East		6.6403	-1.8450		10.8192	-4.2249
0912/12Z	East		2.2480	-0.4230		10.5480	-4.0451
0912/18Z	East		8.0872	-1.2236		10.6303	-4.6295
0914/00Z	East		14.9335	-3.4268		10.5766	-6.8094
0914/06Z	East		8.2767	-2.1191		4.3782	-5.7009
0922/00Z	East		3.1892	-1.6119		9.7758	-3.8631
0922/06Z	East		6.8134	-2.5263		11.2732	-6.4624
0922/12Z	East		8.1260	-0.3688		9.4197	-3.0907
0922/18Z	East		8.2360	-0.5481		7.2721	-2.5386
0924/00Z	East		8.9943	-1.5593		10.8741	-4.4188
0924/06Z	East		11.0099	-3.2822		12.3439	-6.6117
0924/12Z	East		8.3822	-0.9446		10.8883	-3.3992
0924/18Z	East		8.5834	-0.8400		12.0018	-4.2465
0926/00Z	East		10.1158	-1.5269		9.6938	-4.1032
0926/06Z	East		8.2767	-2.1191		8.5996	-6.9200
0926/12Z	East		8.3672	-0.0320		10.2837	-2.5591
0926/18Z	East		9.2055	-1.0104		10.9058	-3.6159
	Avg.		7.5229	-1.6255		8.2471	-3.6968

Appendix E: Model Comparison Study Error Values

Table E1: 2016 GDI and KI location and area errors for the May and August cases.

2016 Days	GDI Location Error	GDI Area Error	KI Location Error	KI Area Error
15-May				
00Z	8.8344	-3.4514	6.1004	-4.1110
06Z	10.0927	-2.2737	8.7138	-3.4176
12Z	9.8751	-2.4033	10.7886	-3.4467
18Z	11.5262	-2.1844	9.1068	-3.2176
	GDI Location Error	GDI Area Error	KI Location Error	KI Area Error
16-May				
00Z	8.0889	-2.3141	6.9928	-3.5209
06Z	15.7398	-5.1008	9.7793	-5.6697
12Z	10.6567	-2.3880	8.9303	-3.6497
18Z	6.0948	-2.3274	6.4844	-3.3495
	GDI Location Error	GDI Area Error	KI Location Error	KI Area Error
17-May				
00Z	9.9091	-2.8715	5.1626	-3.7142
06Z	7.9955	-2.9138	5.0578	-3.8435
12Z	6.4434	-2.3065	9.1875	-3.6122
18Z	3.8826	-1.2684	6.7202	-2.8431
Monthly Avg.	9.0949	-2.6503	7.7520	-3.6996
	GDI Location Error	GDI Area Error	KI Location Error	KI Area Error
15-Aug				
00Z	10.8902	-2.7219	10.6562	-3.9668
06Z	7.4679	-3.4978	5.6891	-4.4858
12Z	7.2218	-2.2769	7.2827	-3.9651
18Z	6.3276	-1.6093	5.9715	-2.9803
	GDI Location Error	GDI Area Error	KI Location Error	KI Area Error
16-Aug				
00Z	8.0526	-2.3992	7.5083	-3.4600
06Z	6.5550	-4.1313	7.0744	-4.9069
12Z	6.7877	-2.1230	8.4034	-3.2765
18Z	8.6408	-3.0583	9.5456	-4.1275
2016 Days	GDI Location Error	GDI Area Error	KI Location Error	KI Area Error
17-Aug				
00Z	8.5077	-2.3503	7.7113	-3.5466
06Z	6.3799	-4.0407	4.9944	-5.1143
12Z	4.8714	-2.2058	5.8226	-3.3258
18Z	7.6571	-2.0663	7.8702	-3.2748
Monthly Avg.	7.4466	-2.7067	7.3775	-3.8692

Table E2: 2016 GDI and KI location and area errors for the September examples.

	GDI Location Error	GDI Area Error	KI Location Error	KI Area Error
15-Sep				
00Z	4.5335	-2.2687	6.5670	-3.3462
06Z	6.7971	-2.8898	10.2042	-4.3708
12Z	9.2997	-2.2408	11.7058	-3.8623
18Z	2.8859	-1.7103	3.5711	-3.5584
	GDI Location Error	GDI Area Error	KI Location Error	KI Area Error
16-Sep				
00Z	11.4196	-2.4986	5.5830	-3.8545
06Z	13.3775	-0.6109	4.0234	-3.3807
12Z	9.6692	-1.7208	12.0903	-3.4232
18Z	5.4143	-1.1867	3.5213	-2.4205
	GDI Location Error	GDI Area Error	KI Location Error	KI Area Error
17-Sep				
00Z	6.5800	-2.4627	9.1213	-4.1335
06Z	5.9563	-2.2935	3.7619	-4.0047
12Z	12.8252	-2.0585	10.1355	-2.9903
18Z	7.3046	-1.9262	8.1644	-2.4631
Monthly Avg.	8.0052	-1.9890	7.3708	-3.4840
	GDI Location Error	GDI Area Error	KI Location Error	KI Area Error
26-Sep				
00Z	4.3328	-2.7584	3.3867	-3.2332
06Z	14.0531	-3.7801	14.9128	-4.9797
12Z	14.0742	-1.0592	5.3221	-0.8668
18Z	5.4557	-1.7792	6.3457	-2.5700
2016 Days	GDI Location Error	GDI Area Error	KI Location Error	KI Area Error
27-Sep				
00Z	5.9021	-1.7079	7.6313	-3.8174
06Z	7.6262	-2.0818	8.3298	-3.6706
12Z	16.4456	-1.5361	9.2064	-3.6042
18Z	11.7714	-0.6653	3.7624	-1.8244
Monthly Avg.	9.9576	-1.9210	7.3621	-3.0708

Table E3: 2018 GDI and KI location and area errors for the May examples.

2018 Days	GDI Location Error	GDI Area Error	KI Location Error	KI Area Error
10-May				
00Z	9.8616	-0.9584	7.4367	-3.1850
06Z	4.6919	2.1883	9.7188	-0.7218
12Z	8.6737	-1.8316	11.1456	-5.2771
18Z	7.0807	-1.3284	8.3782	-4.9392
	GDI Location Error	GDI Area Error	KI Location Error	KI Area Error
12-May				
00Z	5.5435	-1.6484	4.4884	-3.5718
06Z	6.4352	-1.7238	9.9652	-3.0621
12Z	11.3293	-0.7242	9.2939	-3.0444
18Z	9.6941	-2.0199	12.0144	-4.7481
	GDI Location Error	GDI Area Error	KI Location Error	KI Area Error
14-May				
00Z	11.1496	-3.3484	8.2827	-4.8447
06Z	16.2339	-3.5486	14.9247	-4.7351
12Z	19.0710	-2.3398	14.8227	-4.2100
18Z	11.8950	-1.1320	12.9345	-3.3617
	GDI Location Error	GDI Area Error	KI Location Error	KI Area Error
22-May				
00Z	9.7081	-3.2079	10.6165	-6.4098
06Z	7.2013	-1.1700	7.3770	-4.9798
12Z	12.9287	-0.8866	12.1429	-4.3791
18Z	9.4364	-0.6770	8.2564	-3.4691
	GDI Location Error	GDI Area Error	KI Location Error	KI Area Error
24-May				
00Z	5.3976	-0.5973	8.8197	-4.1276
06Z	16.0423	-1.5417	12.5210	-3.5519
12Z	7.5315	-0.3778	6.9549	-3.4932
18Z	17.0388	-1.2080	14.4691	-5.0465
2018 Days	GDI Location Error	GDI Area Error	KI Location Error	KI Area Error
26-May				
00Z	11.5331	-3.9340	10.1056	-5.5206
06Z	12.4711	-3.8397	16.2992	-5.9317
12Z	7.3489	-1.2034	8.0638	-4.5037
18Z	14.2985	-1.0775	15.3248	-4.0723
Monthly Avg.	10.5248	-1.5890	10.5982	-4.2161

Table E4: 2018 GDI and KI location and area errors for the August examples.

	GDI Location Error	GDI Area Error	KI Location Error	KI Area Error
10-Aug				
00Z	14.8167	-2.9197	8.9988	-5.1423
06Z	15.1046	-2.6173	9.7463	-5.6560
12Z	17.4452	-1.8329	10.3504	-5.1082
18Z	14.7327	-1.5006	10.0848	-4.3521
	GDI Location Error	GDI Area Error	KI Location Error	KI Area Error
12-Aug				
00Z	10.0446	-2.3571	4.4495	-4.7200
06Z	10.4336	-2.6645	7.4471	-4.8344
12Z	7.7480	-1.7618	5.6368	-4.2957
18Z	6.8826	-1.3885	3.9533	-3.1345
	GDI Location Error	GDI Area Error	KI Location Error	KI Area Error
14-Aug				
00Z	6.0347	-3.5683	6.3974	-4.3572
06Z	10.7106	-3.7724	9.8543	-5.9749
12Z	11.0573	-1.9367	8.6963	-4.7153
18Z	11.0912	-0.1388	7.1345	-2.4909
	GDI Location Error	GDI Area Error	KI Location Error	KI Area Error
22-Aug				
00Z	7.0080	-2.5564	3.8885	-4.4163
06Z	5.6336	-1.3037	4.0015	-3.6850
12Z	7.9666	-1.2645	7.5917	-3.3794
18Z	7.1462	-1.6960	5.5129	-3.9401
2018 Days	GDI Location Error	GDI Area Error	KI Location Error	KI Area Error
24-Aug				
00Z	6.4114	-2.4243	5.3432	-4.0629
06Z	5.8282	-3.2847	7.4255	-4.7422
12Z	7.4356	-2.2719	7.2255	-4.0223
18Z	7.2499	-2.3282	6.8981	-3.9922
	GDI Location Error	GDI Area Error	KI Location Error	KI Area Error
26-Aug				
00Z	5.8948	-1.9228	4.5505	-3.8599
06Z	9.8743	-3.2106	9.0433	-5.1406
12Z	18.1157	-0.9693	16.2929	-3.7045
18Z	4.2300	-0.4589	3.9379	-2.5301
Monthly Avg.	10.0985	-2.0896	7.2692	-4.2607

Table E5: 2018 GDI and KI location and area errors for the September examples.

	GDI Location Error	GDI Area Error	KI Location Error	KI Area Error
10-Sep				
00Z	13.8026	-3.0206	7.2664	-5.3321
06Z	16.7440	-0.2744	7.7366	-4.5350
12Z	10.2962	-1.0713	9.4584	-3.8523
18Z	7.4765	-1.0032	6.6476	-3.4292
	GDI Location Error	GDI Area Error	KI Location Error	KI Area Error
12-Sep				
00Z	17.0426	-2.4047	16.6382	-5.3590
06Z	8.3719	-2.1528	10.2761	-5.1173
12Z	10.7871	-0.8805	9.8462	-3.8752
18Z	9.4647	-0.7273	9.7679	-3.7138
	GDI Location Error	GDI Area Error	KI Location Error	KI Area Error
14-Sep				
00Z	12.3116	-2.1458	6.2355	-5.1127
06Z	10.6442	-2.2412	9.6938	-5.2148
12Z	*	*	*	*
18Z	*	*	*	*
2018 Days	GDI Location Error	GDI Area Error	KI Location Error	KI Area Error
22-Sep				
00Z	4.8309	-2.0821	4.8174	-5.0464
06Z	5.6345	-2.6053	5.6446	-5.3807
12Z	13.4898	-0.9019	9.1771	-3.4585
18Z	3.5730	-2.0354	5.7012	-4.0876
	GDI Location Error	GDI Area Error	KI Location Error	KI Area Error
24-Sep				
00Z	8.2096	-1.6099	6.9529	-4.3563
06Z	3.0375	-3.4100	9.2589	-6.1313
12Z	11.0498	-1.8495	7.6169	-4.5384
18Z	9.5374	-0.9564	6.8450	-4.0340
	GDI Location Error	GDI Area Error	KI Location Error	KI Area Error
26-Sep				
00Z	8.1550	-1.9213	8.8472	-4.5432
06Z	6.4062	-3.0684	6.2574	-5.5074
12Z	11.3584	-1.4370	8.9150	-3.9699
18Z	9.9519	-1.8599	6.8179	-4.4669
Monthly Avg.	9.6443	-1.8027	8.2008	-4.5937
* = Model data unavailable				

Appendix F: GDI-A Study Error Values

Tables F1 and F2: GDIA location and area errors for the August 2018 examples using the GDI modification of RH700 (left) and EPTP900 (right).

RH700	GDI Location Error	GDI Area Error
10-Aug		
00Z	12.6537	-2.9946
06Z	12.1374	-3.2644
12Z	16.1369	-1.4610
18Z	14.2453	-0.5269
	GDI Location Error	GDI Area Error
12-Aug		
00Z	3.7432	-1.7175
06Z	5.6817	-2.3166
12Z	10.7919	-1.5172
18Z	6.8487	-0.9726
	GDI Location Error	GDI Area Error
14-Aug		
00Z	12.9998	-2.7205
06Z	8.5742	-3.4660
12Z	13.9206	-1.6074
18Z	5.5631	0.0132
	GDI Location Error	GDI Area Error
22-Aug		
00Z	5.8575	-2.1567
06Z	6.1656	-0.8319
12Z	10.1044	-0.6450
18Z	6.3919	-1.1738
	GDI Location Error	GDI Area Error
24-Aug		
00Z	4.7652	-2.0186
06Z	5.5573	-2.5897
12Z	7.4681	-2.2601
18Z	8.1691	-1.9840
	GDI Location Error	GDI Area Error
26-Aug		
00Z	6.5552	-1.9440
06Z	8.0468	-3.2854
12Z	9.8962	-1.4284
18Z	5.3886	-0.1993
Monthly Avg.	8.6526	-1.7945

EPTP900	GDI Location Error	GDI Area Error
10-Aug		
00Z	11.6538	-3.8432
06Z	14.7017	-4.4286
12Z	7.3827	-3.6482
18Z	10.8791	-3.0025
	GDI Location Error	GDI Area Error
12-Aug		
00Z	4.2657	-3.4909
06Z	9.1067	-3.9203
12Z	4.8048	-2.8457
18Z	6.0968	-2.0194
	GDI Location Error	GDI Area Error
14-Aug		
00Z	2.9539	-3.9500
06Z	10.5784	-4.7122
12Z	6.4745	-3.0127
18Z	6.5727	-1.2589
	GDI Location Error	GDI Area Error
22-Aug		
00Z	4.5342	-3.0497
06Z	5.9693	-2.3815
12Z	5.1375	-1.1971
18Z	7.2794	-2.4100
	GDI Location Error	GDI Area Error
24-Aug		
00Z	6.8170	-2.9047
06Z	5.3238	-3.4533
12Z	5.0846	-2.8570
18Z	7.1426	-2.8668
	GDI Location Error	GDI Area Error
26-Aug		
00Z	4.2377	-2.8904
06Z	9.9586	-4.2329
12Z	12.3361	-1.9112
18Z	3.8232	-1.4633
Monthly Avg.	7.2131	-2.9896

Table F3: GDIA location and area errors for the August 2018 examples using the Elevated Layer A GDI modification.

Layer A	GDI Location Error	GDI Area Error
10-Aug		
00Z	12.4304	-3.5466
06Z	14.6079	-3.9439
12Z	7.3651	-3.0616
18Z	10.7250	-2.2860
	GDI Location Error	GDI Area Error
12-Aug		
00Z	4.3303	-2.9172
06Z	9.1398	-3.4427
12Z	5.5930	-2.2161
18Z	6.4407	-1.6618
	GDI Location Error	GDI Area Error
14-Aug		
00Z	3.3028	-3.5028
06Z	10.5255	-4.1311
12Z	5.5926	-2.3988
18Z	5.9920	-0.6969
	GDI Location Error	GDI Area Error
22-Aug		
00Z	5.5834	-2.7749
06Z	7.0907	-1.4525
12Z	5.2611	-1.3201
18Z	7.2447	-2.0054
	GDI Location Error	GDI Area Error
24-Aug		
00Z	4.3597	-2.3640
06Z	7.1840	-2.6514
12Z	4.3401	-2.1076
18Z	8.1680	-2.5070
	GDI Location Error	GDI Area Error
26-Aug		
00Z	5.1202	-2.4413
06Z	11.2453	-3.7111
12Z	12.4246	-1.5007
18Z	4.6435	-1.0712
Monthly Avg.	7.4463	-2.4880

Bibliography

AFWA, 2012: Weather techniques and procedures lightning detection systems. 1-26pp.

Colorado State, 2003: Numerical Weather Prediction. Accessed: 29 November

    2018, http://rams.atmos.colostate.edu/at540/fall03/fall03Pt7.pdf

Davies-Jones, Robert, 2009: On formulas for equivalent potential temperature. Notes and

    Correspondence, 137, 3137-3148, DOI: 10.1175/2009MWR2774.1

Efron, Bradley, and R. Tibshirani, 1993: An Introduction to the Bootstrap. Chapman and

    Hall/CRC, 437 pp.

Gálvez, Jose, and Michel Davison, 2016. "The ForeO-Davison Index for Tropical Convection."

    NOAA, www.wpc.ncep.noaa.gov/international/gdi/GDI_Manuscript_V20161021.pdf.

Galvin, J. F. P., 2016: An Introduction to the Meteorology and Climate of the Tropics.

    Wiley-Blackwell, 328 pp.

16th Weather Squadron, 2016: GALWEM Version 8.5 Specifications. 16th Weather

    Squadron/WXE Offutt AFB, NE.

George, J. J., 1960: Weather forecasting for aeronautics. New York and London Press,

    673 pp.

Holton, J. R. and G. J. Hakim, 2013: An Introduction to Dynamic Meteorology. Academic Press,

    532 pp.

Jirak, I. L., W. R. Cotton, and R. L. McAnelly, 2003: Satellite and radar survey of mesoscale

    convective systems development. Mon. Wea. Rev., 131, 2428-2449,

    https://journals.ametsoc.org/doi/10.1175/1520-

    0493%282003%29131%3C2428%3ASARSOM%3E2.0.CO%3B2

King, Angela, 2006: Africa Physical Map. Geology.com, Map Resources,

https://geology.com/world/africa-physical-map.shtml

Kirshnamurti, T. N., L. Stefanova and V. Misra, 2013: Tropical Meteorology: An Introduction.

Springer, 423 pp.

Krauss, 2019: Kelvin and Rossby Waves. Geo.cornell.edu, Cornell University,

http://www.geo.cornell.edu/ocean/p_ocean/ppt_notes/21_KelvinRossbyWaves.pdf

Marzban, C. and S. Sandgathe, 2005: Cluster analysis for verification of precipitation fields.

Wea. Forecasting, 21, 824-830,

http://journals.ametsoc.org/doi/abs/10.1175/WAF948.1

Mekonnen, Ademe, et al., 2008: Convectively Coupled Kelvin Waves over Tropical Africa

during the Boreal Summer: Structure and Variability. Journal of Climate, vol. 20, no. 24,

pp. 1500–1501., doi:10.1175/2008jcli2008.1.

Mounier, Flore, et al., 2007: Analysis of the Dominant Mode of Convectively Coupled Kelvin

Waves in the West African Monsoon. Journal of Climate, vol. 20, no. 8, pp. 1487–1503,

doi:10.1175/jcli4059.1.

NexSat, 2011: About NexSat. Accessed 29 November

2018, www.nrlmry.navy.mil/nexdat/headliner/About%20the%20NexSat%20web%20pag

e.pdf

North Carolina Climate Office, 2019: General Circulation of the Atmosphere.

https://climate.ncsu.edu/edu/AtmosCirculation

NWS, 2018: Thunderstorm and Lightning Awareness. Accessed 29 November

2018, https://www.weather.gov/cae/thunder.html

Orloff, J. and J. Bloom, 2014: Bootstrap confidence intervals. MIT
OpenCourseWare, https://ocw.mit.edu/courses/mathematics/18-
05.../MIT18_05S14_Reading24.pdf

Pawlowicz, R., 2018: M_Map: A mapping package for MATLAB, version 1.4j, [Computer
software], www.eoas.ubc.ca/~rich/map.html.

Peng, Grace, 2014: Analysis, Reanalysis, Forecast - What's the Difference? UCAR, NCAR,
https://rda.ucar.edu/datasets/ds083.2/docs/Analysis.pdf.

Sensirion, 2001: Dew-point calculation. Application note. 1-3pp.,
http://irtfweb.ifa.hawaii.edu/~tcs3/tcs3/Misc/Dewpoint_Calculation_Humidity_Sensor_E
.pdf

Singh, S. and N. A. Gill, 2013: Analysis and study of k-means clustering algorithm.
International Journal of Engineering Research & Technology, 2, 2546-2551,
https://www.ijert.org/download/4586/analysis-and-study-of-k-means-clusteringalgorithm

Toracinta, E. R., D. J. Cecil, E. J. Zipser, and S. W. Nesbitt, 2001: Radar, passive microwave and
lightning characteristics of precipitating systems in the tropics.
Mon. Wea. Rev., 130, 802-824, http://journals.ametsoc.org/doi/abs/10.1175/1520-
0493(2002)130%3C0802%3ARPMALC%3E2.0.CO%3B2.

UCAR, 2014: NCEP FNLvGFS. Accessed 22 April
2018, http://rda.ucar.edu/datasets/ds083.2/docs/FNLvGFS.pdf

UCAR, 2018: NCEP FNL Operational Model Global Tropospheric Analysis, description.
Accessed 22 April 2018, https://rda.ucar.edu/datasets/ds083.2/

Weather.us, 2018: Satellite Cloud Tops Alert Image. OpenStreetMap Contributors GIScienceResearch Group at Heidelberg University, Accessed 29 Nov 2018, https://weather.us/satellite/africa/top-alert-15min/20180822-0700z.html.

Wilks, D. S., 2011: Statistical Methods in the Atmospheric Sciences. Academic Press, 676 pp.

Wuebbles, D.J., 2017: Observational datasets used in climate studies. In: Climate Science Special Report: Fourth National Climate Assessment, Volume I [Wuebbles, D.J., D.W. Fahey, K.A. Hibbard, D.J. Dokken, B.C. Stewart, and T.K. Maycock (eds.)]. U.S. Global Change Research Program, Washington, DC, USA, pp. 430-435, doi: 10.7930/J0BK19HT.

Zijlma, Anouk, 2018: A Brief Guide to Africa's Dry and Rainy Seasons. TripSavvy, https://www.tripsavvy.com/africas-dry-and-rainy-seasons-1453967

REPORT DOCUMENTATION PAGE

The public reporting burden for this collection of information is estimated to average 1 hour per response, including the time for reviewing instructions, searching existing data sources, gathering and maintaining the data needed, and completing and reviewing the collection of information. Send comments regarding this burden estimate or any other aspect of this collection of information, including suggestions for reducing the burden, to Department of Defense, Washington Headquarters Services, Directorate for Information Operations and Reports (0704-0188), 1215 Jefferson Davis Highway, Suite 1204, Arlington, VA 22202-4302. Respondents should be aware that notwithstanding any other provision of law, no person shall be subject to any penalty for failing to comply with a collection of information if it does not display a currently valid OMB control number.
PLEASE DO NOT RETURN YOUR FORM TO THE ABOVE ADDRESS.

1. REPORT DATE *(DD-MM-YYYY)*	2. REPORT TYPE	3. DATES COVERED *(From - To)*

4. TITLE AND SUBTITLE

5a. CONTRACT NUMBER

5b. GRANT NUMBER

5c. PROGRAM ELEMENT NUMBER

6. AUTHOR(S)

5d. PROJECT NUMBER

5e. TASK NUMBER

5f. WORK UNIT NUMBER

7. PERFORMING ORGANIZATION NAME(S) AND ADDRESS(ES)

8. PERFORMING ORGANIZATION REPORT NUMBER

9. SPONSORING/MONITORING AGENCY NAME(S) AND ADDRESS(ES)

10. SPONSOR/MONITOR'S ACRONYM(S)

11. SPONSOR/MONITOR'S REPORT NUMBER(S)

12. DISTRIBUTION/AVAILABILITY STATEMENT

13. SUPPLEMENTARY NOTES

14. ABSTRACT

15. SUBJECT TERMS

16. SECURITY CLASSIFICATION OF:			17. LIMITATION OF ABSTRACT	18. NUMBER OF PAGES	19a. NAME OF RESPONSIBLE PERSON
a. REPORT	b. ABSTRACT	c. THIS PAGE			
					19b. TELEPHONE NUMBER *(Include area code)*